RADIOLYSIS EFFECTS IN MUONIUM CHEMISTRY

by

Siu-keung Leung

B.Sc., Simon Fraser University, 1982

M.Sc., Simon Fraser University, 1985

THESIS SUBMITTED IN PARTIAL FULFILLMENT OF

THE REQUIREMENTS FOR THE DEGREE OF

DOCTOR OF PHILOSOPHY

in the Department

of

Chemistry

SIMON FRASER UNIVERSITY

March, 1991

APPROVAL

Name: Siu-keung Leung

Degree: Doctor of Philosophy

Title of thesis: Radiolysis Effects in Muonium Chemistry

Examining Committee:

Chairperson:	F.W.B. Einstein, Professor
Senior Supervisor:	P.W. Percival, Professor
	C.H.W. Jones, Professor
	E.J. Wells, Associate Professor
Internal Examiner:	I.D. Gay, Professor
External Examiner:	G.R. Freeman, Professor University of Alberta

Date Approved: 16th April 1991

PARTIAL COPYRIGHT LICENSE

I hereby grant to Simon Fraser University the right to lend my thesis, project or extended essay (the title of which is shown below) to users of the Simon Fraser University Library, and to make partial or single copies only for such users or in response to a request from the library of any other university, or other educational institution, on its own behalf or for one of its users. I further agree that permission for multiple copying of this work for scholarly purposes may be granted by me or the Dean of Graduate Studies. It is understood that copying or publication of this work for financial gain shall not be allowed without my written permission.

Title of Thesis/Project/Extended Essay

Radiolysis Effects in Muonium Chemistry

Author:

(signature)

Siu-Keung Leung

(name)

Apr. 17/91

(date)

ABSTRACT

When positive muons (μ^+) stop in water roughly 60% are incorporated in diamagnetic compounds, and the remainder form muonium (Mu = μ^+e^-). The two fractions can be distinguished by their muon spin rotation (μSR) signals, but the signal amplitudes indicate that part of the initial muon spin polarization is missing. Previous work showed that the depolarization process is a result of encounters between muonium atoms and hydrated electrons e^-_{aq} formed at the end of the muon track. The reaction of muonium with hydrated electrons in aqueous solutions is investigated in this work. A reexamination of the field dependence of the muon polarization in the diamagnetic signal by conventional μSR methods has revealed a small increase of the diamagnetic fraction at low fields, which is consistent with formation of MuH from Mu on the same time-scale as the muonium depolarization process. This has been explored in a variety of experiments at assorted temperatures, pressures, and concentrations of paramagnetic ions. The spin-dependent interactions between muonium and e^-_{aq} are expected to be nonhomogeneous and their encounter time was estimated to be approximately 1 ns.

The nonhomogeneous kinetics between muonium and e^-_{aq} was studied by using pyrogallol (1,2,3−hydroxybenzene) as a trap to capture the magnitude of the muonium fraction at various times after the entrance of μ^+ into the sample. For low concentration of pyrogallol (< 3 mM) the radical signal amplitudes, measured by muon level-crossing resonance (μLCR) spectroscopy, are consistent with radical formation by addition of thermal Mu to one or other of the unsubstituted positions of the benzene ring. At higher concentrations this reaction competes with the muonium depolarization process, and results in increased signal amplitudes.

ACKNOWLEDGEMENTS

My deepest gratitude goes to Professor Paul W. Percival, my senior supervisor, for the guidance he imparted and the directions he showed me over the course of this study. I am also forever indebted to him for his endless patience and understanding during some of the difficult periods that I encountered over the course of my study. Without his leadership and knowledge, this work would not have been possible.

I would also like to thank Dr. Jean-Claude Brodovitch for the numerous discussions we had on kinetics problems and his helpful suggestions on various issues. The numerous pieces of apparatus that he invented for the SFUMU group will be very well remembered.

I am grateful to Mr. Dake Yu, my fellow graduate student, for many constructive rap sessions on the theory of μLCR and intramolecular motions. His friendship made the program more enjoyable.

Miss Julie Bartlett is acknowledged for her help during the earlier part of the research. Credits also go to the staff of beam lines M15 and M20 at TRIUMF. Their technical know-how and workmanship expedited many experimental setup sessions.

Thanks are not enough to show my appreciation to my family members for their continual support. I thank my mother for all the lunch packages; Bosco, my brother, and his family for providing me with inexpensive room and board; Manny, my sister, and her family for their supportive stands.

In memory of my father

"it seems possible that polarized positive and negative muons will become a powerful tool for exploring magnetic fields in nuclei, atoms, and interatomic regions."

R. L. Garwin, L. M Lederman, and M. Weinrich
upon the invention of μSR,
Phys. Rev. Lett., 55, 105 (1957)

TABLE OF CONTENTS

APPROVAL ii

ABSTRACT iii

ACKNOWLEDGEMENTS iv

LIST OF TABLES ix

LIST OF FIGURES x

CHAPTER I. INTRODUCTION 1
- I.1. General background 1
- I.2. Muonium in aqueous solutions 5
- I.3. Aims of this research 6

CHAPTER II. MUON SPECTROSCOPIC TECHNIQUES I - μSR 8
- II.1. Production and decay of μ^+ 8
- II.2. The transverse field μSR technique 12
- II.3. The μSR spectrum of muonium 15
- II.4. The μSR spectrum for Mu-substituted radicals 18

CHAPTER III. MUONIUM FORMATION IN AQUEOUS SOLUTIONS 22
- III.1. Introduction 22
- III.2. Radiolysis of water 22
- III.3. The hot atom model of Mu formation 24
- III.4. The spur model of Mu formation and the missing fraction in aqueous solutions 27

CHAPTER IV. EXPERIMENTAL METHODS AND INSTRUMENTATION 31
- IV.1. TRIUMF 31
- IV.2. Different types of muon beam produced at TRIUMF 33
- IV.3. Transverse field μSR experiments 37
- IV.4. The data acquisition system for transverse field μSR experiments 38
- IV.5. Data analysis 42
- IV.6. Particle detectors 42
- IV.7. Sample cell, sample handling and temperature control 43

CHAPTER V. THE REACTION OF MUONIUM WITH HYDRATED ELECTRONS 48
- V.1. Introduction 48
- V.2. Experimental 51
- V.3. Data analysis 53
- V.4. Calibration procedure 53
- V.5. Experimental results 58

V.5.1. The diamagnetic muon fraction in water 58
V.5.2. The muonium fraction in water 58
V.5.3. Aqueous solutions 62
V.6. Discussion 69
V.6.1. The origin of the field dependence of P_D in pure water 69
V.6.2. The identity of the diamagnetic muon species in water 70
V.6.3. The time-scale of "slow" MuH formation 73
V.6.4. Reinterpretation of earlier residual polarization studies 74
V.6.5. Competitive pathways of muon distribution 75
V.7. Conclusion 79

CHAPTER VI. MUON SPECTROSCOPIC TECHNIQUES II - μLCR 80
VI.1. The muon level-crossing resonance (μLCR) technique 80
VI.2. The experimental setup for longitudinal field μLCR experiments 86

CHAPTER VII. MU-SUBSTITUTED RADICALS IN AQUEOUS SOLUTIONS 90
VII.1. Introduction 90
VII.2. Experimental 92
VII.2.1. Muonium kinetics 92
VII.2.2. Radical products 94
VII.2.3. LCR signal amplitudes in pyrogallol 95
VII.3. Discussion 101
VII.3.1. Homogeneous Muonium kinetics 101
VII.3.2. Competition kinetics 103
VII.4. Conclusion 106

CHAPTER VIII. SUMMARIES OF COLLABORATIVE PROJECTS ... 107
VIII.1. Introduction 107
VIII.2. Pressure-dependent muonium kinetics in aqueous solutions . 107
VIII.3. Intramolecular motion in the Mu-substituted tert-butyl radical 110
VIII.4. Structure and intramolecular motion of Mu-substituted cyclohexadienyl radicals 113
VIII.5. Hyperfine constants for the ethyl radical in the gas phase .. 118
VIII.6. Muonium formation in C_2H_6 and N_2 120
VIII.7. Capto-dative effects in Mu-substituted cyclohexadienyl radicals 128

CHAPTER IX. SUMMARY 138

REFERENCES 140

LIST OF TABLES

TABLE		PAGE
Table I.1.	Physical properties of the positive muon	2
Table I.2.	Properties of muonium	4
Table V.1.	Residual polarization analysis of the field dependence of P_D for pure water	60
Table V.2.	Magnitudes and ratios of the muonium fractions in water	65
Table V.3.	Residual polarization analysis of P_D for some aqueous solutions	67
Table VII.1.	μLCR signal amplitudes and polarization fractions	98
Table VII.2.	Parameters used to fit the low concentration data on muonium addition to pyrogallol	102
Table VIII.1.	Muon (A_μ) and proton (A_p) hyperfine coupling constants for the CH_2CH_2Mu radical in the gas phase	119
Table VIII.2.	Muon, deuteron, and ^{13}C hyperfine couplings for CD_2CD_2Mu and $^{13}CH_2{}^{13}CH_2Mu$ in the gas phase at room temperature	121
Table VIII.3.	Experimental values of ν^+, ν^- and ν^μ for some hydroxy-substituted cyclohexadienyl radicals. The calculated values of A_μ are also included.	132
Table VIII.4.	A_μ, A_p, and B_0 for some hydroxy-substituted cyclohexadienyls	133
Table VIII.5.	Calculated values of A_μ, Δ_x, and Δ_{xy} for some hydroxy-substituted cyclohexadienyl radicals	136
Table VIII.6.	Values of Δ_{xy} for the interaction of two substituents in the cyclohexadienyl radical (in units of 100 Δ_{xy})	137

LIST OF FIGURES

FIGURE		PAGE
Figure II.1.	Energy spectrum of positrons, e^+, and energy dependence of the asymmetry parameter D.	11
Figure II.2.	Typical setup for a transverse field μSR experiment.	14
Figure II.3.	μSR spectrum (top) and diamagnetic signal (bottom) from water in a transverse field of 200G. The precession signal is obtained from the histogram by subtraction of the background and dividing out the exponential decay.	16
Figure II.4.	*Breit-Rabi* diagram of the energy levels of muonium.	17
Figure II.5.	Fourier transform spectrum of a Mu-substituted ethyl radical at 15 kG and 300K. A_μ of this radical is 331.1 MHz at 300K.	21
Figure III.1.	Idealized distribution of ions and excited molecules in the track of an energetic particle.	25
Figure IV.1.	The layout of the experimental areas of the TRIUMF cyclotron.	32
Figure IV.2.	The layout of the beamline magnets of the M20 muon channel.	34
Figure IV.3.	The layout of the beamline magnets of the M15 muon channel.	35
Figure IV.4.	The SFUMU apparatus setup for transverse field μSR experiments.	39
Figure IV.5.	The principal electronic components of the time-differential μSR setup.	41
Figure IV.6.	Schematic drawing of a particle detector.	44
Figure IV.7.	A schematic representation of the sample cell.	45
Figure IV.8.	The flow system used for sample handling.	47
Figure V.1.	Residual muon polarization in the diamagnetic products of a single-step muonium reaction as a function of magnetic field.	50
Figure V.2.	Schematic representation of the high-pressure cell and scintillator arrangement.	52

Figure V.3. Muon asymmetry as a function of applied magnetic field in Al (o) and CCl_4 (□). 55

Figure V.4. Muon asymmetry for a sample of 50% manganous nitrate solution in (a) the high-pressure cell, compared with (b) a conventional thin-walled cell, under an applied field of 200G. . 57

Figure V.5. Muon polarization as a function of magnetic field for pure water at 323 (o), 298 (Δ), and 276 K (□). 59

Figure V.6. Muon polarization in water as a function of pressure in applied fields of 50 (o), 200 (Δ), and 800 G (□). 61

Figure V.7. Muonium fractions in water as a function of pressure: P_M (o), h_M (Δ), and $h_M - h_{MD}$ (□). 63

Figure V.8. Muonium polarization in water as a function of temperature: P_M (o), h_M (Δ), and $h_M - h_{MD}$ (□). 64

Figure V.9. Muon polarization as a function of magnetic field for $MnCl_2$ solutions, 0.004 (o), 0.04 (Δ), and 0.4 M (□); and 0.8 M NaCl (■). 66

Figure V.10. Muon precession signals in: (a) $MnCl_2 \cdot 10H_2O$, (b) $MnCl_2 \cdot 10H_2O$ + a large excess of nitric acid, and (c) pure water. 68

Figure V.11. Muonium decay rates determined from the residual polarization study of thiosulphate solutions [7]. 76

Figure VI.1. Top: A schematic diagram of the energy levels of a $\mu^+ - e^- - p$ system. Bottom: muon polarization curve calculated from eq. VI.4. 83

Figure VI.2. μLCR spectrum of $(CH_3)_2CCH_2Mu$ at 104.8 K, showing experimental data (o) and the best fit line. 85

Figure VI.3. Schematic representation of the SLC setup. 87

Figure VI.4. Block diagram of the electronics used for μLCR experiments. . 89

Figure VII.1. Radicals formed by addition of muonium to pyrogallol: 1,2,3-trihydroxycyclohexadienyl (I) and 2,3,4-trohydroxycyclohexadienyl (II). 91

Figure VII.2. Muonium decay rates as a function of pyrogallol concentration. 93

Figure VII.3. Fourier transform spectrum of pyrogallol in aqueous solution. The signals marked I and II arise from the cyclohexadienyl radicals whose structures are depicted in Figure VII.1. 96

Figure VII.4. μLCR spectra recorded for aqueous solutions of pyrogallol at 298 K. (a) 3 M and (b) 1 x 10^{-4} M. 97

Figure VII.5. Relative signal amplitudes for radicals I (o) and II (□) as determined from μLCR experiments on aqueous solutions of pyrogallol. 100

Figure VII.6. Polarized muonium fraction as a function of the chemical lifetime of muonium. 104

Figure VIII.1. Hyperfine coupling constants in $(CH_3)_2CCH_2Mu$. 112

Figure VIII.2. Definition of the ring positions and notation for Mu-substituted cyclohexadienyl radicals. 114

Figure VIII.3. Temperature dependence of the hyperfine coupling constants for the methylene substituents of C_6H_6Mu and C_6D_6Mu. 116

Figure VIII.4. Temperature dependence of ^{13}C hyperfine coupling constants for $^{13}C_6H_6Mu$. 117

Figure VIII.5. Muonium polarization as a function of density in C_2H_6 above (filled symbols) and below (closed symbols) T_c (305.3 K). ... 123

Figure VIII.6. Diamagnetic and total muon polarizations as a function of density in C_2H_6 above and below T_c. 124

Figure VIII.7. Muonium polarization as a function of pressure in N_2. 126

Figure VIII.8. Diamagnetic and total muon polarizations as a function of pressure in N_2. 127

Figure VIII.9. Radicals formed by addition of Mu to catechol, resorcinol, and hydroquinone. 131

CHAPTER I. INTRODUCTION

I.1. General background

The muon was the first unstable elementary particle detected [1]. It belongs to the small family of leptons. In 1937, Anderson and Neddermeyer discovered muons by the traces they left in photographic emulsions exposed to cosmic rays [1]. In 1948, muons were produced artificially at the 184 inch cyclotron at Berkeley by Gardner and Lattes [2]. Nowadays, they are produced routinely at the few meson factories around the world (*e.g.* the 520 MeV cyclotron TRIUMF at Vancouver, Canada; the 590 MeV PSI proton facility at Villigen, Switzerland; the KEK Booster Synchroton at Tsukuba, Japan; and the relatively new RAL accelerator near Oxford, England). Muons exist naturally in two charge states: the positive muon, μ^+, and the negative muon, μ^-. The present treatise will be limited to the positive muon which is a useful analogue of the proton.

The positive muon, μ^+, has the same charge and spin (½) as the proton but only has one-ninth the mass [3-8]. It is a transient particle and has a mean lifetime of 2.2 μs. Its magnetic moment is 3.1833 times that of the proton [3]. A summary of the properties of μ^+ is given in Table I.1.

The exotic atom muonium, Mu, consists of a positive muon in association with an orbital electron. This concept of a positive muon forming a bound state with an electron was proposed by Friedman and Telegdi to explain the depolarization of muon spins in nuclear emulsions in 1957 [9]. The first direct experimental observation of muonium in matter came in the year 1960, when Hughes *et al* reported the detection of the characteristic muonium signal in argon gas [10]. In

Table I.1. Physical properties of the positive muon

Positive Muon	μ^+
spin	1/2
charge	+1
rest mass	1.883566×10^{-28} kg 105.6596 MeV c^{-2} 1/9 mass of proton, m_p 206.76835 mass of electron, m_e
magnetic moment	4.49048×10^{-30} J G^{-1} 3.1833 proton magnetic moment, μ_p 4.834×10^{-3} electron magnetic moment, μ_e
magnetogyric ratio, γ_μ	13.5534 kHz G^{-1}
mean lifetime, τ_μ	2.197 μs

matter, Mu is formed when μ^+ captures an e^- from the medium during the final stages of its thermalization process [11].

Table I.2 is a summary of the fundamental properties of muonium [3-8]. Although the mass of the muon is only one-ninth the mass of a proton, it is still much more massive than the electron, so that the reduced-mass of muonium is essentially the same (within 0.5%) as that of normal hydrogen. Consequently, the electronic structure of muonium is very similar to that of ^{1}H, and muonium is generally regarded as an isotope of hydrogen.

The standard experimental technique for monitoring the precession signals of different muonic species in matter is known as μSR, which stands for "Muon Spin Rotation", "Muon Spin Relaxation", "Muon Spin Research" *etc.* This mnemonic acronym was chosen to indicate the close analogy with other magnetic resonance techniques such as NMR (Nuclear Magnetic Resonance) and ESR (Electron Spin Resonance).

In a standard μSR experiment, a beam of spin-polarized muons is introduced into a target where the muons are stopped. A magnetic field perpendicular to the muon spin polarization is applied to the target. The time evolution of the muon spin ensemble as a function of time is monitored via the asymmetric distribution of positrons produced in the muon decay. This technique allows the characterization of the amplitude (the fraction of the initial muon spin polarization which survives to precess coherently), relaxation, and, in some cases, the muon hyperfine coupling constant (hfcc). The details of this experimental technique will be given later.

Recently, the possibility of using muon level-crossing resonance (μLCR) spectroscopy in μSR experiments was suggested by Abragam [12]. This spectroscopic method allows the measurement of nuclear hyperfine coupling

Table I.2. Properties of muonium

Muonium	μ^+e^-
mass	207.8 mass of electron, m_e 1/9 mass of protonium, m_H
reduced mass	0.9956 μ_H (the reduced mass of ^1H)
Bohr radius	0.5315 Å 1.0044 Bohr radius (a_o) of ^1H
ionization potential	13.539 eV 0.9956 that of ^1H
magnetogyric ratio, γ_M	1.394 MHz G^{-1}
hyperfine frequency, ω_o	4463 MHz *in vacuum*
mean lifetime	limited by that of μ^+

constants other than those of the muon in muonium-substituted free radicals. This technique involves detection of the resonant transfer of spin polarization from a muon to other magnetic nuclei in the presence of a strong longitudinal magnetic field [13,14]. Since there is no requirement for phase coherence, radicals may be detected even if they are formed relatively slowly, up to the lifetime of the muon. This capability of μLCR is important to the field of free-radical chemistry, since the coupling constants of some radicals can not be measured by the conventional electron spin resonance (ESR) technique.

I.2. Muonium in aqueous solutions

Muonium was first detected in pure water in 1976 [15]. Since then it has been observed in a variety of liquids [4-7]. The spur model [16] has been accepted by most workers in the field as the explanation for the formation of Mu in the liquid phase [17]. This model describes the formation of muonium as encounters between positive muons and dry electrons produced in the radiolysis of water within the muon terminal spur. The formation of muonium is in competition with the hydration and escape of μ^+. The distribution of muons between muonium and diamagnetic states is completed at very short times ($t \leq 1$ ps), and the corresponding prompt chemical fractions are labelled h_M and h_D. At much later times depolarization by either chemical reaction or spin relaxation may occur and reduce the initial muon polarization to the fractions observed by μSR on the microsecond time-scale. The experimentally observed polarizations of the muonium and diamagnetic fractions are labelled P_M and P_D.

The literature values for the two muon signals detected in pure water in a μSR experiment are $P_D = 0.622 \pm 0.006$ and $P_M = 0.196 \pm 0.003$ [17]. The

remaining fraction (0.182) of the initial muon polarization has been dubbed "the missing fraction", P_L, so that $h_M = P_M + P_L$. The origin of the missing fraction has been a matter of debate in the μSR community. Percival *et al* explained the missing fraction as a result of spin relaxation of muonium during a non-reactive encounter with hydrated electrons, e^-_{aq}, produced in the terminal muon spur [16]. The encounter time-scale was estimated to be approximately 1 nanosecond. Similar explanations have been invoked for the missing fraction in ice [18], liquid inert gases [19], organic liquids and solids [20,21], and ionic solids [22].

A study in 1978 by Percival *et al* reported no variation of P_D in water as a function of applied field strength and they concluded that chemical reaction of muonium does not contribute to P_L [16]. However, a small but significant field dependence of P_D in pure water came to light during an investigation of residual polarization in the reaction of muonium with hydrogen peroxide [23]. This indicates chemical reaction of muonium may also contribute to the missing fraction.

The above literature values of P_D and P_M were determined by combining many measurements at "room temperature". It is now known that there is a variation of P_D with temperature amounting to several percent over water's liquid range [24]. However, the variation of P_M with temperature is not known.

I.3. Aims of this research

There have been tremendous improvements in μSR facilities in the last decade or so. It was the purpose of the present research to reinvestigate the properties of muonium in water. It involved the characterization of the missing fraction of the initial muon polarization as a function of temperature and pressure, by determining the muonium and diamagnetic fractions. In addition, the time-scale

of the spur process which leads to the missing fraction was deduced from residual polarization analysis of scavenger experiments.

The reaction of muonium with pyrogallol (1,2,3-trihydroxybenzene) in aqueous solution was studied by means of the μLCR technique. The amplitude of the radicals formed in the reaction as a function of solute concentration was used to determine the time-scale of the spur reaction which leads to the missing fraction.

Members of the Simon Fraser University μSR research group (also known as SFUMU in the μSR community) collaborate with μSR scientists from other institutions on a variety of topics. Some of these ventures are not relevant to the specific goals of the present dissertation. A chapter of this thesis summarises the collaborative works in which the author was involved.

CHAPTER II. MUON SPECTROSCOPIC TECHNIQUES I - μSR

II.1. Production and decay of μ^+

The positive muon is produced in the spontaneous decay of the positive pion along with a neutrino, as indicated in Eq. (II.1) [25],

$$\pi^+ \rightarrow \mu^+ + \nu_\mu \qquad \text{(II.1)}.$$

Pions are produced when a nucleus is bombarded with high energy particles. Typical nuclei used in modern particle accelerators are copper and beryllium and the nuclear reaction can be exemplified by

$$^9\text{Be} + \text{p} \rightarrow {}^{10}\text{Be} + \pi^+ \qquad \text{(II.2)}.$$

The minimum proton kinetic energy required for the production of pions in this reaction is limited by the rest mass of the pion, m_π = 140 MeV. The lifetime of the pion is 26 ns and its decay is exoergic by 34 MeV.

The muons produced in the decay of pions have energy of 4.1 MeV [25]. After an average lifetime of 2.2 μs the muons decay to give an energetic positron, e^+, and two neutrinos as given in Eq. (II.3) [3]:

$$\mu^+ \rightarrow e^+ + \nu_e + \bar{\nu}_\mu \qquad \text{(II.3)}.$$

The functionality of μSR relies on two conditions: the intrinsic polarization of the muons during their production from pions and the anisotropy of the positron emission in their subsequent decay – both are manifestations of parity violation processes [26]. While the positive pion is a zero-spin particle, ν_μ has negative

helicity and has a spin ½. In order to conserve linear and angular momentum, μ^+ has negative helicity and its spin is anti-parallel to its momentum in the pion's center-of-mass co-ordinate system. Therefore, a highly polarized beam of energetic muons can be produced by judiciously selecting the momentum of muons in the in-flight decay of the pions.

Muon decay also follows the same principles. The positron and ν_e have negative helicities while $\bar{\nu}_\mu$ has positive helicity. As a consequence of the conservation of energy, momentum, and angular momentum this three-body decay is spatially anisotropic. The angular distribution of positron emission has the greatest probability in the direction of the muon spin at the moment of decay. As a result, the variation of e^+ detection probability in a given direction reflects the evolution of the muon spin polarization.

The theoretical positron decay spectrum is given by the following expression [27]:

$$\begin{aligned} \frac{dR(w,\theta)}{dw\, d\Omega} &= \frac{w^2}{2\pi}\left[(3 - 2w) - P \cdot (1 - 2w)\cos\theta\right] \\ &= \frac{C}{2\pi}\left[1 + D\cos\theta\right] \end{aligned} \qquad \text{(II.4)}$$

where $w = E/E_{max}$ is the positron energy measured in units of the maximum possible energy $E_{max} = \frac{1}{2}m_\mu = 52.8$ MeV, θ and Ω are the angle and the solid angle between the spin of the decaying μ^+ and the e^+ momentum, respectively, and P stands for the degree of polarization of the decaying muons. The asymmetry parameter D is

a function of the positron energy

$$D = P \cdot \frac{2w - 1}{3 - 2w} \qquad \text{(II.5).}$$

The positron energy spectrum, C, and the asymmetry parameter D with P = 1 are plotted in figure II.1.

In practice, the positrons are detected with an efficiency $\xi(w)$ which will not be constant over the entire energy range due to absorption and scattering in the target and the counters as well as to the effect of an external magnetic field on the positron trajectories. The observed distribution probability is then given by equation II.6:

$$\frac{dR(\theta)}{d\Omega} = \int_0^1 \left[\frac{dR(w,\theta)}{dw d\Omega} \right] \xi(w)\, dw = \frac{\bar{\xi}\,(1 + \bar{A}\cos\theta)}{4\pi} \qquad \text{(II.6).}$$

where $\bar{\xi}$ is an average positron detection efficiency. If all positrons were detected with the same efficiency, the observed average asymmetry, $\bar{A}$, would be ⅓ P. However, the low energy positrons have a lowered detection efficiency in an actual experimental setup. This will result in an $\bar{A}$ greater than ⅓ P. On the other hand, this effect is counterbalanced by a reduction of the average asymmetry due to the finite detection angle subtended by the detectors. As a result, an expression containing an effective asymmetry A_D is used to describe the positron distribution

$$R(\theta) = 1 + A_D \cos\theta \qquad \text{(II.7).}$$

The resulting effective asymmetry varies from 0.22 to 0.3 depending on the geometry

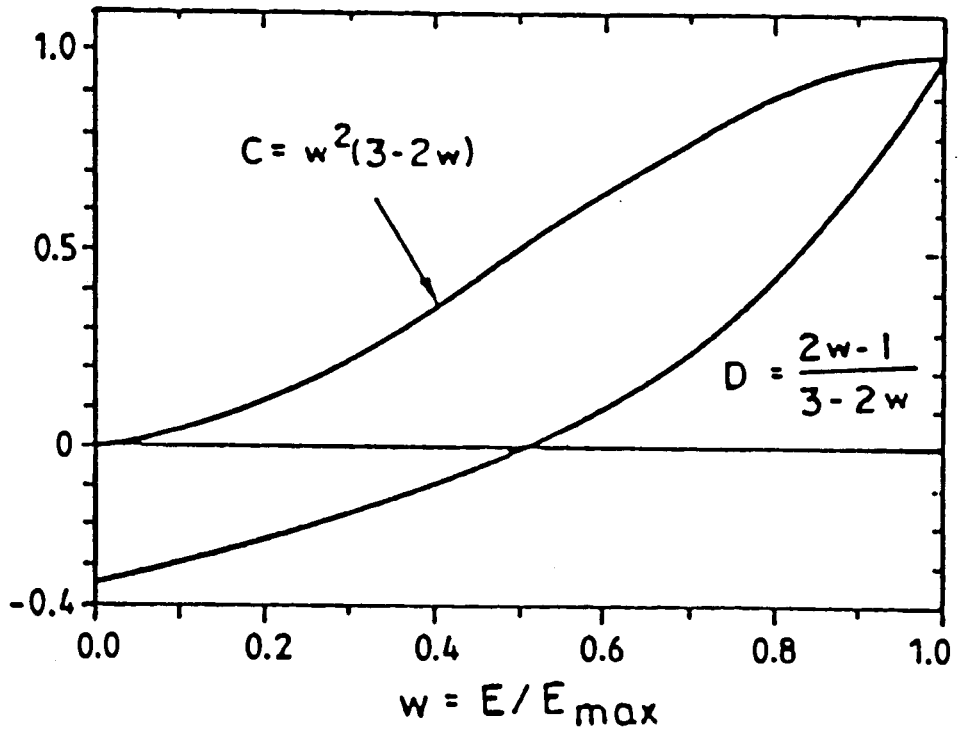

Figure II.1. Energy spectrum of positrons, e^+, from muon decay C (upper curve) and energy dependence of the asymmetry parameter D with P = 1 (lower curve).

of detector arrangements in different experiments. The average energy of the positrons is about 35 MeV [3]. This corresponds to a typical stopping range of $\approx$ 15 g cm^{-2}. Therefore, it is no problem to observe most positrons, even if the decaying muons are placed deep inside a target.

II.2. The transverse field μSR technique

In order to measure the magnetic interactions of the muon ensemble with the target material and their time-dependent effects on the polarization, the positron distribution has to be measured as a function of the elapsed muon lifetime, *i.e.*, in a time-differential fashion. For each implanted muon its individual lifetime and the direction of the emitted positron are measured in a μSR experiment. The muon lifetime is measured as the difference of the time at which the muon enters the sample and the instant at which a positron is emitted. The signature of an event is constructed such that only one muon might be present in the sample at any time. Subsequently, only one positron can be detected. Hence μSR is a single-particle-counting technique. The resulting positron counts are then displayed as a function of time. There are two types of μSR experiments in common usage: transverse field and longitudinal field [3-8]. The transverse field technique was utilized in this work and is described below.

By transverse we mean that the external magnetic field, B, is applied perpendicularly to the initial muon polarization. The muons stopped in the target will precess in a plane perpendicular to the direction of the magnetic field. A set of positron detectors is placed in the plane of the precession at an angle ϕ with respect to the muon spin. The Larmor precession frequency of μ^+, ν, is governed by the muon magnetogyric ratio ($\omega = \gamma_\mu \cdot B$). Because of the initial polarization of

the muons, all muons stopped in the sample will have the same initial phase of precession. For the positive muon the sense of precession is left-handed when viewing the precession in the direction of the magnetic field [3]. Since muon decay is spatially asymmetric, the probability of detecting the positrons emitted at a fixed solid angle rises and falls as the precessing muon spin swings passed the observation point. A schematic of a typical arrangement for the transverse field μSR experiment is given in figure II.2.

The number of positron counts in a particular direction is collected in a histogram. The general form of a μSR histogram is:

$$N(t) = N_0 [B + \exp(-t/\tau_\mu)] [1 + A(t)] \qquad \text{(II.8)}$$

where N_0 is a normalization factor determined by the solid angle of the positron detector and the total number of stopped muons. B is a time-independent background parameter which accounts for random accidental events. The asymmetry function $A(t)$ contains contributions from all muons in different environments. In the absence of muonium, $A(t)$ is given by

$$A(t) = A_D \exp(-\lambda t) \cos(\omega_\mu t + \phi) \qquad \text{(II.9)}$$

where ω_μ is the muon precession frequency and the amplitude parameter A_D represents the fraction of diamagnetic species. The first-order relaxation rate constant, λ, accounts for processes which cause a loss of phase coherence in precessing muon spins and an irreversible decrease in the oberved asymmetry in time (usually negligible for diamagnetic species).

Equation (II.8) is computer fitted to experimental data by varying the parameters to obtain the best values. A typical μSR time spectrum is shown is

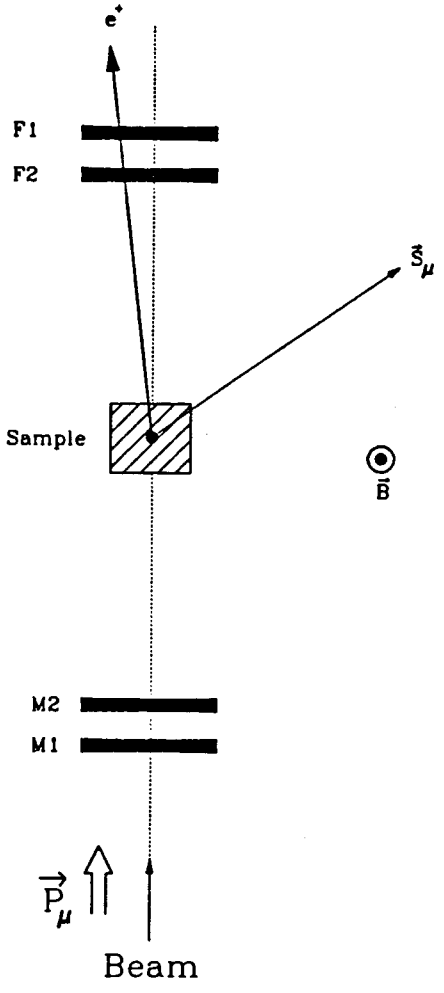

F1 and F2 = Forward positron telescope

M1 and M2 = Backward positron telescope

Figure II.2. Typical setup for a transverse field μSR experiment.

figure II.3. Its most dominant feature is the exponential muon lifetime upon which is superimposed the oscillating muon asymmetry.

II.3. The μSR spectrum of muonium

In muonium, the muon spin is coupled to the electron spin *via* the hyperfine interaction. Muonium has four spin states (the number of combinations for a two spin−½ system). However, the muons used in a μSR experiment are spin polarized initially while the electrons are not. Therefore, there are only two initially populated spin states of muonium. These spin states are defined as $|\alpha_\mu\alpha_e>$ and $|\alpha_\mu\beta_e>$, with the quantization axis being that of the muon polarization direction. The population of the two spin states is expected to be equal in such a system. For an isotropic hyperfine interaction the spin Hamiltonian, $\hat{H}$, can be written as [3]

$$\hat{H} = \nu^e S_z - \nu^\mu I_z + A_\mu \mathbf{S}\cdot\mathbf{I} \qquad \text{(II.10)}$$

where S represents the electron spin and I the muon spin. The four spin states are divided into a triplet state, ^{T}Mu, and a singlet state, ^{S}Mu, in zero magnetic field. In the presence of a magnetic field, the degeneracy of the triplet state is lifted. Figure II.4 shows the variation of the energy levels of the four spin states as a function of the strength of the applied field (*Breit-Rabi* diagram).

In a transverse field experiment there are four allowed precession frequencies. However, two of the frequencies are too high to be resolved by the conventional μSR technique, which has a timing resolution in the nanosecond regime. The muonium signal is superimposed on the diamagnetic signal in a transverse field μSR histogram. At low applied field (linear Zeeman region), the two observable frequencies are degenerate. This low-field precession frequency is approximately 103

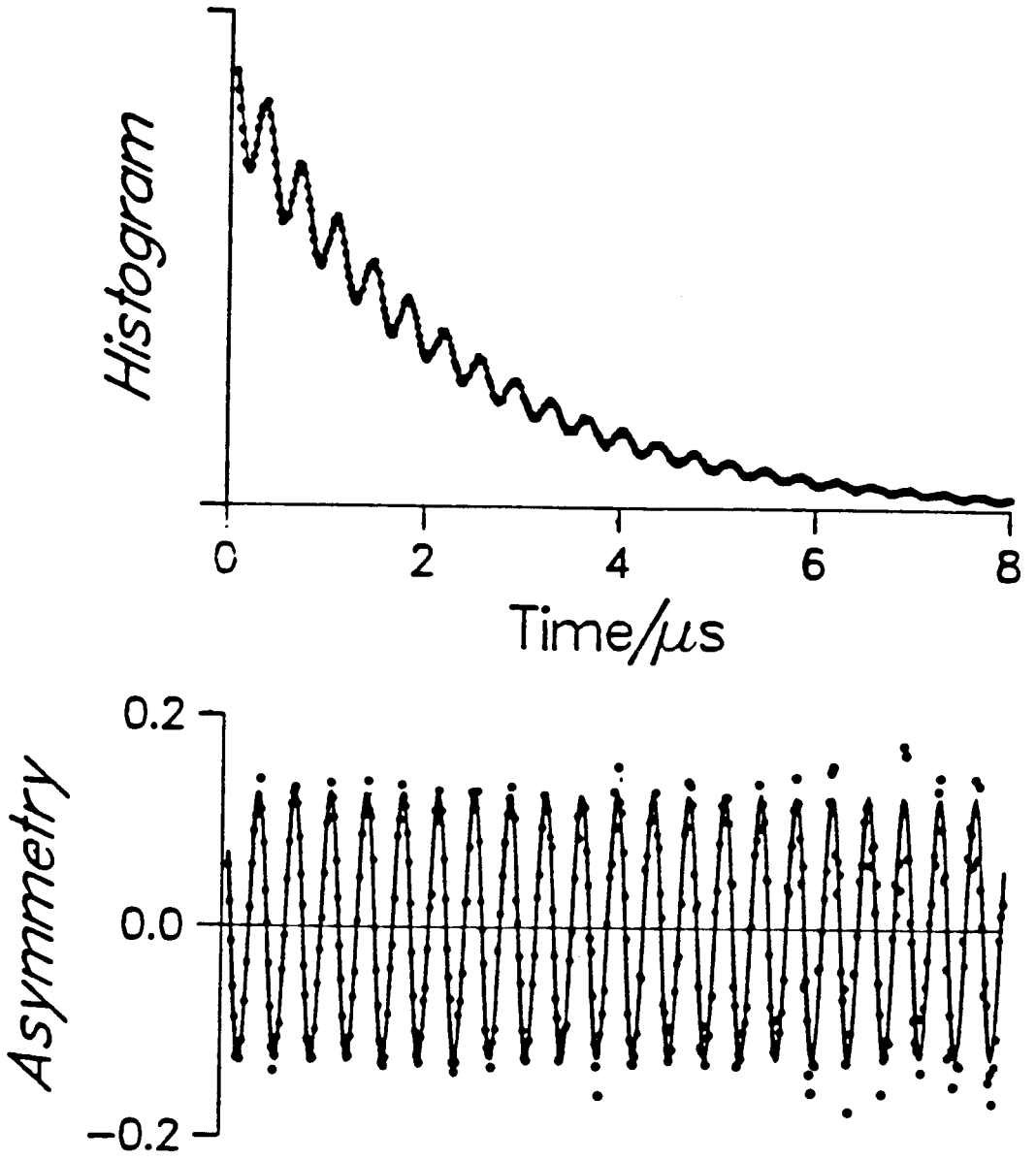

Figure II.3. μSR spectrum (top) and diamagentic signal (bottom) from water in a transverse field of 200G. The precession signal is obtained from the histogram by subtraction of the background and dividing out the exponential decay.

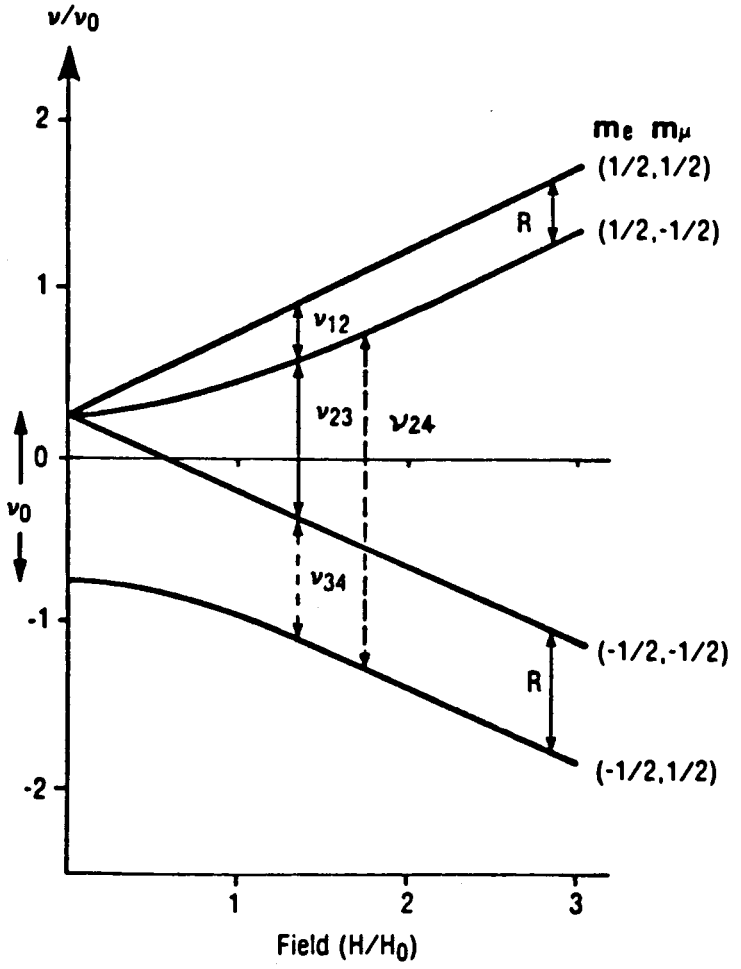

Figure II.4. *Breit-Rabi* diagram of the energy levels of muonium as a function of applied field. Of the four allowed transitions, only the two denoted by full lines are resolvable in a low transverse field μSR experiment.

times faster than that of the diamagnetic signal. At intermediate field strength, the degeneracy is lifted and the two observable frequencies give rise to a beat pattern. The frequencies are field dependent and the splitting can be obtained by Fourier transforming the time spectrum. At high fields, the Paschen-Back region (where the Mu electron spin is decoupled from the muon and other neighbouring nuclear spins) is reached and only two transitions are allowed. Muonium studies are mostly done in the low field limit where there is only one observable frequency.

The asymmetry parameter given in Equation II.9 is modified to include the contribution from muonium:

$$A(t) = A_D \exp(-\lambda_D t) \cos(\omega_D t + \phi_D) + A_{Mu} \exp(-\lambda_{Mu} t) \cos(\omega_{Mu} t + \phi_{Mu}) \quad \text{(II.11)}$$

with the same meanings for all the parameters as in Equation II.9 with the subscript D denoting the diamagnetic signal and Mu denoting the muonium signal. The parameter λ_{Mu} has more significance than its diamagnetic counterpart since muonium is a highly reactive species in most media. In fact, it is this high reactivity of muonium which delayed its direct detection in water until 1976 [15]. From this decay rate, the pseudo–first order decay rate of muonium can be determined. In the present research, this decay rate was used in the determination of the rate of slow formation of the muonium-substituted cyclohexadienyl radicals and the results are compared to that determined from μLCR.

II.4. The μSR spectrum for Mu-substituted radicals

Radicals are atoms and molecules with an unpaired electron. The irradiation of unsaturated organic liquids with μ^+ results in the formation of radicals isotopically substituted with a positive muon in place of a proton. Such radicals are formally

derived by addition of muonium to the parent molecule. The site of attack by Mu is at the double bond, as shown in equation II.12,

$$Mu + R_1R_2C{=}CR_3R_4 \quad \rightarrow \quad R_1R_2C{-}CMuR_3R_4 \qquad \text{(II.12)}.$$

Muonium always occupies the β position in the product. Consequently, the muon-electron hyperfine coupling is much weaker than in muonium. In the absence of other magnetic nuclei, the variation of the energy levels of the radical spin-system as a function of applied transverse field is qualitatively the same as that of muonium (shown in Figure II.4). In the presence of other magnetic nuclei, *e.g.* protons, the electron spin is also coupled to these nuclei. The spin Hamiltonian of the coupled system in a transverse field μSR experiment is given by [28]:

$$\hat{H} \quad = \quad \nu^e S_z - \nu^\mu I_z - \sum_k \nu^k I_{kz} + A_\mu \mathbf{S}\cdot\mathbf{I} + \sum_k A_k \mathbf{S}\cdot\mathbf{I}_k \qquad \text{(II.13)}$$

where ν^e, ν^μ, and ν^k are the Larmor precession frequencies of the electron, muon and the k−th nucleus. The subscript k used in all other parameters stands for the k−*th* magnetic nucleus. The Fermi contact hyperfine coupling constant A_i is assumed to be isotropic, which is usually the case in gases and liquids where tumbling and Brownian motion of the molecules result in averaging of any anisotropy. For N nuclei with spins I_n, the Hamiltonian leads to $4\prod_n^N(2I_n + 1)$ eigenstates. For low and zero-field ($\nu^e << A_\mu, A_k$) the selection rule for the spin system is $\Delta M = \pm 1$ and $\Delta F = 0, \pm 1$ where M is the total magnetic quantum number ($M = m^\mu + m^e + \Sigma_k m^k$) and F is the total spin quantum number of the total spin operator $\hat{\mathbf{F}}$ ($\hat{\mathbf{F}} = \hat{\mathbf{S}} + \hat{\mathbf{I}} + \Sigma_k \hat{\mathbf{I}}^k$). In this field limit, the spin system generally oscillates between many of these eigenstates. Consequently, the muon polarization

is spread out over many frequencies. This renders the detection of muonium-substituted radicals difficult, or close to impossible, by μSR at low field. However, in the high field Paschen-Back limit ($\nu^e >> A_\mu, A_k$), the spins are effectively decoupled. The selection rule for this high-field regime is given by $\Delta m^\mu = \pm 1$, $\Delta m^e = \Delta m^k = 0$. Under this condition, the time-differential μSR spectrum is simplified considerably, since the radical will have a signature cast by two frequencies [28]

$$\nu^+ = |\nu^M + \tfrac{1}{2} A_\mu|$$

and (II.14)

$$\nu^- = |\nu^M - \tfrac{1}{2} A_\mu|$$

where the parameter ν^M is given by

$$\nu^M = \tfrac{1}{2}\{[A_\mu^2 + (\nu^e + \nu^\mu)^2]^{\frac{1}{2}} - \nu^e + \nu^\mu\} \quad \text{(II.15).}$$

The μSR signals are usually analyzed in frequency space rather than in time space [29]. The Fourier transform of a μSR spectrum will consist of two radical frequencies on either side of the diamagnetic signal. The separation of the two radical frequencies provides an exact measure of A_μ. An example of a μSR Fourier transform spectrum for a muonium-substituted radical is given in figure II.5.

Mu-substituted radicals can be observed by conventional μSR techniques only if their formation rate is much larger than the precession frequency of its precursor, *i.e.* muonium. This puts a lower limit of 10^9 M^{-1} s^{-1} on the radical formation rate in order for this method to be effective. Mu-substituted radicals were mostly studied by μSR until the advent of the muon level-crossing resonance, μLCR, technique. The details of the μLCR technique will be given in a later chapter.

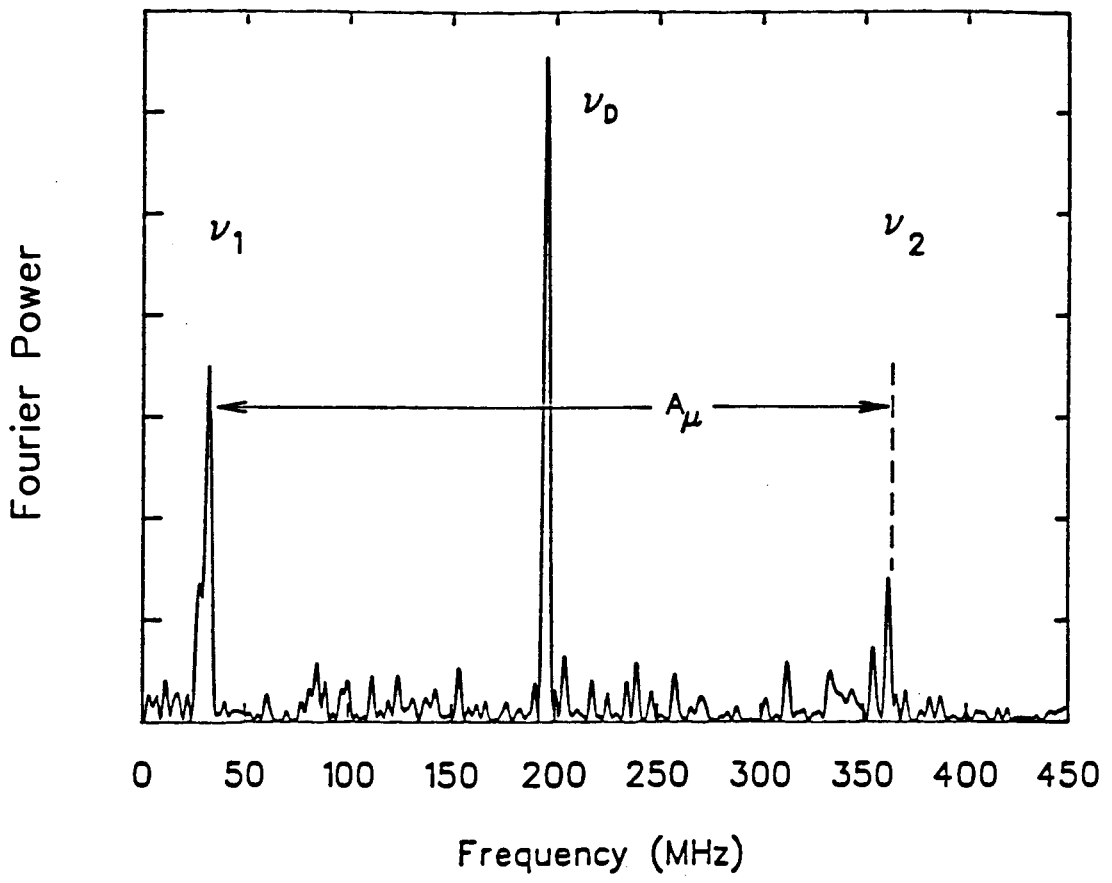

Figure II.5. Fourier transform spectrum of a Mu-substituted ethyl radical at 15 kG and 300K. A_μ of this radical is 331.1 MHz at 300K.

CHAPTER III. MUONIUM FORMATION IN AQUEOUS SOLUTIONS

III.1. Introduction

A qualitative understanding of the deceleration process of an energetic μ^+ and its subsequent thermalization in a target is helpful to the understanding of the behaviour of muons in matter and the formation of muonium. A brief overview of the radiolysis of water is given below.

III.2. Radiolysis of water

When high-energy charged particles enter water, they transfer their energies to the medium by inelastic collisions and elastic scattering [30]. The number of collisions that a particle undergoes depends on its incident energy. When the particle is thermalized, it may be neutralized by reaction with electrons or other ionization products. The rate of energy loss of the particle depends on its energy and charge and is given by the Bethe formula [31]:

$$-\frac{dE}{dx} = \frac{4\pi z^2 e^4}{m_0 v^2} NZ \left[ln \frac{2m_0 v^2}{I(1-\beta^2)} - \beta^2 \right] \qquad \text{(III.1)}$$

where N is the number of atoms per cm^3, Z is the atomic number and I is the mean excitation potential for the atoms of the stopping material. v, m_0, and ze are the velocity, rest mass, and the charge of the particle, respectively. e is the electron charge and β equals v/c where c is the speed of light. Thus, the slower the particle and the higher the magnitude of its charge, the larger is the rate of energy loss.

The energy lost when a charged particle is slowed down in matter results in a trail of excited and ionized atoms and molecules along the path of the particle.

This is known as the "track". Generally speaking, track species will be the same in a particular material regardless of the type or energy of the particles responsible. However, particles of different types and energy will lose energy in matter at different rates, and consequently will form tracks of different densities [32]. This accounts for the differences observed in the chemical effect of different particles. Track effects of this sort are more important in liquids than in gases since the active species are hindered from moving apart by the proximity of other molecules.

In the radiolysis of water, some of the water molecules in the vicinity of the track are excited. If the energy taken up is larger than the ionization potential of water, the following reactions take place in approximately 1 x 10^{-14} s [30]:

$$\begin{aligned} H_2O^{\bullet} &\rightarrow e^- + H_2O^+ \\ H_2O^+ + H_2O &\rightarrow H_3O^+ + OH\cdot \end{aligned} \qquad \text{(III.2)}$$

where e^- is a delocalized electron. The electrons form localized states in the solvent, which relax to the solvated state in about one picosecond [30] to give the hydrated electrons, e^-_{aq}. In general, the electrons produced in the radiolysis of water move further away from the point of ionization than the OH· radical since they are more energetic. Sometimes, they are sufficiently energetic to produce further ionizations and excitations. If the energy of these electrons is relatively small, less than about 100 eV, their range in condensed matter will be short [30]. Hence, the ionizations that they produce will be situated close to the original ionization, giving a small cluster or "spur" of excited and ionized species. The average spur has an initial diameter of about 20 Å in water [33]. It contains excited species and 2–3 ion pairs and corresponds to an energy deposit of 60 to 100 eV [34].

With densely ionizing particles (*e.g.*, α–particles) the spurs overlap and form

a "blob" or a column of ions and excited species about the track [33]. The energy deposited in a blob is in the range from 100 to 500 eV. Because of higher electron and radical concentration, blobs are expected to behave quite differently from spurs. Less densely ionizing particles give spurs at intervals along the track. An idealized representation of the distribution of ions and excited molecules is shown in figure III.1.

The processes described above occur less than a picosecond after the energetic particle enters the medium. The species produced (e^-, H_2O^*, H *etc.*) will undergo further interactions leading to the formation of free-radical products. These processes end with the reestablishment of chemical equilibrium. The expression for the radiation-induced decomposition of water,

$$H_2O \quad \rightarrow \quad H_3O^+_{aq},\ OH,\ e^-_{aq},\ H,\ H_2O_2,\ H_2 \qquad \text{(III.3)}$$

represents the state in irradiated water about 1 ns after the passage of the high energy particle, when the reactions in the spurs and blobs are practically terminated. These products are formed during radiolysis of water, regardless of the type of particles or radiation.

III.3. The hot atom model of Mu formation

When high energy muons (usually in the MeV regime in conventional μSR experiments) enter matter, their kinetic energy is first transferred to the medium at the rate given by the Bethe formula (equation III.1). At these high energies, little or no muonium is formed. As the velocity of the muons drops below that of the valence electrons of the medium, they begin to capture and lose electrons in rapid succession and interconvert between μ^+ and Mu as given by [35,36]

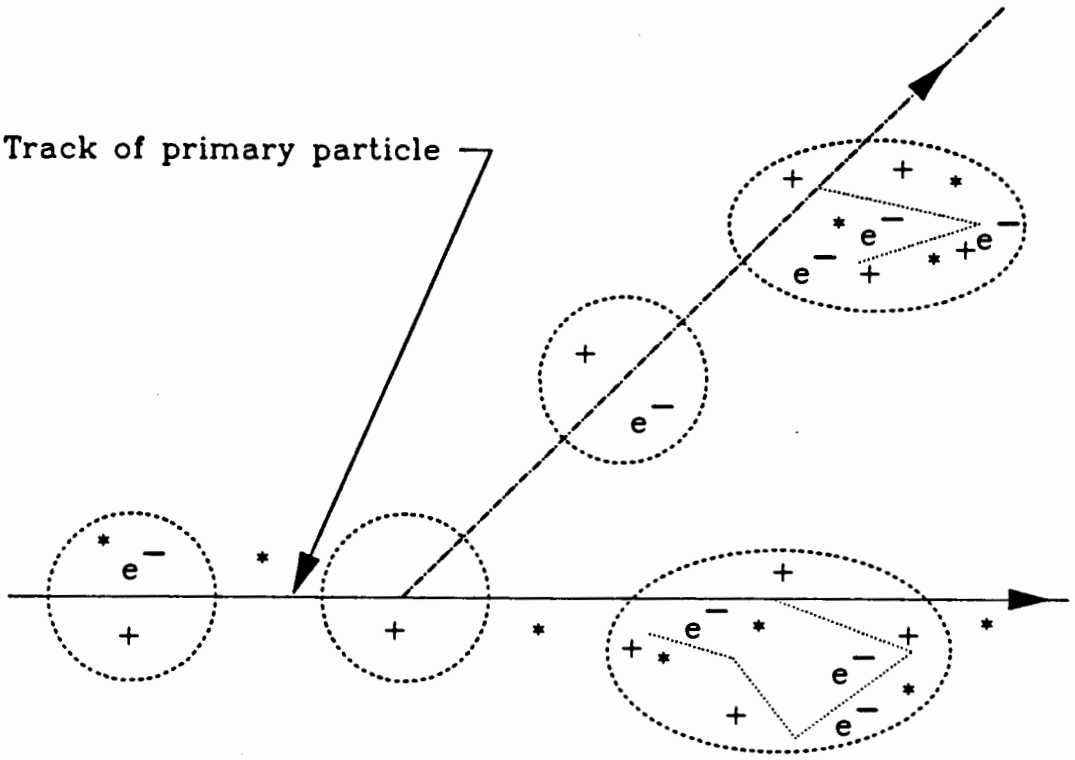

= isolated ionizations and spurs

= track of high-energy secondary electron

= track of low-energy secondary electron

\+ = positive ion

* = excited molecule

Figure III.1. Idealized distribution of ions and excited molecules in the track of an energetic particle.

$$\begin{aligned} \mu^+ + M &\rightarrow Mu + M^+ \\ Mu + M &\rightarrow \mu^+ + M^- \end{aligned} \qquad \text{(III.4)}$$

where M represents a molecule of the medium. During this sequence of charge-exchange cycles, the muons are slowed down to ≈30 eV and emerge as either bare muons or as muonium. The total time that the positive muon spends in the medium after its entrance until the end of the charge-exchange cycles has been estimated to be less than 0.5 picosecond for condensed phase [35]. This time is small when compared to the muonium hyperfine interaction (28 picoseconds). Thus depolarization of the muon spins within this time range is negligible. However, for low pressure gases, the time elapsed can be as long as 1 nanosecond and depolarization due to the muonium hyperfine interaction can be important [36,37].

After the charge-exchange cycle, the muons and/or muonium are thermalized via inelastic collisions with the molecules of the medium. During this last stage of thermalization, the muon and/or Mu can undergo hot atom reactions with molecules of the medium).[1] The most common hot atom reactions can be classified as follows:

1. Substitution reactions of the type

$$Mu^{\bullet} + XH \rightarrow XMu + H \qquad \text{(III.5);}$$

2. Abstraction reactions such as

$$Mu^{\bullet} + XH \rightarrow X + MuH \qquad \text{(III.6);}$$

[1] Hot atom reactions are chemical reactions that are usually improbable in the thermal region for lack of energy to overcome high activation barriers.

3. Addition reactions:

$$Mu^{\bullet} + X \rightarrow XMu \qquad \text{(III.7).}$$

The third type of reaction requires a deexcitation mechanism to carry away the excess energy in the product. It is likely that a free-radical can be produced this way if X contains a double bond. The remaining two types can also give rise to muonium-substituted paramagnetic molecules since there is a lot of energy available for reactions.

The observation of appreciable diamagnetic fractions in all molecular gases at low pressures was the primary reason for introducing the hot atom model. The sum of the experimentally observed polarizations of the different muonic species is equal to unity for gases at moderate pressures. For pressures below a few atmospheres, part of the muon polarization is lost due to the muonium hyperfine interaction [36]. However, this is recovered at even moderate pressures of a few atmospheres for most gases. As an example, for water in the gas phase, P_D = 11±2% and P_M = 89±2% with no missing fraction [37].

III.4. The spur model of Mu formation and the missing fraction in aqueous solutions

The spur model was introduced in the late 70's to explain μSR results in condensed media, primarily in aqueous solutions [16,17]. The idea of the spur model is based on an analogous concept developed by Mögensen for the thermalization of positrons and positronium, Ps, formation in condensed matter [40]. The essential features of the spur model are depicted in scheme III.1. It starts from a different viewpoint from the hot atom model, by assuming that the muon

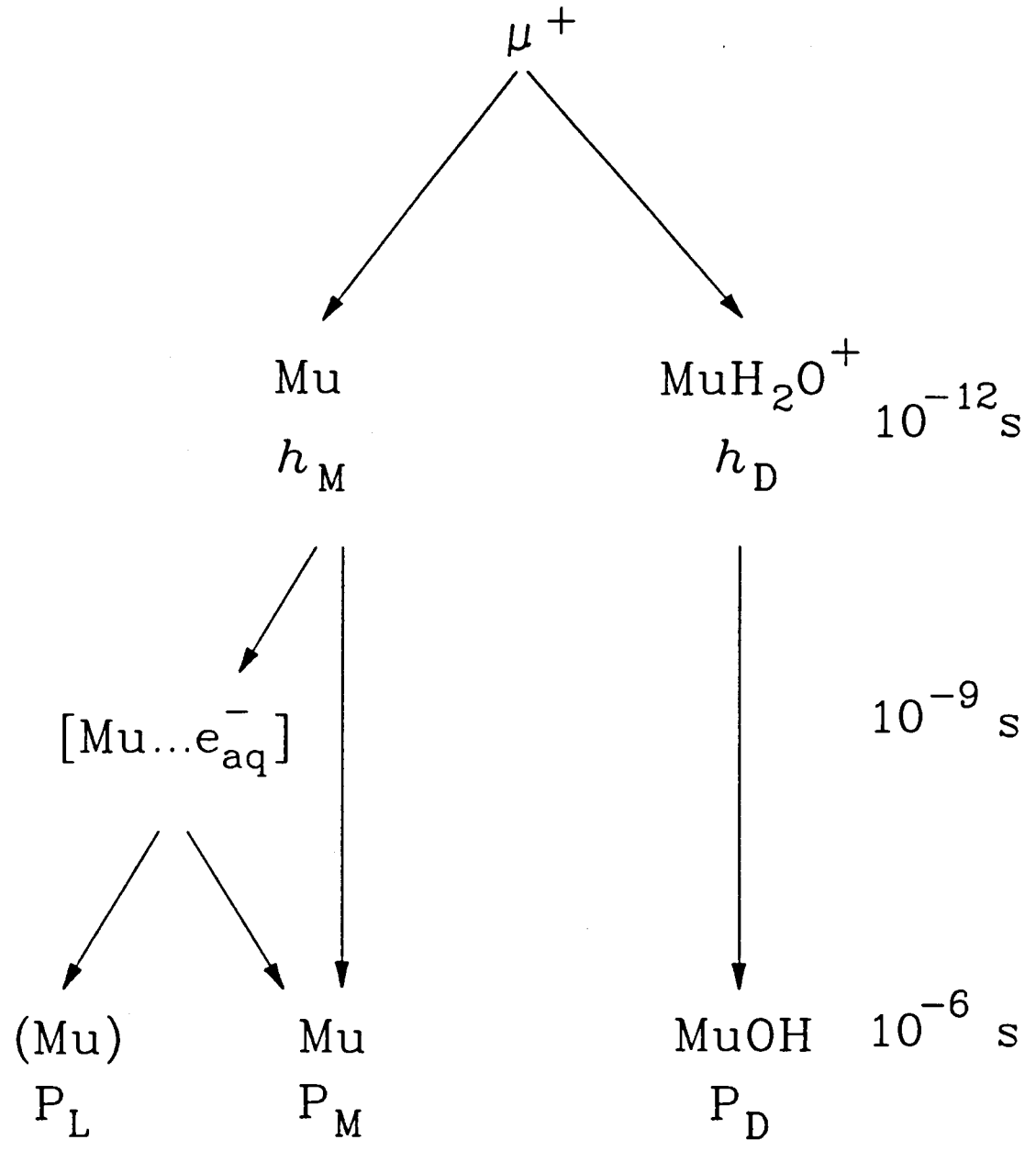

Scheme III.1. The essential features of the spur model

thermalizes close to the terminal spur of its track and that its fate is determined by reactions with transient species (e^-, OH, *etc*) formed in the radiolysis of the medium. The various muon fractions are determined by the outcome of competitive reactions between the muon and these spur transients. Muonium is formed when a μ^+ interacts with a hydrated electron. The formation of Mu competes with the hydration and escape of μ^+ and the radiolysis products of water from the spur. Muon hydration leads to the diamagnetic species MuOH via fast proton transfer to a neighbouring water molecule:

$$MuOH_2^+ + H_2O \rightarrow MuOH + H_3O^+ \qquad \text{(III.8)}.$$

The competitive rections are complete in $\leq$ 1 ps.

Competition between the various spur reactions depends on several factors related to the nature of the spur in addition to the usual kinetic parameters. These include the initial size of the spur, the number and distribution of reactive species, and their diffusion properties. Although theoretical and modelling studies have provided the relevant information for conventional radiation chemical systems (electrons or heavy ions passing through condensed matter) [32], essentially nothing is known about the end of the muon track. The way in which the spur changes with density of the medium is an additional source of uncertainty. In the low pressure limit, molecular ionization and excitation centers will be so well separated as to nullify the concept of the spur. Indeed, under such conditions there is negligible probability of encounter between the muon and radiolysis products. On the other hand, in condensed matter the epithermal muon interacts with the medium in many-body encounters, blurring the simple picture of sequential charge exchange events. In fact, the charge state of the muon following a molecular collision in condensed

matter can not be sensibly defined until the muon comes to rest [41,42]. Thus, ionization and excitation of the medium are expected to follow the muon to low energies, supporting the basic tenet of the spur model that the muon thermalizes close enough to the terminal spur transients to interact with them.

In aqueous solutions, since muonium is formed within the terminal spur, it can react with transient radicals in its vicinity, namely,

$$Mu + e^-_{aq} \rightarrow MuH + OH^- \quad \text{(III.9)},$$

$$Mu + OH \rightarrow MuOH \quad \text{(III.10)}.$$

It has been suggested that these reactions are responsible for the 20% of missing muon polarization, P_L [17].

In a longitudinal field μSR experiment, chemical reaction of muonium results in a maximum loss of $\frac{1}{2}h_M$ [43]:

$$P_{//} = h_D + \frac{1}{2}h_M [1 + \lambda^2/(\omega_{42}^2 + \lambda^2)] \quad \text{(III.11)}$$

where λ is the rate constant of the chemical reaction and ω_{42} is the transition frequency between E_2 and E_4 as shown in fig. II.4. However, the missing fraction found in pure water (0.18) is larger than $\frac{1}{2}h_M$ [17]. Therefore, it was concluded that the missing fraction was a result of spin relaxation of muonium [43]. Studies using different scavengers have positively identified the missing fraction in aqueous solutions as the result of interaction between muonium and hydrated electrons [16,43,44]. Similar suggestions have been made to explain the fast relaxation exhibited by half of the Mu signal in liquid Ar and for the missing fraction in liquid Kr and Xe [19].

CHAPTER IV. EXPERIMENTAL METHODS AND INSTRUMENTATION

IV.1. TRIUMF

There are only a few meson facilities in the world. The work realized in the present research was performed at TRIUMF,[1] Canada's national meson facility. TRIUMF has the world's largest cyclotron and provides experimental facilities for subatomic research with beams of muons, pions, protons, and neutrons. The cyclotron accelerates negatively charged hydrogen ions, H^-, up to an energy of 520 MeV. Beams of energetic protons are produced by removing the electrons of the ions by means of stripping foils. The intensity of the proton beams reaches 150 μA. The protons can be used in the production of pi-mesons. Because of the high intensity beams of pi-mesons available, TRIUMF is known as a "meson factory". The energy of the extracted proton beams varies from 60 MeV to 520 MeV. At TRIUMF, there are three stripping foils which allow the simultaneous extraction of three proton beams: Beam Line 1 (BL1), Beam Line 2 (BL2), and Beam Line 4 (BL4). This versatility makes TRIUMF unique among its peers. The layout of the TRIUMF facility and its experimental areas is depicted in figure IV.1.

The extracted proton beams are delivered to experimental stations located in two large experimental halls called the Proton Hall and the Meson Hall. An essential feature of TRIUMF which allows conventional μSR be done routinely is that the proton beams are continuous, *i.e.* the particles arrive at the experimental

---

[1] TRIUMF is an acronym for TRI University Meson Facility. It is jointly managed by four universities: Simon Fraser University, The University of Alberta, The University of British Columbia, and The University of Victoria. The operating fund of TRIUMF is contributed by the Canadian federal government through the National Research Council of Canada.

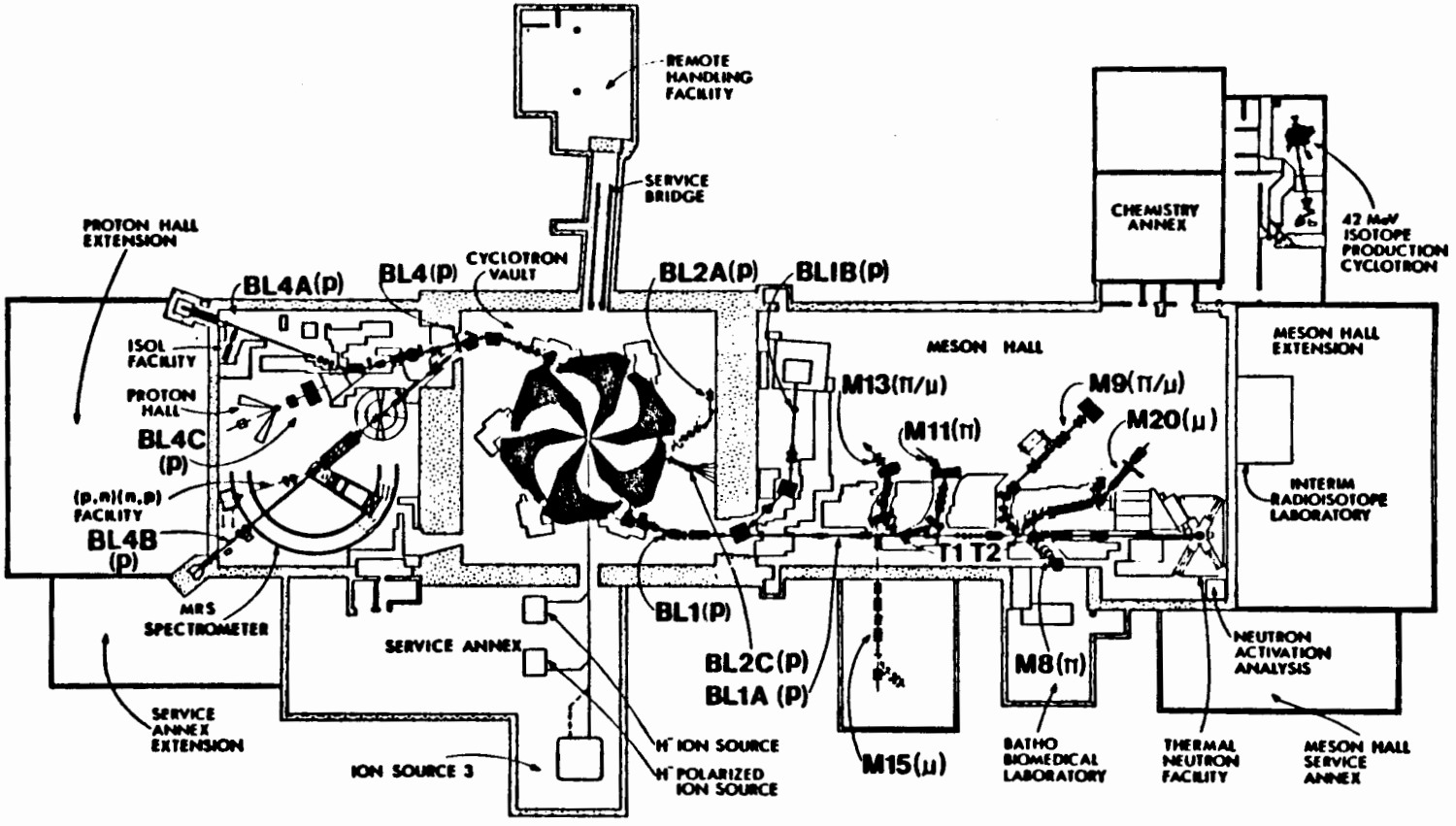

Figure IV.1. The layout of the experimental areas of the TRIUMF cyclotron.

target randomly. On a microscopic timescale, the cyclotron produces 3 nanosecond bursts of protons in 43 nanosecond intervals (the cyclotron frequency is 23 MHz).

The bulk of the experiments described in this thesis were carried out at the M15 and M20 channels. Figures IV.2 and IV.3 show the layouts of the two channels. The M20 channel has two legs. M20A is a decay muon channel, *i.e.* the muons are produced from the in-flight decay of pions, and backward muons are delivered to the experimental area. The M20B and M15 channels both deliver so-called surface muons, *i.e.* muons produced from pions which decay at rest in the production target. Details of these two different types of muon beam will be given in the next section. In these secondary beam lines, dipole bending magnets (designated with the letter B for "bender") are used to steer and select the momentum of the beam particles from the production targets. Quadrupole magnets (designated with the letter Q) are used for focusing. In M20, the section of the beam line between M20Q5 and M20Q6 is used for the decay of pions. When operating in this mode, the muons produced are directed to M20A.

Both the M20B and M15 channels employ a Wien filter (dc separator) [45]. When operated at low voltages, the Wien filter can minimize contamination of the beam by positrons. In high-voltage mode, the dc separators are used as spin rotators. μSR spectra obtained in these two channels generally have lower backgrounds than those obtained in M20A.

IV.2. Different types of muon beam produced at TRIUMF

There are three types of muon beam that are available for experiments, namely, the forward, backward, and surface. The forward muon beam has the highest energy of the three. This beam is rarely used due to the high stopping range

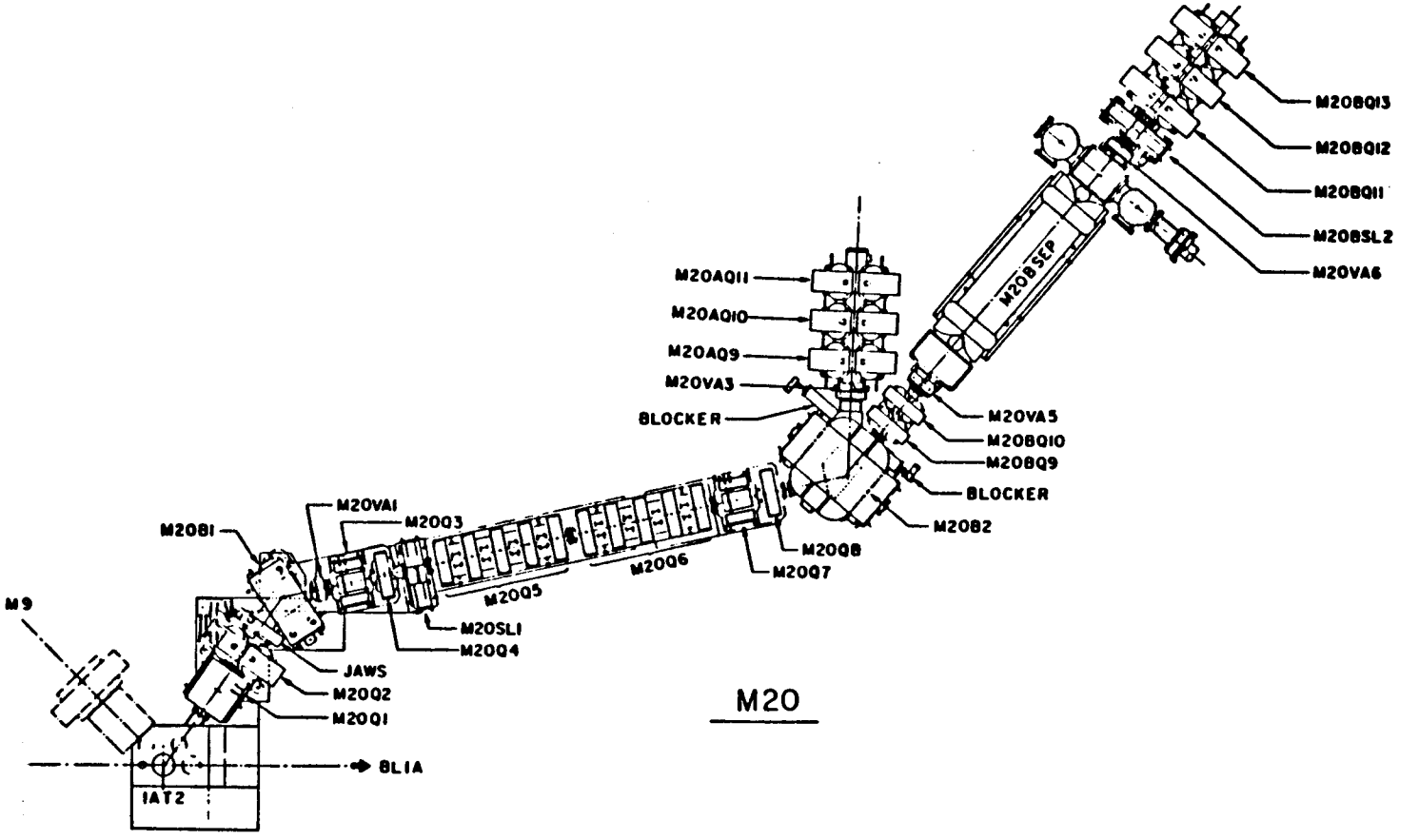

Figure IV.2. The layout of the beamline magnets of the M20 muon channel.

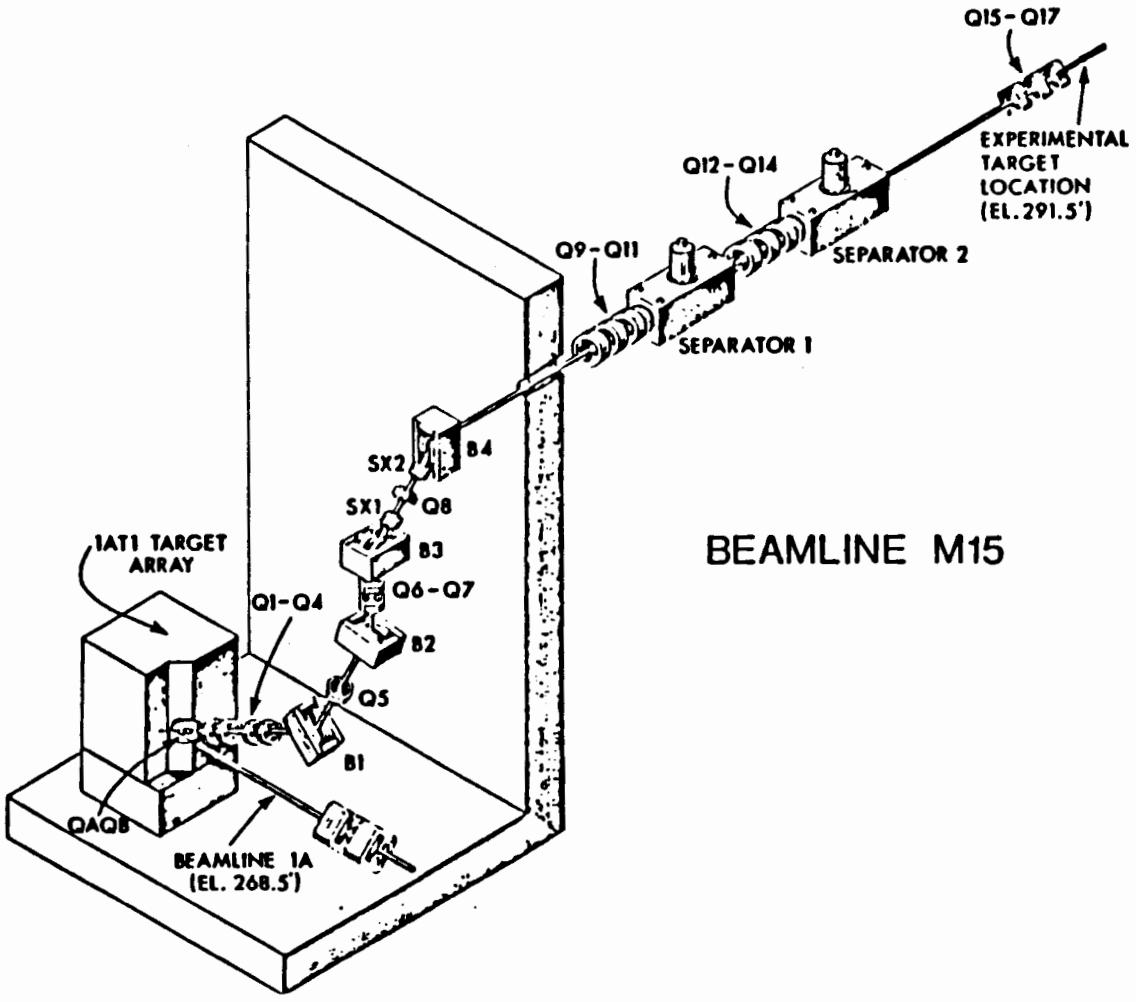

Figure IV.3. The layout of the beamline magnets of the M15 muon channel.

($\approx$35 g cm^{-2}) and high degree of contamination of pions, positrons and protons.

The backward muon beam has polarization of 60-80%. The positive pions produced at the production target T2 are collected by the quadrupole doublets of M20Q1 and M20Q2 and are bent by the dipole magnet B1 to select the appropriate particle momentum before they are injected into the decay channel between M20Q5 and M20Q6. The momenta of the muons are selected by the second bender B2. The muon beam is focused by the last few quadrupoles before it is delivered to the experimental area. The momentum range is from 60-120 MeV/*c*. The standard backward muon momentum used in M20A is 86.5 MeV/*c*. The stopping range of these muons in matter is about 5 g cm^{-2}. With this stopping range, moderation of the particle incident energy by a degrader is sometimes necessary to stop the particles completely in the target. The degrader material is typically graphite or water. The thickness of the degrader is usually made adjustable so as to allow for optimization of stopping rates in the sample.

A surface muon beam usually has 100% muon polarization. Surface muons are produced from the decay of pions that are at rest near the surface of the production target. The nominal momentum of these muons is 28 MeV/*c*. Their stopping range is 0.15 $\pm$ 0.01 g cm^{-2}. This corresponds to a penetration depth of about 0.2 mm in copper, 1.5 mm in water, or 1 m in He gas at STP, for instance. This makes surface muons ideal for the study of gases at low pressures, thin or rare solids, or small quantities of liquid held in thin-walled cells. A thin muon counter and thin windows for cryostats are used in experiments to allow the entrance of muons into the sample. No additional degrader is necessary since the sample will stop all incident muons. For certain experimental setups, surface muons of different momentum (up to a few percent from the nominal value) can be selected to allow

for a reasonable stopping distribution within the sample volume.

There are disadvantages when surface muons are used in an experiment. Due to their low energy and momentum, they are readily affected by the external field. Their radius of curvature is less than 1 m kG^{-1}, which implies beam bending in high transverse field will be significant. The installation of dc separators in M15 and M20B at TRIUMF to rotate the muon spin with respect to its momentum axis has eliminated this problem. The spin rotator consists of crossed magnetic and electrostatic fields (a vertically oriented electric field and a horizontally oriented magnetic field). As the magnetic field can change both the spin and the momentum of the muons while the electric field only affects the muon momentum, a suitable combination of electric field and magnetic field will allow the rotation of the muon spin with its momentum unchanged. Thus a single apparatus, when equipped properly, can be used for a longitudinal field experiment with unrotated muons and a transverse field experiment with transversely polarized muons.

IV.3. Transverse field μSR experiments

The transverse field experiments described in this thesis employed both backward muons and surface muons. The longitudinally polarized backward muons were used for the high pressure residual polarization study of water, since the window of the high pressure cell used is too thick for surface muons to penetrate. Transversely polarized surface muons were used for all other transverse field μSR studies. The experimental setup for longitudinally polarized muons will be described in detail below. A similar setup was used for transversely polarized surface muons.

The apparatus used for longitudinally polarized muons was SFUMU, which

was designed specifically for backward muon experiments.[2] It consists of a set of Helmholtz coils, a variable water degrader (controlled remotely) and two (more if necessary) collimators. The collimators are for limiting the diameter of the beam spot. This apparatus can deliver a homogeneous magnetic field of up to 4 kG over the sample area (6-8 cm in length). The muon counter B is located between the degrader and the collimators. For regular μSR experiments, four sets of positron telescopes can be installed on SFUMU. However, because of the size and shape of the high pressure cell used for the present set of experiments, the installation of a forward positron telescope proved to be too cumbersome and only three pairs were used. Furthermore, the second counter of the backward telescope is a veto counter. It is basically a regular positron telescope with a hole approximately the same diameter as the cell window. A positive signal registered by this counter signifies a muon which enters the sample obliquely with a very high probability of stopping in the cell instead of the sample, and is subsequently counted as a bad event. A schematic drawing of the SFUMU apparatus is given in figure IV.4.

IV.4. The data acquisition system for transverse field μSR experiments

The data acquisition system used was the standard TRIUMF μSR setup. For the experimental setup to register a muon stop in the sample, the muon must pass through the B counter and the back counter M_1. If the muon is going to stop in the sample, it should pass through the hole of M_2 which should show no response. If a signal is registered by M_2 in coincidence with B and M_1, it means that a muon has

---

[2] SFUMU, as its name suggests, stands for the Simon Fraser University MU spin rotation group. Although SFUMU nominally belongs to the SFU experimenters, it is shared with other TRIUMF μSR users and remains at TRIUMF while not being used.

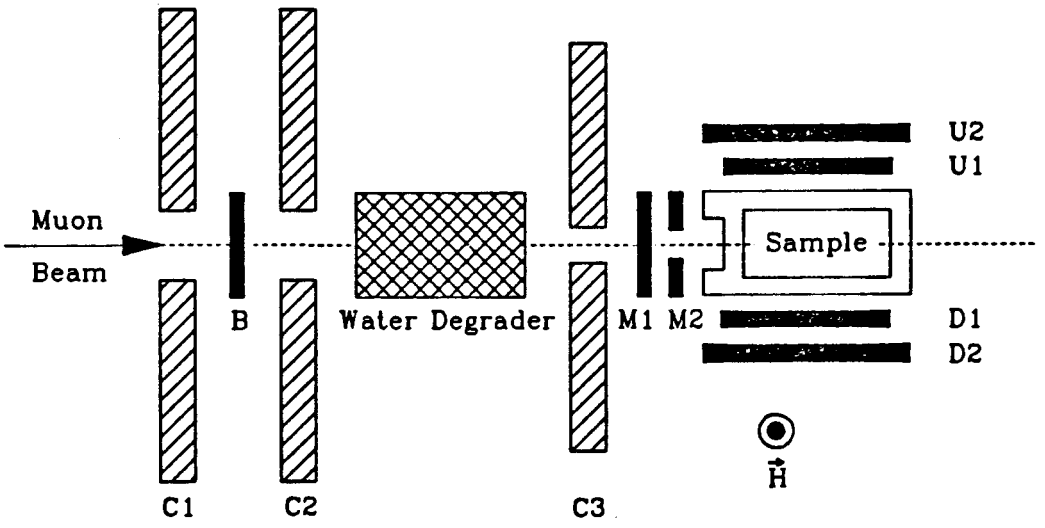

C1, C2 and C3 are collimators

B = Back counter

M1 and M2 = Backward telescope

U1 and U2 = Up telescope

D1 and D2 = Down telescope

Figure IV.4. The SFUMU apparatus setup for transverse field μSR experiments.

entered the sample obliquely and the event should be vetoed. Therefore, the muon start signature is $B \cdot M_1 \cdot \bar{M}_2$. By the same token, simultaneous responses from the U_1 and U_2 counters signify a decay positron detected in the upward direction and the logic signature of this is $U_1 \cdot U_2$. Similarly, the logic signature $D_1 \cdot D_2$ represents a decay positron detected by the downward telescope. The backward counters can also serve as a positron telescope and the corresponding positron signature is $\bar{B} \cdot M_1 \cdot M_2$.

The electronic diagram for this setup is given in figure IV.5. The signals from the counters are converted to standard Nuclear Instrument and Measurement (NIM) pulses with a width of ≈20 ns. These pulses are routed through time-delay circuits for time synchronization before they are fed into various electronic units. The muon start signature triggers two devices: a clock and a data gate. The function of the data gate is to set up a time interval after a good muon stop within which the decay positron corresponding to the incoming muon must be detected. After this time interval, the data gate will stop the clock, reset itself and wait for another good muon signature. When a good positron signal is registered by either of the three telescopes within the data-gate interval, the clock is stopped. The elapsed time forms the address of a histogram memory, and the content of the corresponding channel is incremented by one. When data of sufficient statistics (usually 10^6-10^7 per histogram) have been accumulated, the run is stopped.

There are other experimental considerations. For instance, after the data gate is triggered by an incoming muon, another muon can still come into the sample within the time interval set by the data gate and before the detection of the decay positron. There are now two muons within the sample, and the subsequent decay positron detected by the telescopes can not be related unambiguously to the parent

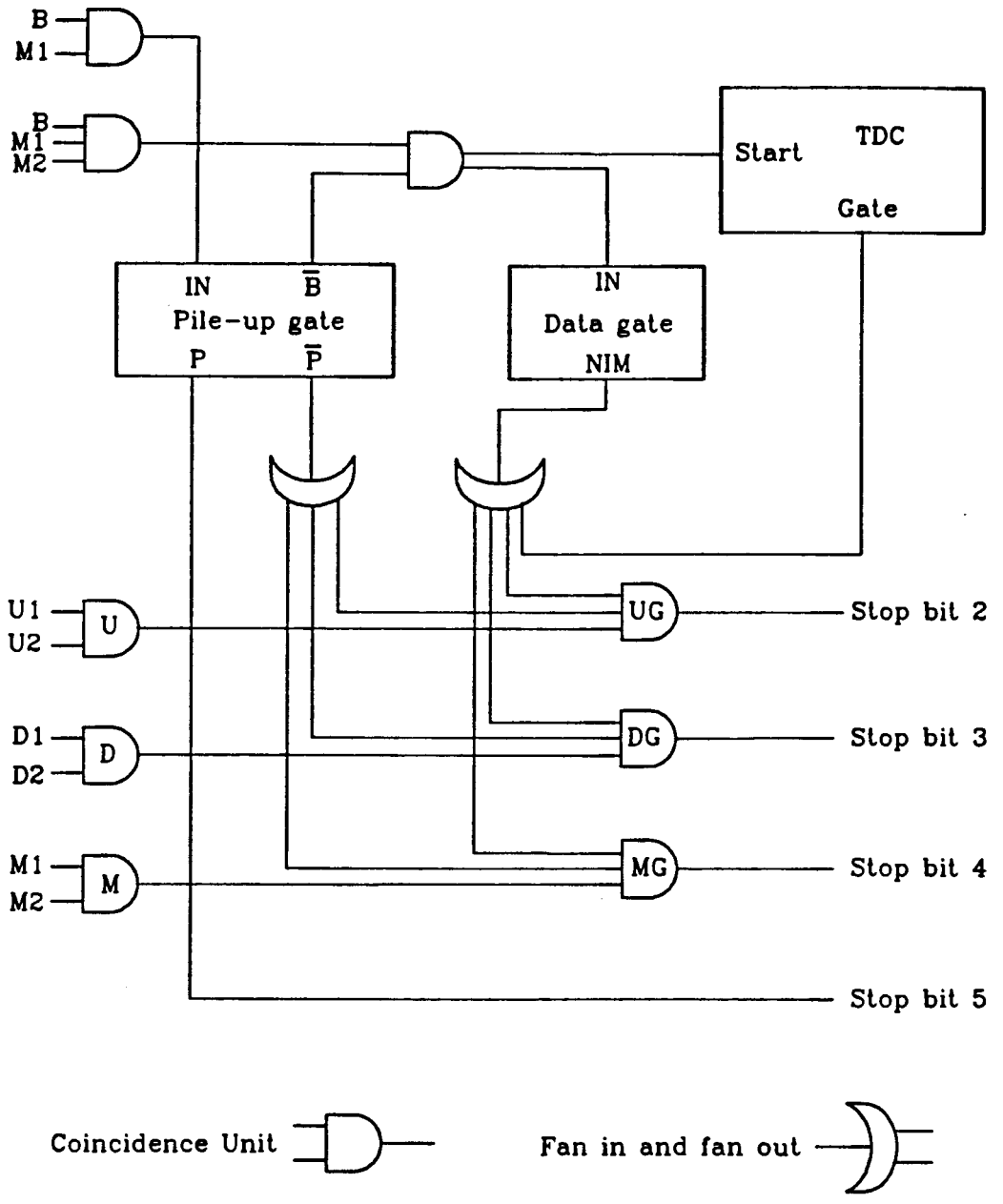

Figure IV.5. The principal electronic components of the time-differential μSR setup.

muon. This ill-defined event must be rejected. Furthermore, it is important to exclude second muons which enter the sample after the detection of the decay positron within the interval of the data gate. These events will result in histogram distortions since the observation of long-lived muons has a larger probability of suppression by second muons than that of the short-lived muons. These problems are avoided with the installation of a pile-up gate. The problem of second positrons (from muons which hit the edge of the counters, collimators, and the degrader and not detected by the muon telescope) is eliminated by software.

IV.5. Data analysis

The appropriate theroetical expression was computer fitted to experimental μSR spectra. The computer program used was MINUIT, written by James and Roos [46]. It involves a non-linear chi-square least-square minimization procedure to fit a theoretical expression to experimental data and calculate the parameter errors and correlations.

IV.6. Particle detectors

The particle detectors comprise scintillators, lightguides and photomultuplier tubes. These can be used singly (counters). More commonly, pairs of them are used in coincidence to eliminate electronic noise and to obtain some telescopic effect (telescopes). The detectors used are plastic organic scintillators. These scintillators are fluorescent compounds dissolved in a solidified polymer matrix. Typical compounds are *para*-xylene, benzene, and 2,5-diphenyloxazole (PPO). The fluorescence lifetimes of these materials are typically on the order of 1 nanosecond. Common compounds used in the polymer matrix are polystyrene and

polyvinyltoluene. Small amount of additives such as PPO are used in the matrix to enhance scintillation efficiency.

A simplified schematic diagram of a detector assembly is given in figure IV.6. The light emitted by the scintillator during the fluorescence process is collected by a light guide and conducted to the photomultiplier for amplification and conversion to an electrical signal. Because of their sensitivity to light, the scintillators and the lightguides are wrapped in black tape. Depending on the application, the lightguides can be moulded into various shapes and lengths. Since the high fields used in the μLCR experiments affect the efficiency of the photomultipliers, the lightguides used in the SLC and HELIOS apparatus were over 1 meter long.

High voltages applied to the phototube for the present experiments ranged from 1.8-2.5 kV, depending on the sensitivity of the tube used. For optimum performance, the phototubes on the SLC and HELIOS apparatus were shielded from the magnetic fields.

IV.7. Sample cell, sample handling and temperature control

The sample cell described here was used in all but the high pressure experiments. The details of the high pressure cell will be given in Chapter VI. The cell is cylindrical in shape and its body is made of teflon. A schematic drawing of the cell is given in figure IV.7. There are two windows made of Mylar with the space in between the two windows acting as an insulating volume. During the later stage of experiments, N_2 gas was bubbled through this space to ensure that O_2 did not leak into the sample volume. A copper plate with copper coils soldered onto the back was attached to the back of the cell. Thermostatting fluid was circulated through the coils. Thermally conducting grease was used between the copper plate

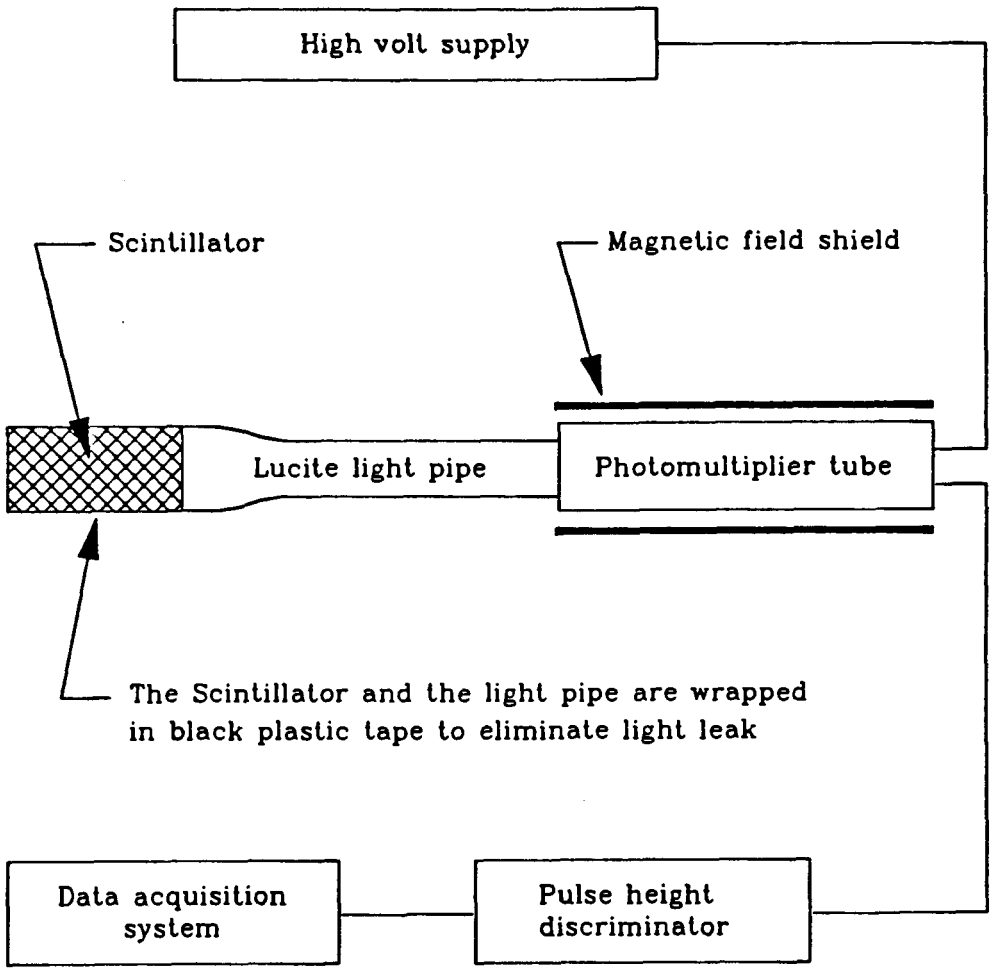

Figure IV.6. Schematic drawing of a particle detector.

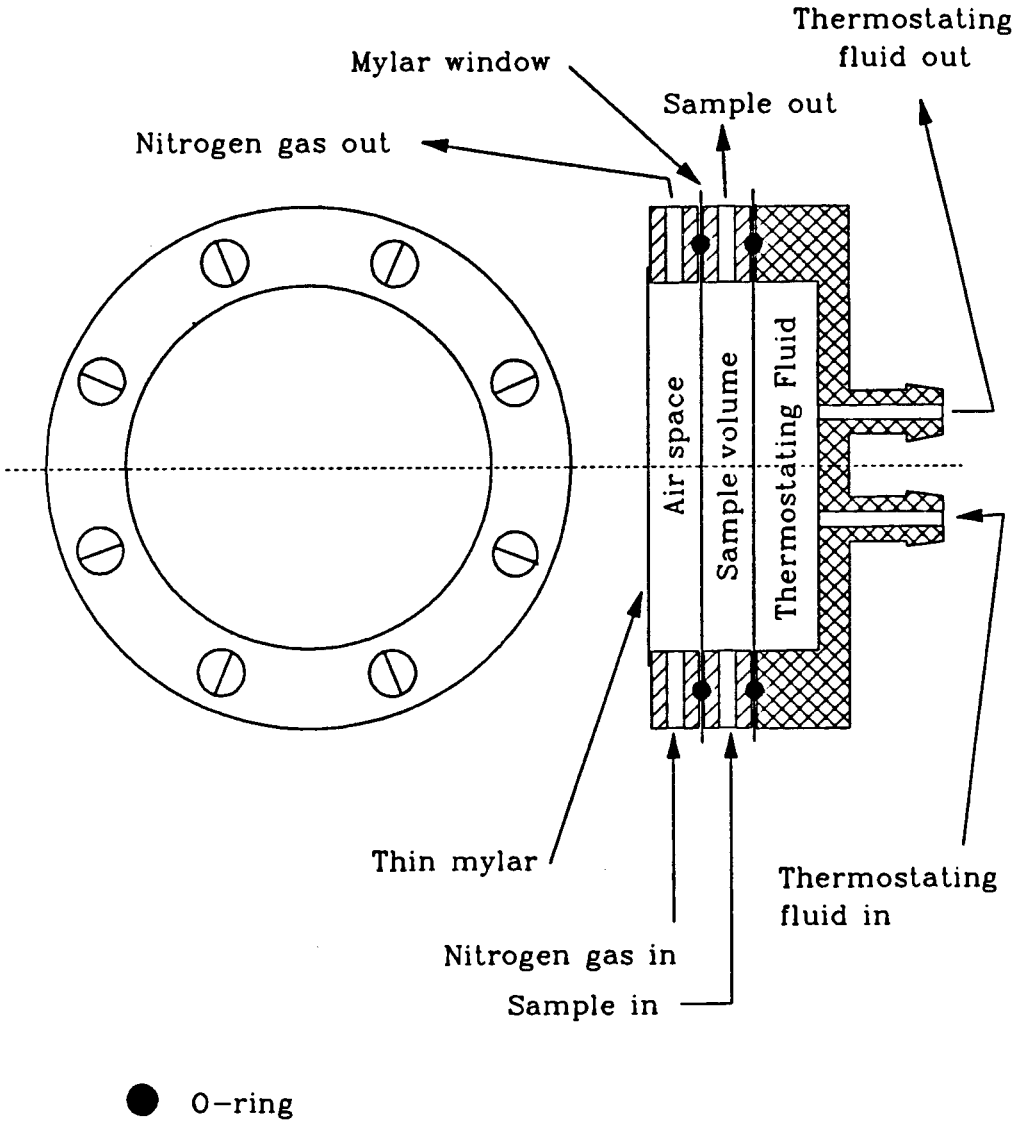

Figure IV.7. A schematic representation of the sample cell.

and the back of the cell. A variation of this cell was used with HELIOS. The body of this cell was made of glass. Thermostatting fluid was circulated in a compartment at the back of this cell.

The samples were bubbled with nitrogen before the experiments. After each experiment, the cell was rinsed several times: first with distilled water then with the new sample, before it was filled. Samples were pumped in and out of the cell to ensure reproducibility of sample position with respect to the scintillator detectors. The sample was bubbled with nitrogen during the course of the experiment to minimize the risk of contamination by atmospheric oxygen. A diagram of the flow system used is given in figure IV.8.

The temperature of the thermostatting fluid was controlled by a constant-temperature bath. The tubes which connect the temperature bath to the back of the cell were insulated in order to minimize the temperature gradient between the bath and the sample. In spite of this, there was still a discrepancy of a few degrees at extreme temperatures (0° and 50°C). In view of this, a temperature sensor (type K copper-constantan thermocouple) was embedded between the cell and the copper plate to measure the sample temperature. It was found that this temperature closely represented that of the sample, and that the variation of temperature over the sample volume was less than 1°C.

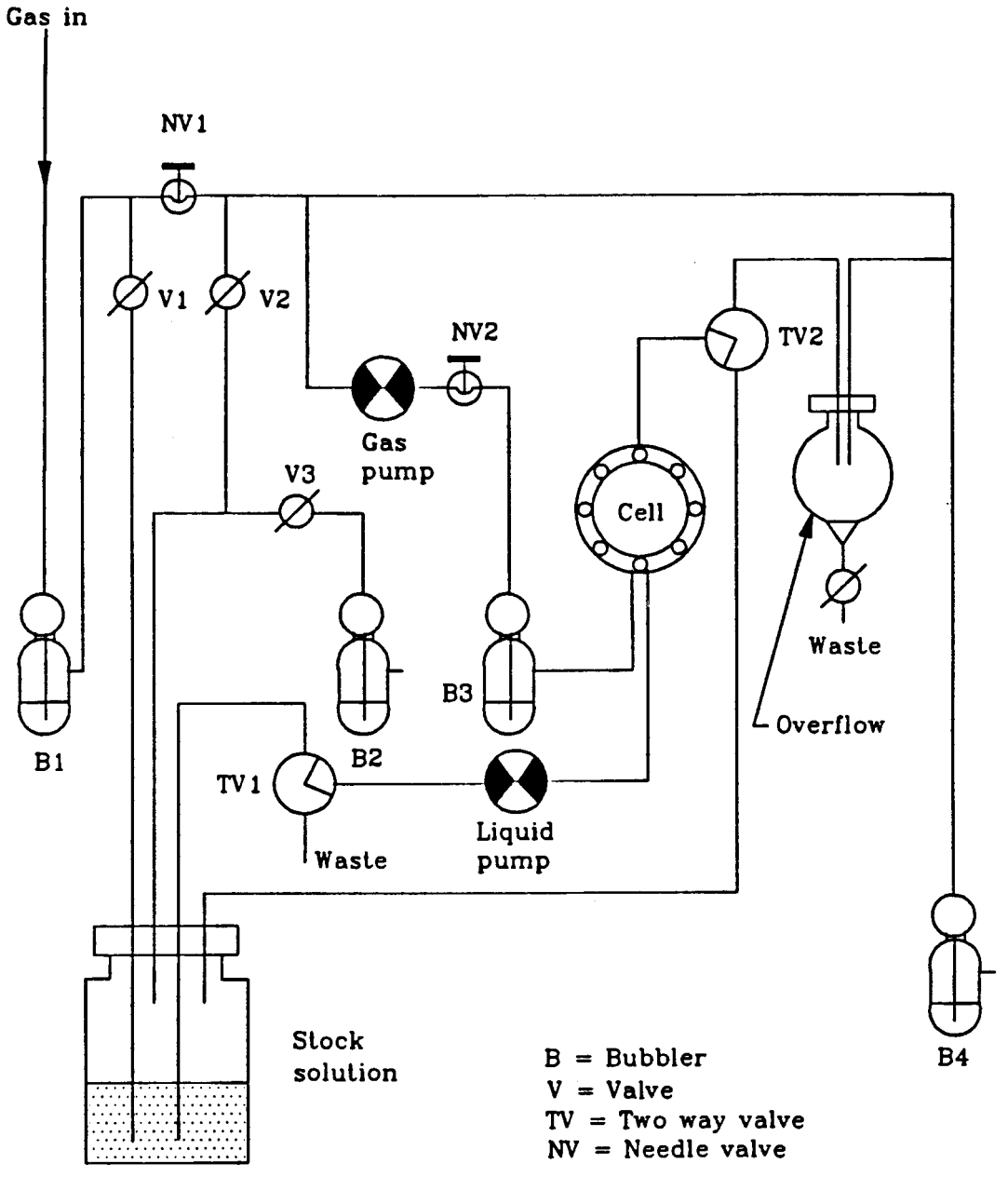

Figure IV.8. The flow system used for sample handling.

CHAPTER V. THE REACTION OF MUONIUM WITH HYDRATED ELECTRONS

V.1. Introduction

In pure water two distinct μSR precession signals can be detected, and are attributed to muonium and muon-substituted diamagnetic species. Their amplitudes correspond to fractions of muon polarization $P_M = 0.196 \pm 0.003$ and $P_D = 0.622 \pm 0.006$, respectively [16]. The remaining fraction (0.182) of the initial muon polarization has been dubbed "the missing fraction", P_L. It is important to realise that polarization fractions (P_i) provide only a lower limit to the mole fractions h_i of the corresponding chemical species. Two mechanisms serve to reduce the initial muon polarization to the fractions observed by μSR on the microsecond time-scale: spin relaxation and spin dephasing. In published reports on the missing fraction in water, the former was emphasized [16,18,43,44]. The explanation of the missing fraction in water was first introduced as part of the spur model, a general description of muon radiolysis effects [16]. When applied to muonium the term "spur model" encompasses both the early radiolysis events associated with muonium formation, and the much slower processes leading to the development of the missing fraction. Muonium formation results from the combination of a stopped muon (at or close to thermal energy) with one of the excess electrons created during the slowing down process. In competition with this is muon hydration, which leads to MuOH. In this version of the model the measured diamagnetic fraction, P_D, equals the initial fraction, h_D. Muonium, however, is partially depolarized by spin-exchange encounters with e^-_{aq} on a nanosecond time-scale, so that $h_M = P_M + P_L$.

In addition to spin relaxation, loss of spin coherence also results in reduced

μSR signal amplitudes. This happens when one muonic species reacts to give another with different precession frequencies. The loss depends on the rate of reaction and the difference in precession frequencies, and is therefore magnetic field-dependent [47]. The fraction of muon polarization retained in the product of the reaction is termed the residual polarization, P_{res}. For reaction of Mu to give a diamagnetic product at a first-order rate constant of λ_M

$$P_D = h_D + P_{res} = h_D + h_{MD} f_{res}(\lambda_M, H) \qquad (V.1)$$

where h_{MD} is the polarization of the muonium fraction at the moment of reaction. The factor f_{res} accounts for the spin dephasing during reaction, and is readily calculated [47]. Its field dependence is illustrated in figure V.1 for various reaction rates. An early study concluded that there was no variation of P_D in water with fields from 25 – 3200 G, so muonium reaction was discounted as a possible contributor to the missing fraction.

However, facilities for μSR have been greatly improved over the past 15 years, with reliable beam production, two orders of magnitude increase in beam intensity, the development of the surface muon beam and the advent of the transversely polarized muon beam. Under these new conditions a small but significant field-dependence of P_D in water came to light during a recent investigation of residual polarization in the reaction of muonium with hydrogen peroxide (a preliminary report is given in [23]). Accordingly, a project was initiated to reinvestigate muonium in water, and to extend studies to different temperatures and pressures.

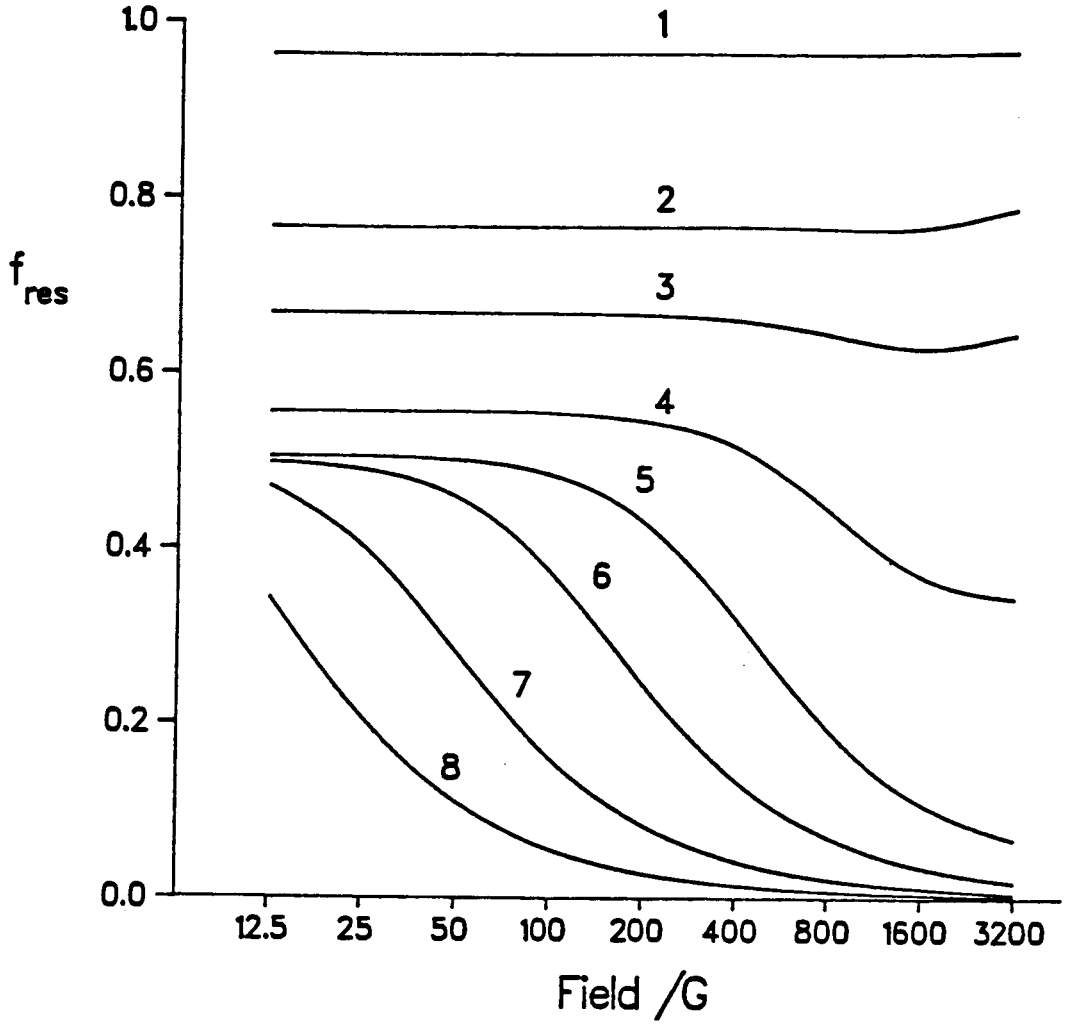

Figure V.1. Residual muon polarization in the diamagnetic products of a single-step muonium reaction as a function of magnetic field for reaction rates: (1) $1x10^{11}$ s^{-1}, (2) $3x10^{10}$ s^{-1}, (3) $2x10^{10}$ s^{-1}, (4) $1x10^{10}$ s^{-1}, (5) $3x10^{9}$ s^{-1}, (6) $1x10^{9}$ s^{-1}, (7) $3x10^{8}$ s^{-1}, and (8) $1x10^{8}$ s^{-1}.

V.2. Experimental

Experiments were performed at the M20 and M15 beam lines of TRIUMF, using conventional μSR techniques. The high pressure experiments employed longitudinally polarized backward muons (in M20A), whose high momentum is required to penetrate the window of the pressure cell. The magnetic field was applied transverse to the beam and was limited to 800 G to avoid significant beam deviation. Details of the experimental setup were given earlier (Section IV.3).

The high-pressure cell and fittings are made of a beryllium-copper alloy, heat-treated for maximum strength after machining. A schematic representation is given in figure V.2. The cell is pressurized with a 7 kbar hydraulic hand pump charged with paraffin oil and connected via standard non-magnetic stainless-steel high-pressure tubing. A floating piston communicates the applied pressure to the liquid sample. The muon window is 2.5 mm thick and 12 mm in diameter. The whole apparatus has been tested up to 4 kbar, but the μSR experiments were limited to 2 kbar for safety reasons. The samples were bubbled with N_2 and transferred to the pressure cell in a N_2 atmosphere before the cell was sealed.

Experiments at atmospheric pressure utilized either the M15 or the M20B surface muon beam in transverse polarization mode. The magnetic field was applied along the direction of the incoming beam to minimize field-dependent systematic errors associated with beam-bending. Experiments covered the range of 0 – 3200 G. Details of the sample cell, sample handling technique and thermostatic control were as described in Section IV.7.

For residual polarization experiments, typically 2–3 million events were collected in each of the μSR histograms corresponding to the four positron

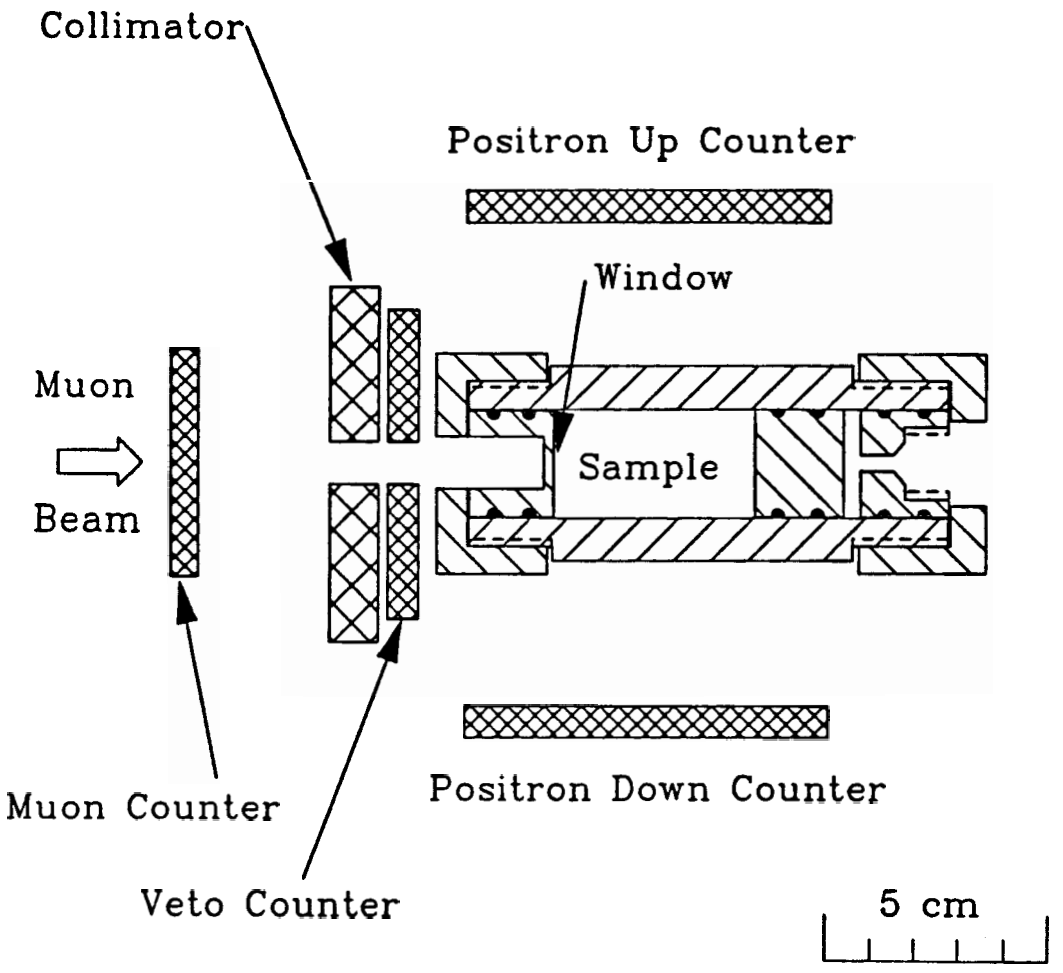

Figure V.2. Schematic representation of the high-pressure cell and scintillator arrangement.

telescopes (two for the high pressure apparatus) symmetrically placed about the sample. Higher statistics, usually 8–10 million events per histogram, were used for muonium signals, which were studied at 10 G.

V.3. Data analysis

Signal amplitudes were extracted from the raw histograms by computer fitting of the appropriate theoretical function as given in Chapter II. For concentrated $MnCl_2$ solutions, the μSR spectra contained two signals at the diamagnetic precession frequency – a long-lived signal and another which decays rapidly. Thus, adequate fits were only possible by assuming two diamagnetic fractions with different (exponential) relaxation rates [48]:

$$A(t) = [A_{D1} \exp(-\lambda_{D1}t) + A_{D2} \exp(-\lambda_{D2}t)] \cos(\omega_D t + \phi) \qquad (V.2).$$

where A_{D1} and A_{D2} represent the asymmetries of the two signals with exponential decay rates of λ_{D1} and λ_{D2}, respectively.

V.4. Calibration procedure

The diamagnetic and muonium signal amplitudes were converted to muon polarization fractions P_D and P_M by calibration against the diamagnetic signal of a standard sample run under identical conditions. It has been common practice to use carbon tetrachloride as a liquid standard, assuming a diamagnetic fraction of 1.00. However, a small field dependence of P_D for CCl_4 has been reported by Miyake *et al* [49]. The present measurements consistently gave a slightly higher signal amplitude for aluminium, another widely used standard, so all the measurements have been calibrated against that. The aluminium standards used were constructed

from commercial grade foil made up to have the same shape and weight as the liquid samples. Figure V.3 shows muon asymmetries determined for the surface muon apparatus in two separate run periods. The solid lines represent smoothed curves through the two sets of aluminium data, and were used in the calibration of the other samples. At high fields the CCl_4 data fall significantly below the dotted curve, which represents the calibration data scaled by a constant factor. Residual polarization analysis according to equation (V.1) is consistent with a prompt diamagnetic fraction of 0.963 ± 0.002 and a muonium fraction of 0.037 ± 0.006, which reacts to give diamagnetic products at a rate constant $\lambda = (7 \pm 1) \times 10^9\ s^{-1}$.

The polarization of the different muonic species was obtained as follows [50]:

$$P_D = A_D/A_S \qquad (V.3)$$

and

$$P_M = 2\,A_M/A_S \qquad (V.4)$$

where A_S is the asymmetry of the standard (Al). The factor of 2 in P_M accounts for the unobserved fraction of muonium in the singlet state. An average value of A_S was used for results obtained from the first run period where P_D in aluminium did not show any field dependence. For the second run period, P_D in aluminium exhibited a slight field dependence (see figure V.3). Subsequently, the smoothed curve (from a fitted polynomial function) was used for calibration.

In the high pressure experiments approximately 10% of the incoming muons were found to stop in the window and walls of the cell, as indicated by the presence of a non-relaxing signal component detected when the cell was filled with 50% manganous nitrate [51]. This is illustrated in figure V.4, which compares the muon

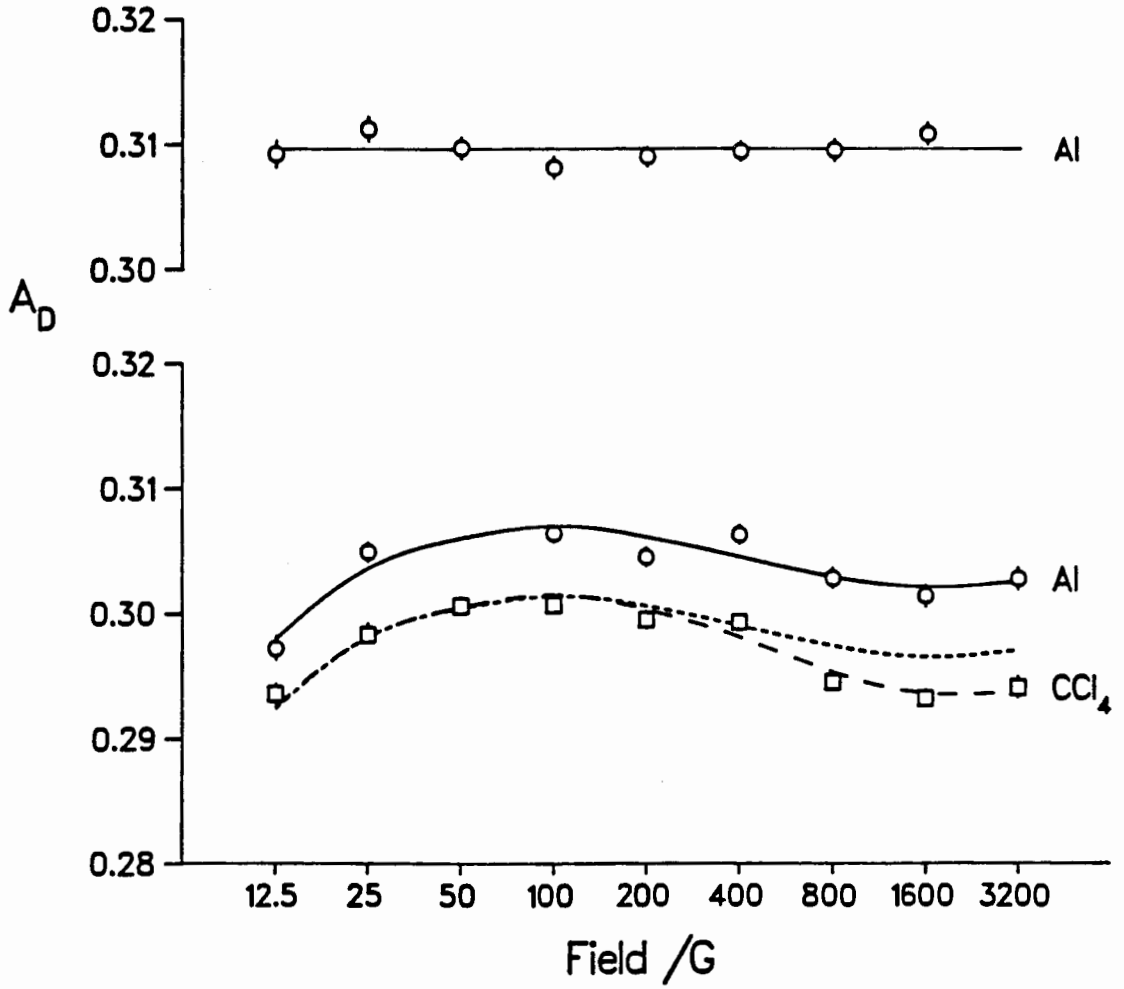

Figure V.3. Muon asymmetry as a function of applied magnetic field in Al (o) and CCl_4 (□). Note the break in the *y*-axis, which separates the data obtained in different run periods.

asymmetry for a sample of 50% manganous nitrate solution in the high-pressure cell with the same sample in a conventional thin-walled cell. The fast-decaying signal is due to muon spin relaxation by the paramagnetic manganous ion. The low-amplitude non-relaxing component seen in the upper curve arises from muons stopped in the non-magnetic material of the cell. The polarizations were corrected according to established procedures [18,19]:

$$P_D = (A_D - A_W)/(A_S - A_W) \qquad (V.5)$$

and

$$P_M = 2\,A_M/(A_S - A_W) \qquad (V.6)$$

where A_W is the wall asymmetry and was determined from the non-relaxing signal for 50% manganous nitrate.

In one run period no aluminium standard was measured in the pressure cell, and the calibration against CCl4 was inconsistent with all the other data, so the results for water were simply scaled to fit the other more accurately calibrated data.

A weighted average polarization was calculated by combining the results for individual histograms:

$$\langle P \rangle = \sum_i (P_i/\Delta P_i^2) \,/\, \sum_i (1/\Delta P_i^2) \qquad (V.7)$$

where ΔP_i is the error of the polarization of the *i-th* histogram.

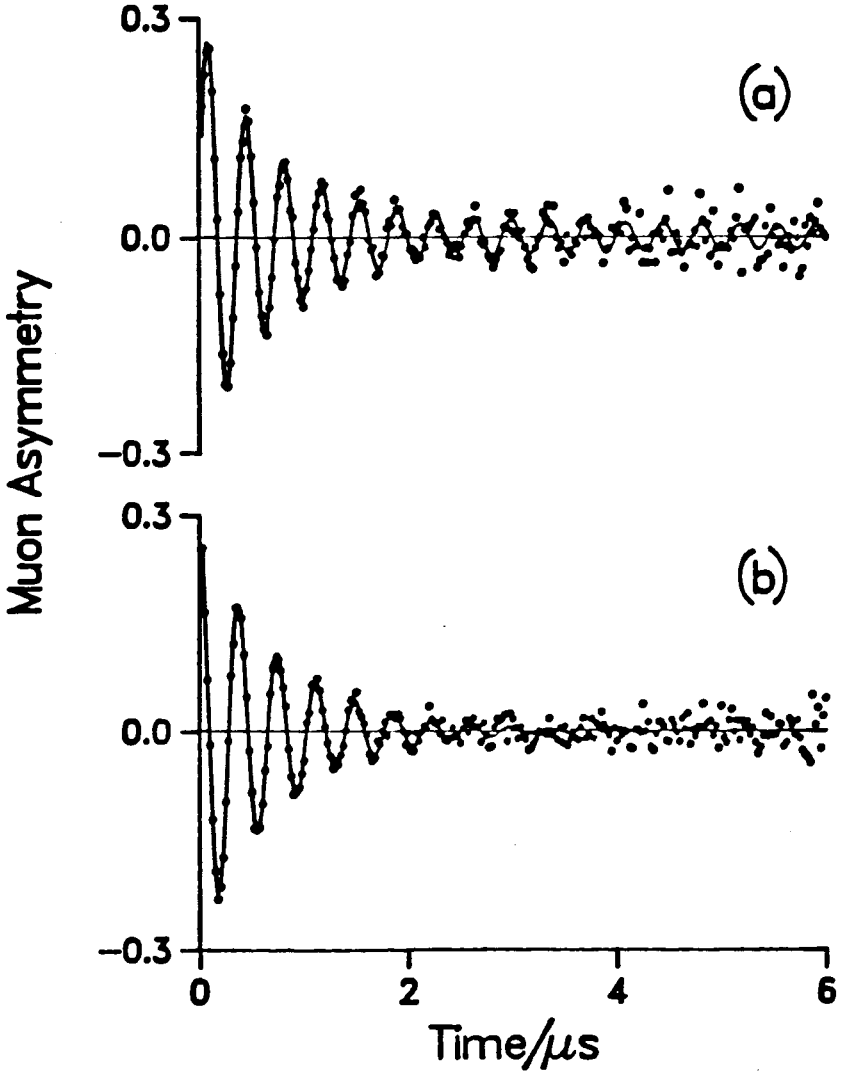

Figure V.4. Muon asymmetry for a sample of 50% manganous nitrate solution in (a) the high-pressure cell, compared with (b) a conventional thin-walled cell, under an applied field of 200G.

V.5. Experimental results

V.5.1. The diamagnetic muon fraction in water

The diamagnetic fraction (P_D) in water was determined for 9 values of the applied magnetic field from 12 G to 3200 G, at temperatures of 276 K, 298 K, and 323 K (fig. V.5). A field dependence is apparent at all three temperatures, so the data were subjected to residual polarization analysis, assuming direct reaction of Mu to form a diamagnetic product as described by eq. (V.1). Initially, separate three-parameter (h_D, h_{MD}, and λ_M) fits were carried out for each temperature. The results are reported in table V.1. The optimized value of λ_M at 276 K is inconsistent with that obtained for the higher temperature data sets, but a fit with fixed λ_M also described the data well, as can be seen in figure V.5. P_D was also determined as a function of pressure for applied fields of 50 G, 200 G and 800 G. The data were analyzed as above, but because of the limited number of field points λ_M was fixed at the value obtained in the earlier study. The experimental data are plotted in figure V.6, and the fit results are included in table V.1.

V.5.2. The muonium fraction in water

In order to characterize the missing fraction, muonium fractions (P_M) were determined over the same range of temperature and pressure as the residual polarization studies. P_M seems to fall slightly with increasing pressure (figure V.7), but the variation with temperature (figure V.8) is too slight to be significant. In both cases the variation of the initial muonium fraction, $h_M = 1 - h_D$ is more marked. The observable Mu fraction is less than half of h_M, and only part of the difference is due to h_{MD}, muonium which reacts to give the residual diamagnetic

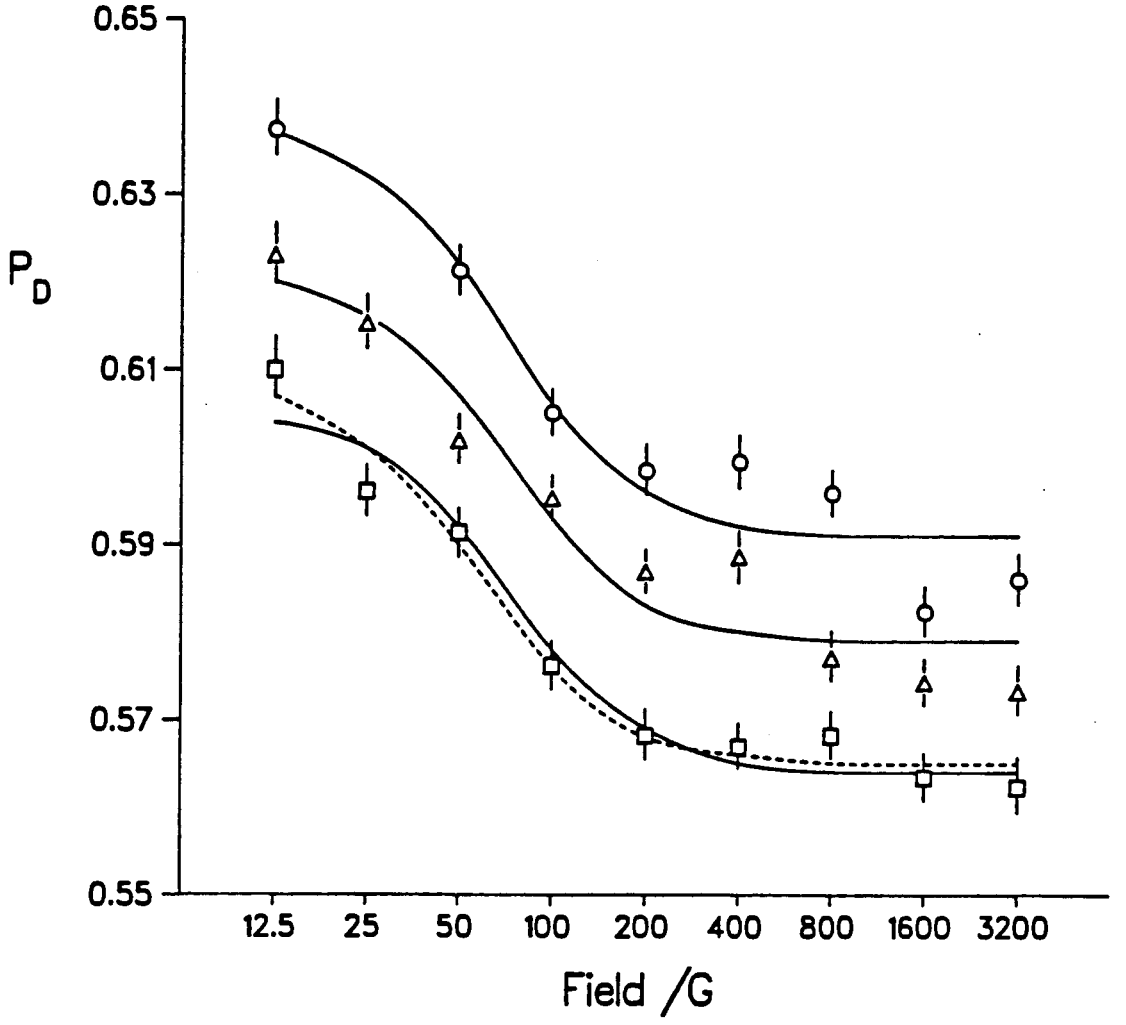

Figure V.5. Muon polarization as a function of magnetic field for pure water at 323 (o), 298 (Δ), and 276 K (□). The lines through the experimental points represent the fits summarized in table V.1. The dotted line represents the fit to the 276 K data with available λ_M.

Table V.1. Residual polarization analysis of the field dependence of P_D for pure water

T (K)	h_D	h_{MD}	log λ_M
323	0.590(1)	0.095(4)	8.80(4)
298	0.578(2)	0.085(6)	8.80(5)
276	0.565(1)	0.087(4)	8.69(5)
276	0.564(2)	0.083(5)	8.80[a)]
p (bar)	h_D	h_{MD}	log λ_M
2000	0.631(4)	0.058(16)	8.80[a)]
1000	0.605(4)	0.059(17)	8.80[a)]
1	0.573(4)	0.071(17)	8.80[a)]

[a)] Parameter value fixed.

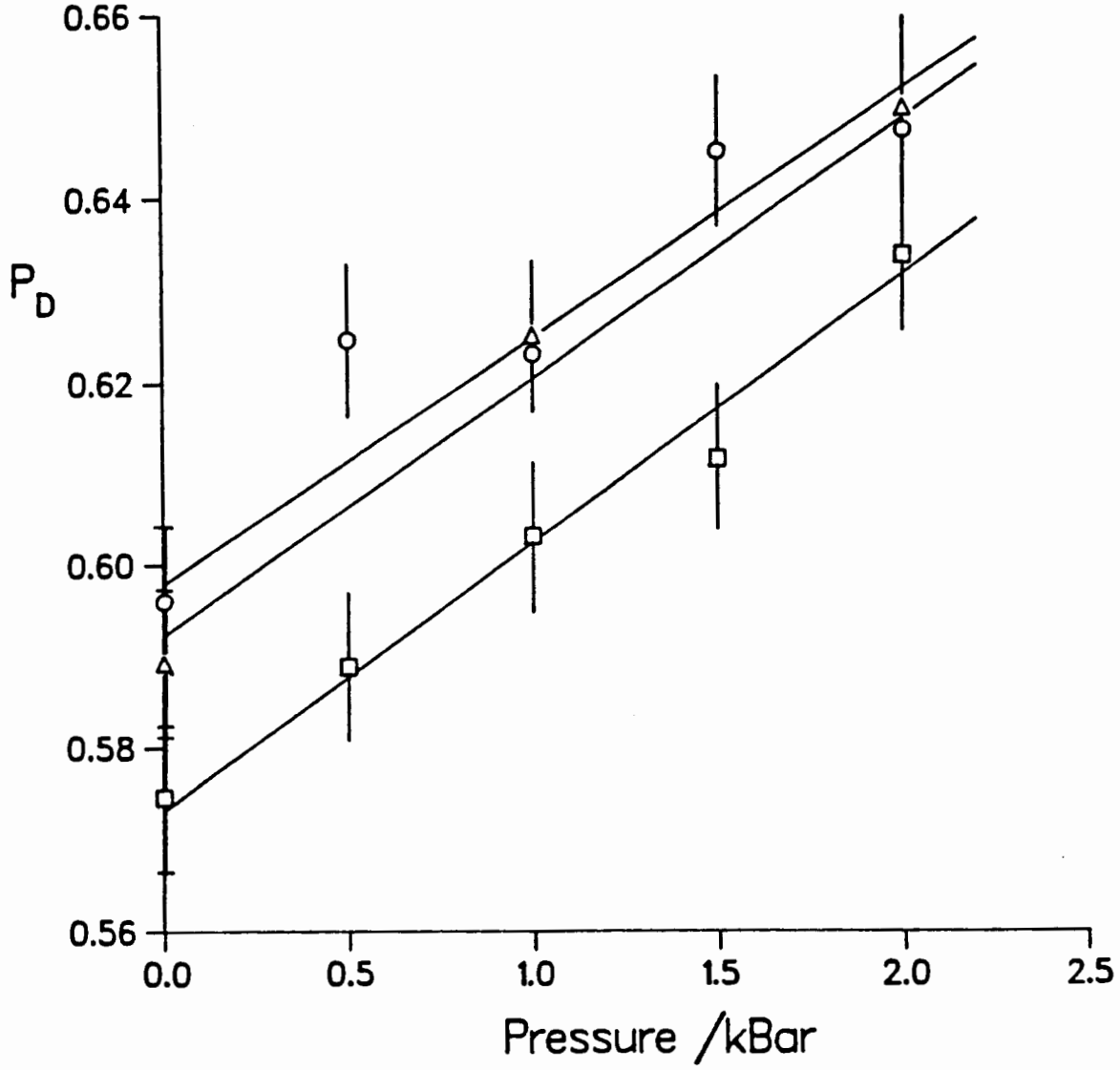

Figure V.6. Muon polarization in water as a function of pressures in applied fields of 50 (o), 200 (Δ), and 800 G (□).

polarization. Thus, there is still a "lost" fraction, $h_L = 1 - h_D - h_{MD} - P_M$. The ratios of P_M, h_{MD} and h_L to h_M are listed in table V.2. There is little variation with temperature and pressure.

V.5.3. Aqueous solutions

Residual polarization studies of the type described in Section V.5.1 were carried out for several aqueous solutions: 0.004, 0.04 and 0.4 M $MnCl_2$ to test the effect of various concentrations of a paramagnetic ion; and 0.8 M NaCl as a control in case Cl^- had an effect. The results were analyzed as for the pure water, except for 0.4 M $MnCl_2$, where there is no significant field dependence. The experimental data and fits are shown in figure V.9., and the best fit parameters are reported in table V.3. A series of measurements using 5 M KSCN was interrupted by technical problems, and a full set of field points was not achieved in the available beam time. Although the data are insufficient for quantitative residual polarization analysis, all P_D measurements were below those in pure water. From the high and low field extremes, estimates of 0.50 and 0.09 for h_D and h_{MD}, were deduced respectively.

Diamagnetic signals were also investigated for a highly concentrated solution of $MnCl_2$, corresponding to $MnCl_2 \cdot 10H_2O$, and for a similar solution containing an additional 0.2M $NaNO_3$. Two distinct diamagnetic components of different relaxation rate were detected for both samples. The amplitudes were found to be field-independent and correspond to polarization fractions $P_D(fast) = 0.556$ and $P_D(slow) = 0.067$ in the absence of nitrate, and $P_D(fast) = 0.641$, $P_D(slow) = 0.039$ with the additional 0.2 M $NaNO_3$. The two components collapsed to one on addition of concentrated nitric acid, as can be seen in figure V.10, which also contains an example of the long-lived signal detected in pure water.

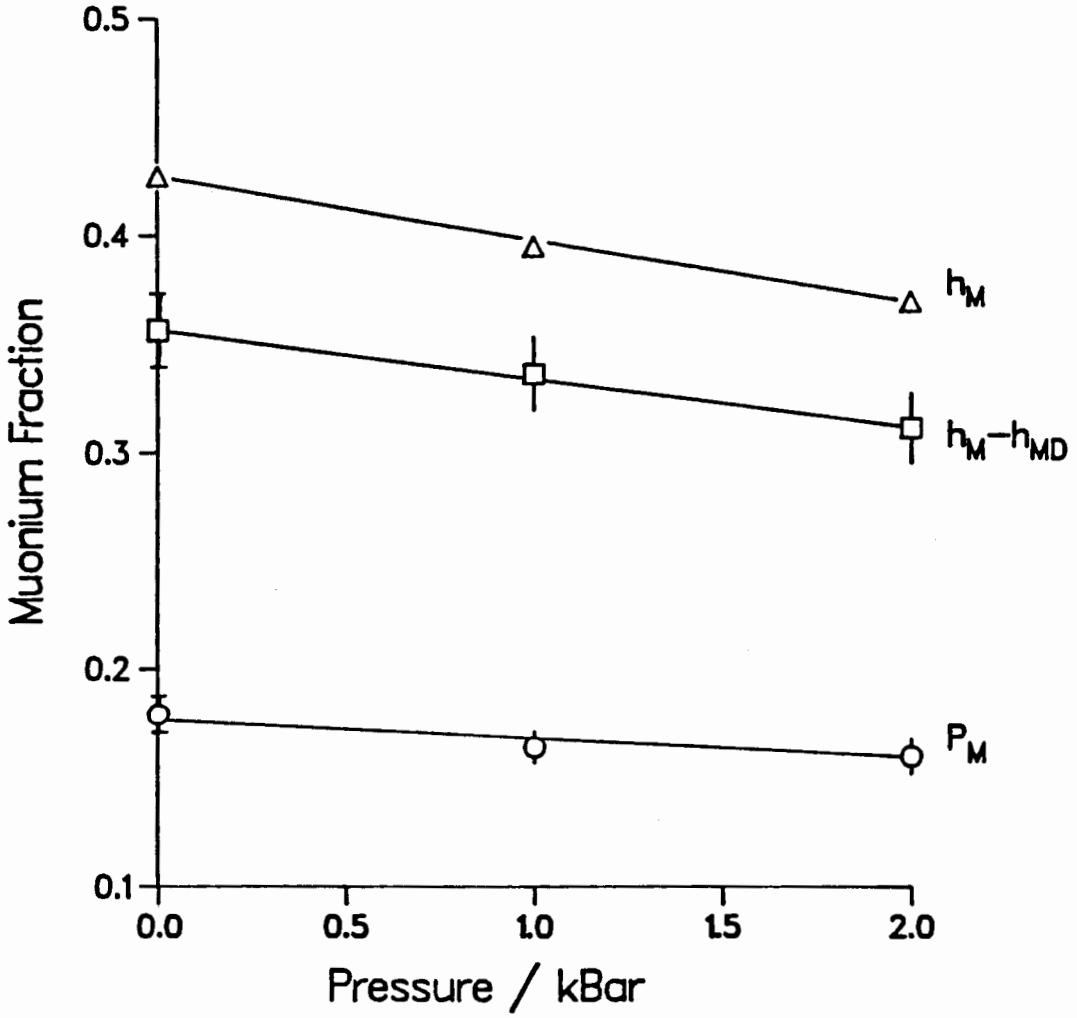

Figure V.7. Muonium fractions in water as a function of pressure: P_M (o), h_M (Δ), and h_M-h_{MD} (□).

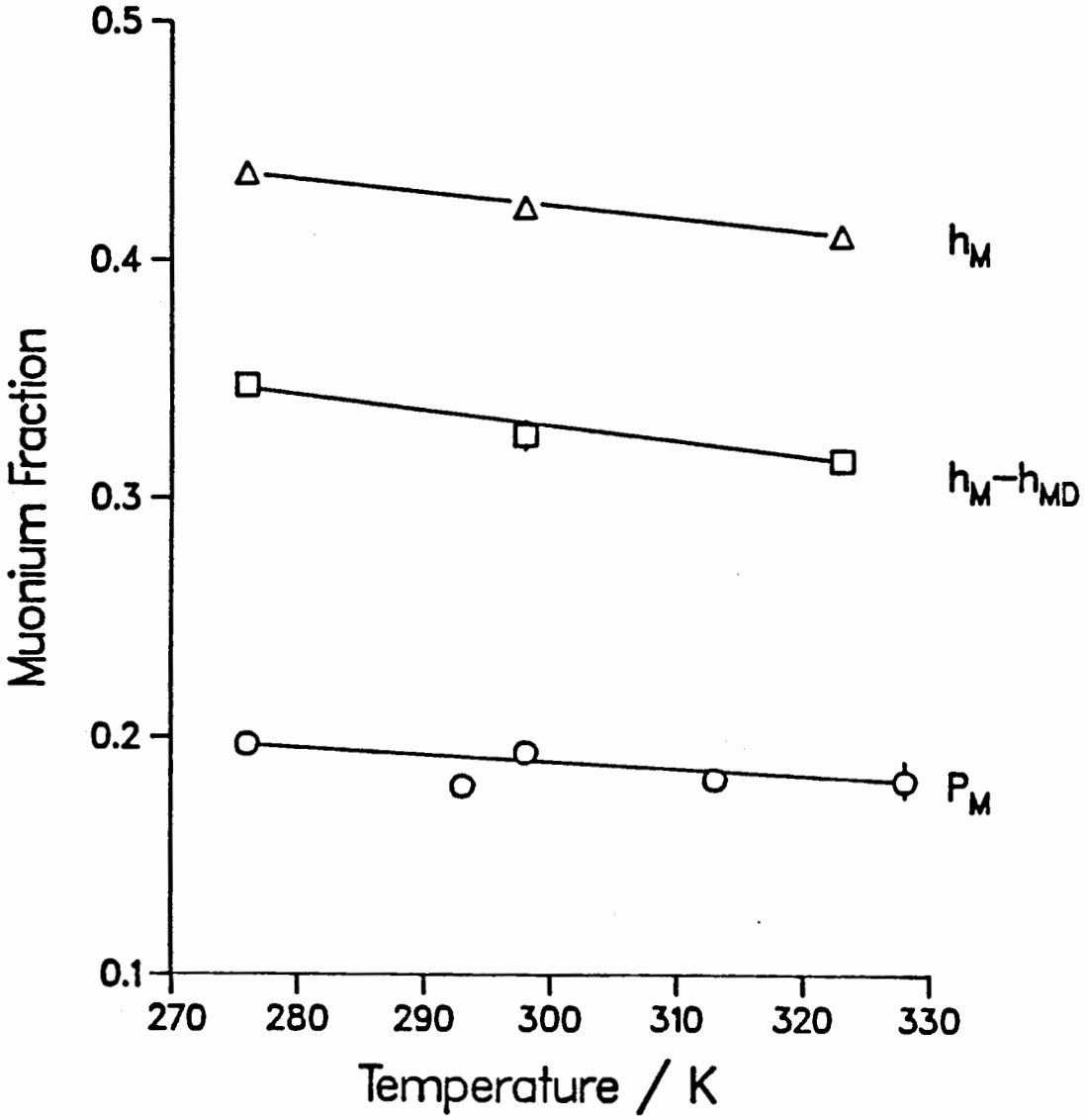

Figure V.8. Muonium polarization in water as a function of temperature: P_M (o), h_M (Δ), and $h_M - h_{MD}$ (□).

Table V.2. Magnitudes and ratios of the muonium fractions in water

T/K	P_M	h_M [a]	P_M/h_M	h_{MD}/h_M	h_L/h_M [b]
323	0.181(8) [c]	0.410(1)	0.44(2)	0.23(1)	0.33(2)
298	0.193(4)	0.422(2)	0.46(1)	0.20(1)	0.34(1)
276	0.197(4)	0.435(1)	0.45(1)	0.20(1)	0.35(1)
276	0.197(4)	0.436(2) [d]	0.45(1)	0.19(1) [d]	0.36(1)
p/bar	P_M	h_M [a]	P_M/h_M	h_{MD}/h_M	h_L/h_M [b]
2000	0.167(9)	0.369(4)	0.45(2)	0.16(4)	0.39(5)
1000	0.172(8)	0.395(4)	0.44(2)	0.15(4)	0.42(5)
1	0.187(9)	0.427(4)	0.44(2)	0.17(4)	0.40(4)

[a] $h_M = 1 - h_D$.
[b] $h_L = 1 - h_D - h_{MD} - P_M$.
[c] P_M measured at 328 K.
[d] log λ_M fixed at 8.80.

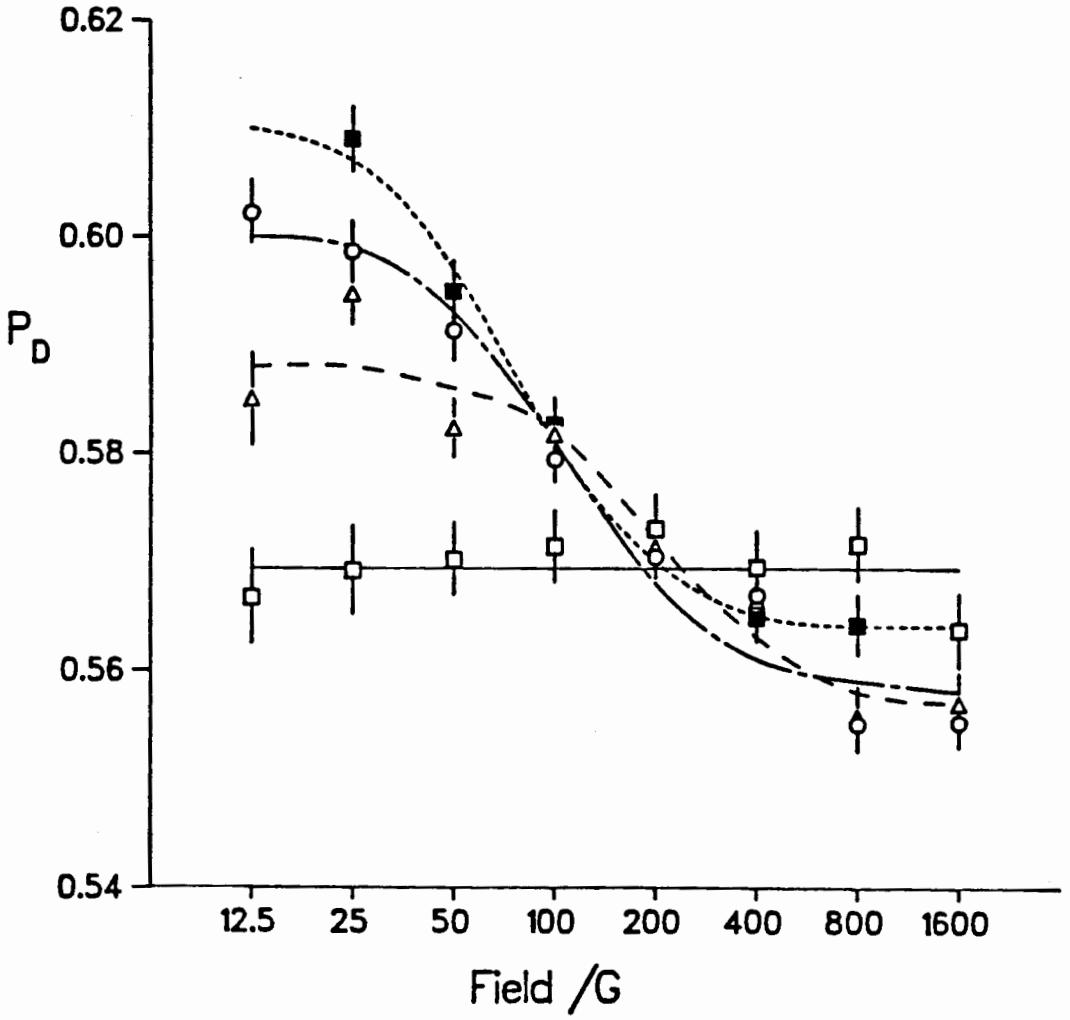

Figure V.9. Muon polarization as a function of magnetic field for $MnCl_2$ solutions, 0.004 (o), 0.04 (Δ), and 0.4 M (□); and 0.8 M NaCl (■).

Table V.3. Residual polarization analysis of P_D for some aqueous solutions

Solution	h_D	h_{MD}	log λ_M
0.004 M $MnCl_2$	0.557(1)	0.087(1)	8.98(5)
0.04 M $MnCl_2$	0.555(1)	0.066(3)	9.26(5)
0.4 M $MnCl_2$	0.569(1)	[a]	
0.8 M NaCl	0.563(2)	0.098(5)	8.82(4)

[a] No field dependence.

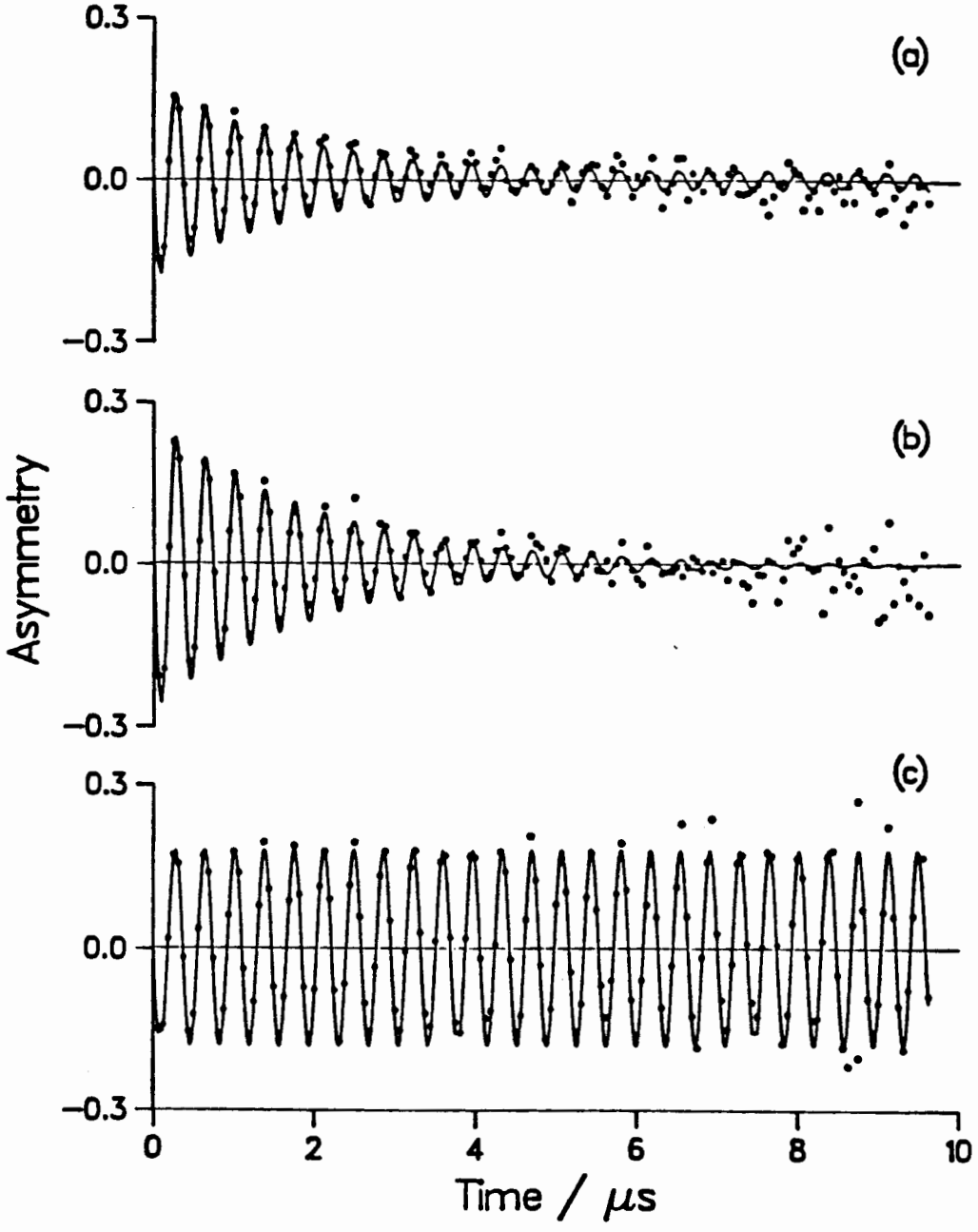

Figure V.10. Muon precession signals in: (a) $MnCl_2 \cdot 10H_2O$, (b) $MnCl_2 \cdot 10H_2O$ + a large excess of nitric acid, and (c) pure water.

V.6. Discussion

V.6.1. The origin of the field dependence of P_D in pure water

The greater part of P_D is independent of field, and is still interpreted as the prompt muon fraction, h_D, i.e. those muons which escape muonium formation via hydration, and end up as MuOH. The additional field-dependent fraction is attributed to a more slowly formed diamagnetic species, and the field dependence analysis is consistent with reaction of muonium at a first-order rate constant of about 6×10^8 s^{-1}. Since some muonium (P_M) is detected at much later times (microseconds), it follows that, of the original muonium fraction ($h_M = 1 - h_D$), only part (h_{MD}) reacts. Furthermore, since $P_M + h_{MD} < h_M$ there must be yet a third fate for muonium, one in which the muon polarization is lost. The latter fate is the missing fraction discussed in the past and attributed to spin depolarization of muonium. Although reaction and depolarization of muonium are in competition with each other, part of the muonium fraction escapes both fates, so there must be some spatial or temporal boundary which limits the loss of the muonium signal. Both possibilities are consistent with radiolysis effects – the paramagnetic products of water radiolysis are short-lived and are distributed in a non-homogeneous manner, so some muonium atoms may never react.

There is strong evidence from residual polarization studies of dilute nitrate solutions that the radiolysis transient involved in the missing fraction is the hydrated electron [44]. Previously, only non-reactive spin-exchange encounters were considered, but since hydrogen atoms are known to react with e^-_{aq} [52],

$$H\cdot + e^-_{aq} \rightarrow H_2 + OH^- \qquad (V.8)$$

the analogous reaction for muonium should also be expected:

$$Mu + e^-_{aq} \rightarrow MuH + OH^- \qquad (V.9).$$

However, earlier results from longitudinal field experiments indicated that the missing fraction arises from spin relaxation rather than chemical reaction of Mu [43]. The results of other experiments supported this view [53,54]. In fact, both fates of muonium should be possible, since the outcome of Mu...e^-_{aq} encounters depends on the electron spin multiplicity of the radical pair. Only singlet pairs react chemically, since a chemical bond must be formed. Triplet pairs are subject to spin interaction (spin exchange), which in some cases results in loss of muon polarization.

In summary, the fraction (h_{MD}) which gives rise to the field dependence of P_D is attributed to singlet encounters between Mu and e^-_{aq}. The amended model for the distribution of muon polarization in water is depicted in Scheme V.1.

V.6.2. The identity of the diamagnetic muon species in water

Determination of the identity of the diamagnetic reaction product would be most valuable to test the explanation of the residual polarization. There is no doubt that the prompt fraction is due to MuOH (or one of its hydrated ions). Large concentrations of manganous nitrate result in efficient relaxation of the diamagnetic signal, and the measured relaxation rates for a variety of conditions are entirely in accord with a model in which MuOH enters the primary hydration sphere of the paramagnetic ion, resulting in efficient spin relaxation of the muon through both scalar and dipolar interactions [55,56]. Any reaction of Mu with OH, produced by the radiolysis of water, would also result in MuOH, whereas reaction with e^-_{aq} would give the quite different product, MuH. In principle, MuH and MuOH could be

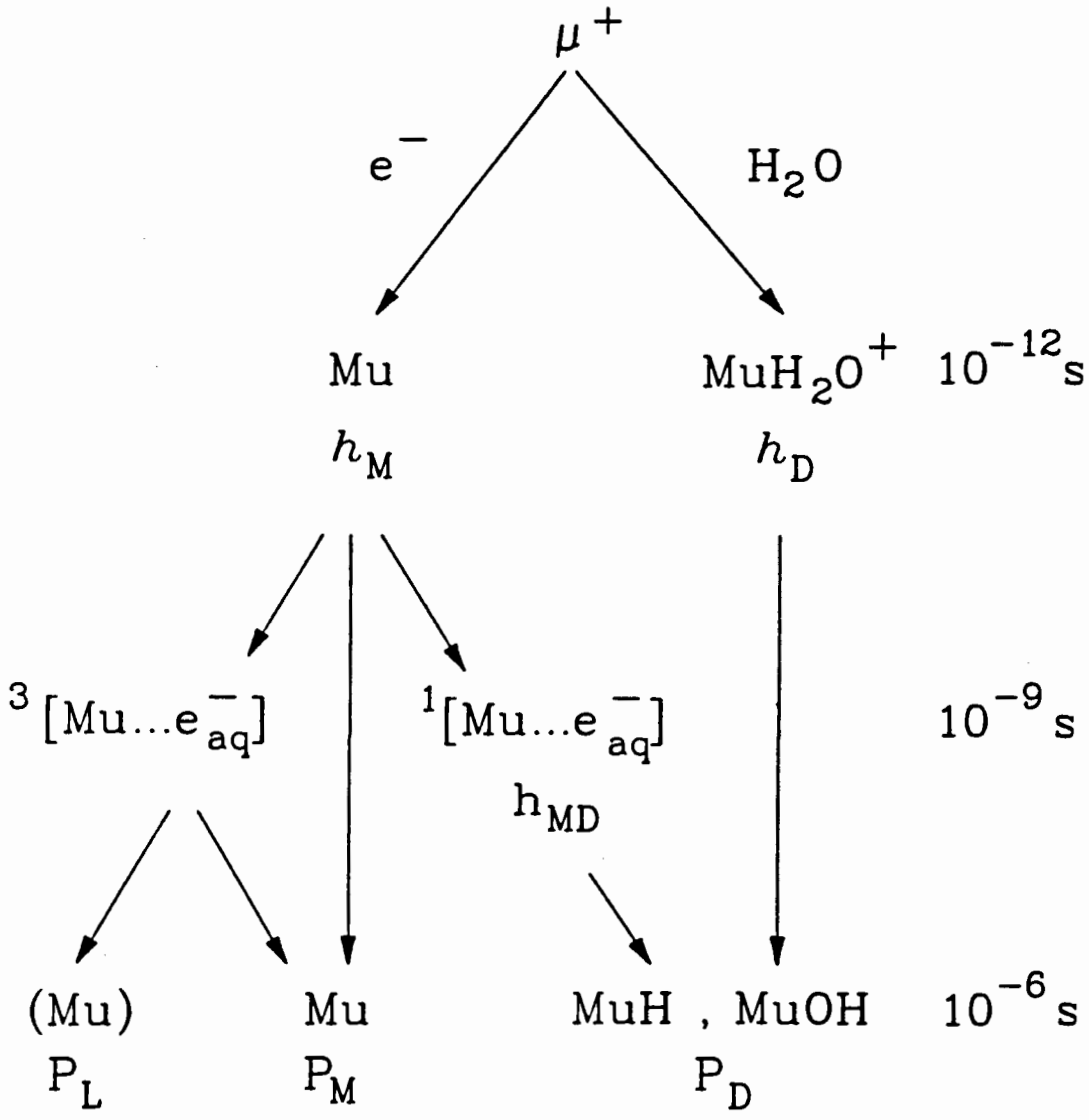

Scheme V.1. Refined spur model.

distinguished by their chemical shifts. Unfortunately, conventional μSR lacks resolution, although the recent developments of stroboscopic [57] and resonance [54,58] techniques have the potential to solve this problem.

Although not as specific as frequency, relaxation rates can also be used to distinguish diamagnetic species, as has been demonstrated for organic solvents [48]. Of the two distinct components apparent in the diamagnetic spectrum of $MnCl_2 \cdot 10H_2O$ (fig. V.10), the fast-decaying signal is readily attributed to MuOH (and associated ionic forms such as MuO^-), while the only possibility for the long-lived signal is MuH, all other species being of a protic nature in fast equilibrium with MuOH. The reduction of the long-lived signal by addition of nitrate is consistent with both inhibition of muonium [16] and scavenging of e^-_{aq}.

Thus, there is clear evidence of MuH formation in an aqueous solution. It is very tempting to attribute this MuH to the Mu + e^-_{aq} reaction, particularly since the muon fraction evident as the long-lived signal in $MnCl2 \cdot 10H_2O$ is equal to the fraction h_{MD} deduced from the residual polarization analysis of the pure water results. However, muonium should be efficiently depolarized in the presence of such a high concentration of paramagnetic ions, so that the product of its reactions would not be detected by transverse field μSR. (This point is expanded in the following Section.) It seems, therefore, that the MuH detected in concentrated $MnCl_2$ solution is not the same MuH as is responsible for the field dependence in pure water. Instead, it must be formed in a very short time (picoseconds) after muon thermalization, before there is significant diffusion of species from the terminal spur. As yet there are not sufficient data to do more than speculate on the process by which it is formed, but this question is worthy of further study, since it may shed light on the origin of the primary H_2 found in the conventional radiolysis of water.

It should be noted that a recent CIDNP study provides evidence that at least some of this H_2 arises from the intraspur reaction of H and e^-_{aq} [59].

V.6.3. The time-scale of "slow" MuH formation

The residual polarization study on pure water (table V.1) suggests that MuH is formed from Mu at a rate constant of 6×10^8 s^{-1}. This is consistent with the conclusion from scavenger studies that Mu interacts with e^-_{aq} on a nanosecond time-scale [44]. We suggest that there are three competitive pathways for muonium which encounters e^-_{aq}, as shown in Scheme V.1: (a) reaction to give MuH; (b) spin depolarization resulting in the missing fraction; and (c) survival to the microsecond timescale, where it can be detected by μSR. In addition, any Mu which escapes encounter with e^-_{aq} will also contribute to the detectable fraction P_M. The residual polarization studies on various concentrations of $MnCl_2$ were designed to test this competition and confirm the time-scale. Mu should be depolarized by the Mn^{2+} ions at a diffusion-controlled rate (a typical rate constant for other paramagnetic ions is 2×10^{10} M^{-1} s^{-1}). $MnCl_2$ concentrations were chosen to bracket the region where depolarization of muonium by Mn^{2+} is in direct competition with reaction or depolarization by e^-_{aq}.

The field dependence of P_D is quite different for the three solutions, as seen in fig. V.9. P_D is constant for 0.4 M $MnCl_2$, consistent with complete loss of muon polarization in Mu before encounter with e^-_{aq}. At the other extreme, the field dependence for 0.004 M $MnCl_2$ is similar in shape and extent to pure water, indicating that the reaction with e^-_{aq} occurs faster than spin relaxation by Mn^{2+}. For the 0.04 M $MnCl_2$ solution the field dependence is intermediate, with part of the muonium fraction depolarized before reaction. This is evident from the reduced

value of h_{MD} extracted from the residual polarization analysis (table V.3). At this concentration of Mn^{2+} the Mu depolarization rate is $\approx 8 \times 10^8\ s^{-1}$. The reaction rate of Mu with e^-_{aq} must be a little faster, since h_{MD} is more than half its pure water value.

Another indication of the reaction time-scale is provided by the shape of the field dependence curve, which is determined by the parameter λ_M. According to the theory of residual polarization [47] this is the total muonium reaction rate, *i.e.*

$$\lambda_M = \lambda_e + k_s [S] \qquad (V.10)$$

where λ_e is the rate constant of the reaction with e^-_{aq} and k_s is the rate constant for reaction with some other species S. Given that the second term in equation (V.10) amounts to $\approx 8 \times 10^8\ s^{-1}$ for 0.04M Mn^{2+}, and $\lambda_M = 1.8 \times 10^9\ s^{-1}$, we again deduce that $\lambda_e \approx 1 \times 10^9\ s^{-1}$.

A more precise statement of the Mu + e^-_{aq} rate is not possible at this stage (even with improved data), because the estimations are based on the usual assumption of homogeneous reaction kinetics. This assumption is correct for the reaction of Mu (an isolated atom) with the solute S (homogeneously distributed), but the reaction with e^-_{aq} depends crucially on the initial distribution of radiolysis products and the diffusion processes which bring Mu and e^-_{aq} together.

V.6.4. Reinterpretation of earlier residual polarization studies

In all previous residual polarization studies it was assumed that the muonium decay rate λ_M is directly proportional to reactant concentration [S]. Consideration of equation V.10 shows that this is only true for $k_s[S] >> \lambda_e$, and it is predicted that λ_M should appear anomalously high at low concentrations of S if reaction with e^-_{aq}

is ignored. Reexamination of old data [7,16,23,43,44] shows just such effects, and two examples are presented here.

In a study of residual polarization in sodium thiosulphate solutions [7] the values extracted for the muonium rate constant at the two lowest concentrations (8 x 10^{10} M^{-1} s^{-1} and 6 x 10^{10} M^{-1} s^{-1}) are far in excess of the values determined more directly by muonium decay measurements (1.5 x 10^{10} M^{-1} s^{-1}). However, if the muonium rates (N.B. rates, not rate constants, which were reported in ref. [7]) are plotted against thiosulphate concentration, a good straight line is achieved (fig. V.11), as predicted by eq. (V.10). The slope yields a value for the rate constant of (1.8 ± 0.5) x 10^{10} M^{-1} s^{-1}, in agreement with the muonium decay measurements made in solutions one-hundred-fold less concentrated. The intercept represents λ_e and has the value (5 ± 3) x 10^8 s^{-1}, in reasonable agreement with our other estimates for the timescale of Mu...e^-_{aq} encounters.

Similarly, a residual polarization study of acidic nitrate solutions [44] produced higher values for muonium decay rates than were found in an earlier study of neutral solutions [16]. For example, λ_M = 2.6 x 10^9 s^{-1} in 0.5 M nitrate in a large excess of acid, 1.4 x 10^9 s^{-1} when neutral. The e^-_{aq} lifetime in 0.5 M NO_3^- is only 0.1 ns, so λ_e is reduced to zero. That is why λ_M was found to be consistent with the rate constant determined from muonium decay measurements. In contrast, in acidic solutions e^-_{aq} is converted to H, which reacts much slower with NO_3^-, and Mu...H radical pairs can form and either react or undergo spin exchange in exactly the same way as Mu...e^-_{aq} pairs.

V.6.5. Competitive pathways of muon distribution

The distribution of positive muons amongst the various fractions identified by

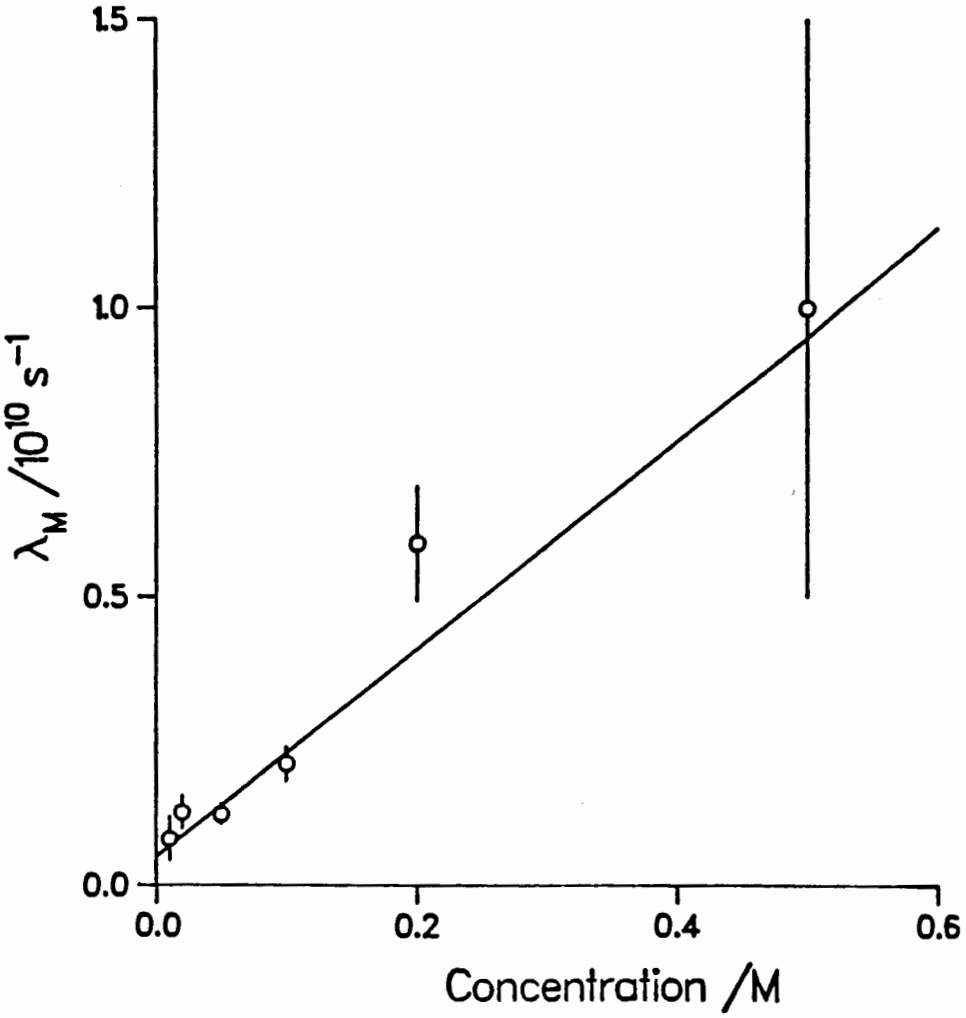

Figure V.11. Muonium decay rates determined from the residual polarization study of thiosulphate solutions [7].

μSR on the microsecond time-scale is a result of two distinct competitions which take place at different times after muon thermalization. Muonium formation competes with muon hydration, probably less than 1 ps after thermalization [16,60]. Some MuH may also be formed at this stage, as suggested in section V.6.2, but there is no indication which of μ^+ or Mu is its precursor. The second competition occurs around 1 ns after thermalization, when muonium encounters paramagnetic radiolysis products. Muonium may be depolarized, react to give MuH, or escape unchanged. The outcome of these competitions is manifest in the relative magnitudes of the various polarization fractions. The way in which these fractions vary with temperature, pressure and solute concentration provides clues as to the nature of the competitive reactions.

The increase of P_D with temperature was known long ago [61], and has been remeasured in more recent times [24]. This residual polarization study has confirmed that it is the prompt fraction h_D which changes, i.e. less muonium is formed at elevated temperatures. Similarly, less muonium is formed as the pressure is increased. However, table V.2 shows that, once formed, the fate of muonium is not significantly influenced by temperature or pressure. This is in accord with the concept of spin-selective reactions, *i.e.* the outcome of the competition is determined by spin statistics, which are not influenced by temperature and pressure. It is instructive to consider the predictions of a simple model.

Since the electron spins of Mu and e^-_{aq} are uncorrelated, ¼ of the encounter pairs should have an overall singlet electronic spin state and ¾ triplet. The singlet pairs should react to form MuH, whereas the triplets should experience a non-reactive spin interaction. Spin exchange in the M = 0 component of the triplet will result in muon depolarization [16], but the M = ±1 components will be

unaffected and muonium should escape with its polarization intact. Table V.2 shows that the fraction of muonium that reacts (h_{MD}/h_M) is only about 0.20. This can be taken as ¼ of the fraction of Mu which encounter e^-_{aq}. Thus, the encounter probability is 80%, and the simple model predicts $h_L/h_M = 0.20$ and $P_M/h_M = 0.6$. The experimental values (≈ 0.34 and ≈ 0.44) show an increase in the missing fraction at the expense of detectable muonium. This might be due to sequential encounters of Mu with e^-_{aq}. Another factor could be the mixing of singlet and triplet spin functions in the non-zero magnetic fields which apply in the experiment. A full quantitative description of these refinements is beyond the scope of the present work. However, it should be noted that much of the necessary theory has already been developed [62,63].

A few of the experimental findings pertain to the earlier competition, which includes muonium formation. The effects of temperature and pressure on h_D probably arise through changes in the rate of muon hydration rather than muonium formation. The local structure of water around the positive muon is bound to influence proton transfer from MuH_2O^+, and it is well known that the degree of hydrogen bonding in water is sensitive to changes in temperature and pressure [64]. Recent calculations by Brocklehurst and Cook [65] suggest that muons in water may exist as $MuH_4O_2^+ \cdot 4H_2O$ in contrast to $H_3O^+ \cdot 2H_2O$, and that H^+ transfer (resulting in MuOH) may be much slower than originally supposed.

It is possible that dissolved ions also affect the hydration rate through their influence on water structure. For the solutions of $MnCl_2$ and NaCl slightly lower values of h_D were found than for pure water (compare table V.3 with table V.1), and the value for the KSCN solution was even lower. In the latter case, the lowering of h_D was attributed to scavenging of the OH radical by SCN^- [66]. The

Cl^- ion is also known to react with OH [67]. Clearly, more experiments will be necessary to test whether the effect of dissolved ions on the structure of water can influence the distribution of muons between Mu and MuOH.

V.7. Conclusion

There is a small field dependence of the diamagnetic muon polarization in pure water. It arises from MuH formed in the spin-selective reaction of Mu with e^-_{aq}. In competition with chemical reaction is spin exchange, which leads to the muon spin depolarization manifest in the missing fraction. These processes occur on a nanosecond time-scale and are quite distinct from the competition between muon hydration and muonium formation which occur at much shorter times.

CHAPTER VI. MUON SPECTROSCOPIC TECHNIQUES II - μLCR

VI.1. The muon level-crossing resonance (μLCR) technique

The conventional time-differential transverse field μSR technique does not allow the determination of the hyperfine coupling constants (hfcc) of magnetic nuclei present in a radical other than that of the muon. In atomic spectroscopy and nuclear quadrupole resonance the mixing effect of near degenerate levels has been known for many years [68,69]. In 1984, Abragam proposed the use of this phenomenon to detect the hyperfine splittings of paramagnetic ions in longitudinal field μSR [12]. This led to the development of the μLCR technique [13,14,70,71]. The power of μLCR as a spectroscopic technique is slowly being realized. The information contained in a μLCR spectrum yields extra knowledge about non-muon spin interactions. A brief review of the theory is given below.

The spin Hamiltonian for a Mu-substituted free radical was given in equation II.13. For a three-spin system with an electron, a muon and one nucleus with spin I^k (assumed to be ½ in much of the following), there are eight energy levels. Due to the dominance of the electron Zeeman term in $\hat{H}$ the energy levels of the spin system are separated into two groups according to the sign of the electron spin (the energy gap of the electron Zeeman term is about 3 MHz per Gauss while the proton hyperfine energy gap is typically 2 or 3 orders less). The spin Hamiltonian equation has been solved approximately by Roduner *et al* [14]. The field of closest approach of the levels is given by [14]

$$B_0(M) \approx \left| \frac{A_\mu - A_k}{2(\gamma_\mu - \gamma_k)} - \frac{A_\mu^2 - 2MA_k^2}{2\gamma_e(A_\mu - A_k)} \right| \qquad \text{(VI.1)}$$

and the energy gap or μLCR transition frequency

$$\omega(M,B) = \pi \left[\left(2B(\gamma_\mu - \gamma_k) - |A_\mu - A_k| + \frac{A_\mu^2 - 2MA_k^2}{2B\gamma_e} \right)^2 + \left(\frac{cA_\mu A_k}{B\gamma_e} \right)^2 \right]^{1/2} \quad \text{(VI.2)}$$

and the minimum energy gap

$$\omega_0(M,B_0) \approx \frac{\pi c A_\mu A_k}{B_0 \gamma_e} \quad \text{(VI.3)}$$

where γ_i are the magnetogyric ratios, $I^k \geq M \geq (-I^k+1)$ and $c = [I^k(I_k+1) - M(M-1)]^{1/2}$. There are $2I^k$ nearly degenerate μLCR transitions. At the resonance field, the off-diagonal terms of the spin Hamiltonian are no longer negligible and they serve to mix the two states. This result is actually a non-crossing of the energy levels. It is also called the Avoided Level Crossing Resonance (ALCR) by researchers from PSI [14,71]. For $A_\mu > A_k$ only the states with $m^s = +1/2$ come to resonance, for $A_\mu < A_k$ only those with $m^s = -1/2$. For $A_\mu \approx A_k$, this treatment is invalid.

The muon expression for the muon polarization in the three-spin system at the high field limit is then given by [14]

$$P_z(B) = 1 - \frac{2}{N} \sum_{i=1}^{2I^k} \frac{\omega_{0i}^2}{\lambda^2 + \omega_{0i}^2 + [2\pi(B - B_{0i})(\gamma_\mu - \gamma_k)]^2}, \quad \text{(VI.4)}$$

which is a sum of Lorentzian lines with full width at half maximum (FWHM)

$$\Delta B_{1/2} = \frac{\omega_0}{\pi(\gamma_\mu - \gamma_k)} \left(1 + \frac{\lambda^2}{\omega_0^2} \right)^{1/2} \quad \text{(VI.5)}$$

and amplitude

$$P_z(B_0) = 1 - \frac{2}{N}\frac{\omega_0^2}{\lambda^2 + \omega_0^2} \qquad \text{(VI.6)},$$

where N is the dimension of the energy matrix and is equal to 8 for a three spin ½ system. The parameter λ is the damping rate of the transition, which describes any process that takes the muon out of the resonance, *i.e.* the muon decay and chemical reactions. In the presence of electron spin flip (T_1^e) processes, the situation becomes more complicated and requires a special treatment. The selection rule of a level-crossing resonance is $\Delta(m^s+\Delta m^k) = 0$ for an isotropic spin system. In solids, the averaging of the hyperfine interaction due to tumbling of the molecules is no longer present and the situation becomes different. In particular, the anisotropy of the hyperfine interaction gives rise to a zero-crossing resonance (ZCR) in addition to the regular μLCR resonances [72]. ZCR occurs at a field where one of the radical precession frequencies goes through zero. This effect has been observed for muonium addition to frozen isobutene [73].

In general, $\Delta B_{½} << B_0$. This implies that the μLCR dips are sharp resonances in the curve of $P_z(B)$. This can be seen in the calculated muon polarization curve for a μ^+-e^-−p system as shown in Figure VI.1, which also includes a schematic diagram of the energy levels of the system in the level-crossing region. This means that resonances due to inequivalent nuclei will usually not overlap and can be treated separately. This feature allows μLCR to be used to measure nuclear hyperfine parameters in complicated spin systems. The sharpness of a μLCR peak also allows the position of the resonance field to be determined precisely. In a μLCR experiment, the few gauss uncertainty in the value of B_0 are caused by uncertainties in field calibration and is equivalent to only a few

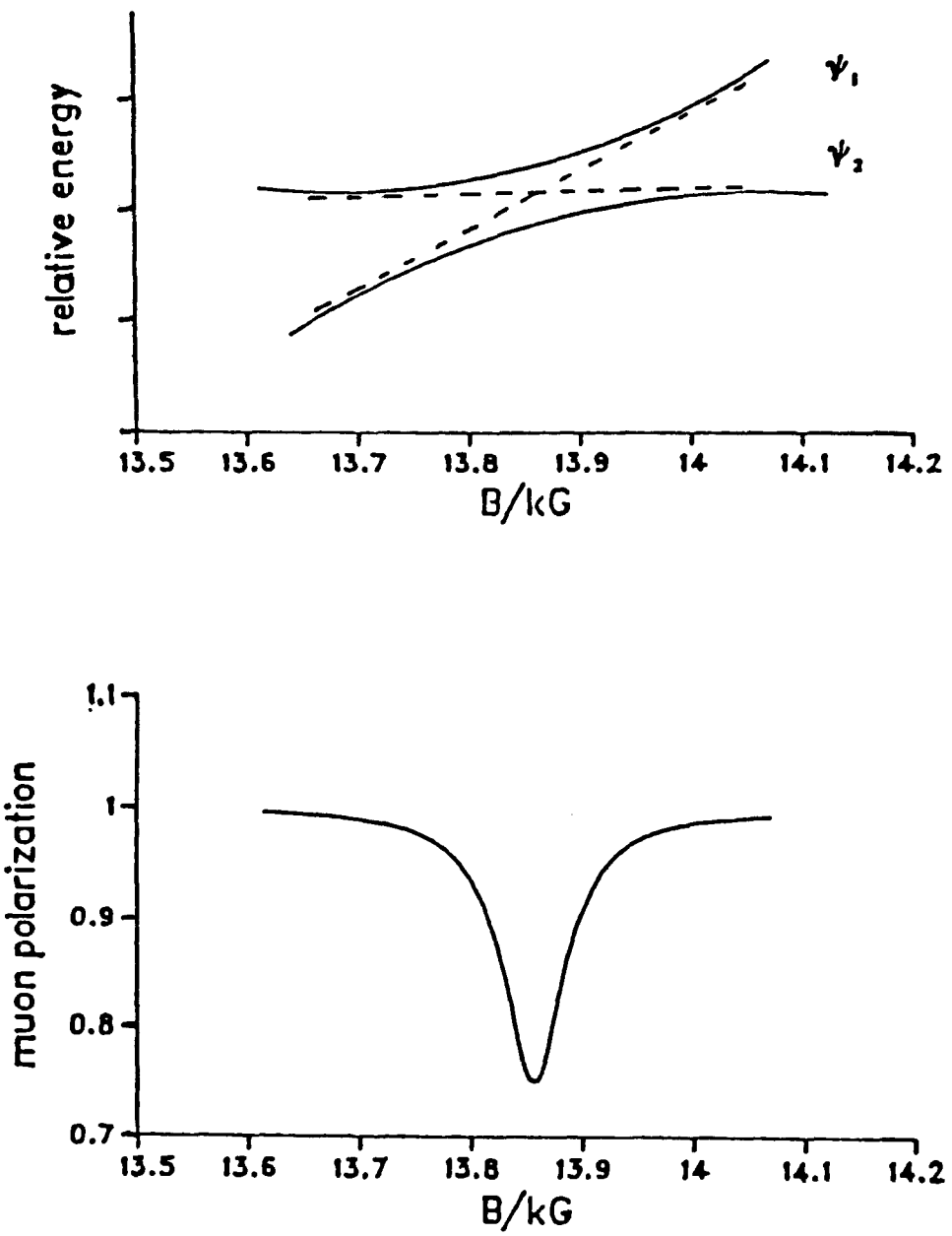

Figure VI.1. Top: A schematic diagram of the energy levels of a $\mu^+ - e^- - p$ system. Bottom: muon polarization curve calculated from eq. VI.4.

hundredths of a MHz in hyperfine frequencies.

The μLCR technique also provides a possibility to detect slowly forming radicals, including those which are evolving from a radical reaction [14]. When muonium forms a radical, with a reaction rate of λ_1, the muons in the radical product do not carry the full initial muon polarization. The time-integrated μLCR signal amplitude (equation VI.6) in the high field limit ($B/B^{\dagger} >> 1$ with $B^{\dagger} = 1.585$ kG for muonium) is modified to [71]

$$P_z(B_0) = 1 - \frac{2}{N}\frac{\lambda_1}{\lambda_1 + \lambda_0} \cdot \frac{\omega_0^2}{\lambda_0^2 + \omega_0^2} \qquad \text{(VI.7)}$$

where λ_0 is the muon decay rate. Thus, as long as the radical formation rate λ_1 is greater than or comparable to the muon decay rate λ_0 and the transition frequency ω_0 is high enough to produce a significant LCR peak, it is possible to observe the μLCR resonance of the radical. The formation rate of the radical can be deduced from the amplitude of the signal. This extends the observable values of λ_1 by four orders of magnitude when compared to that obtained from conventional transverse field μSR.

The μLCR technique allows the determination of the relative signs of the muon and other magnetic nuclear hyperfine frequencies. The information obtained by the technique allows the identification and the determination of electron spin densities of Mu-substituted radicals. In fact, these parameters have been used to study intramolecular motion of such radicals [73-75]. Figure VI.2 shows a typical μLCR spectrum.

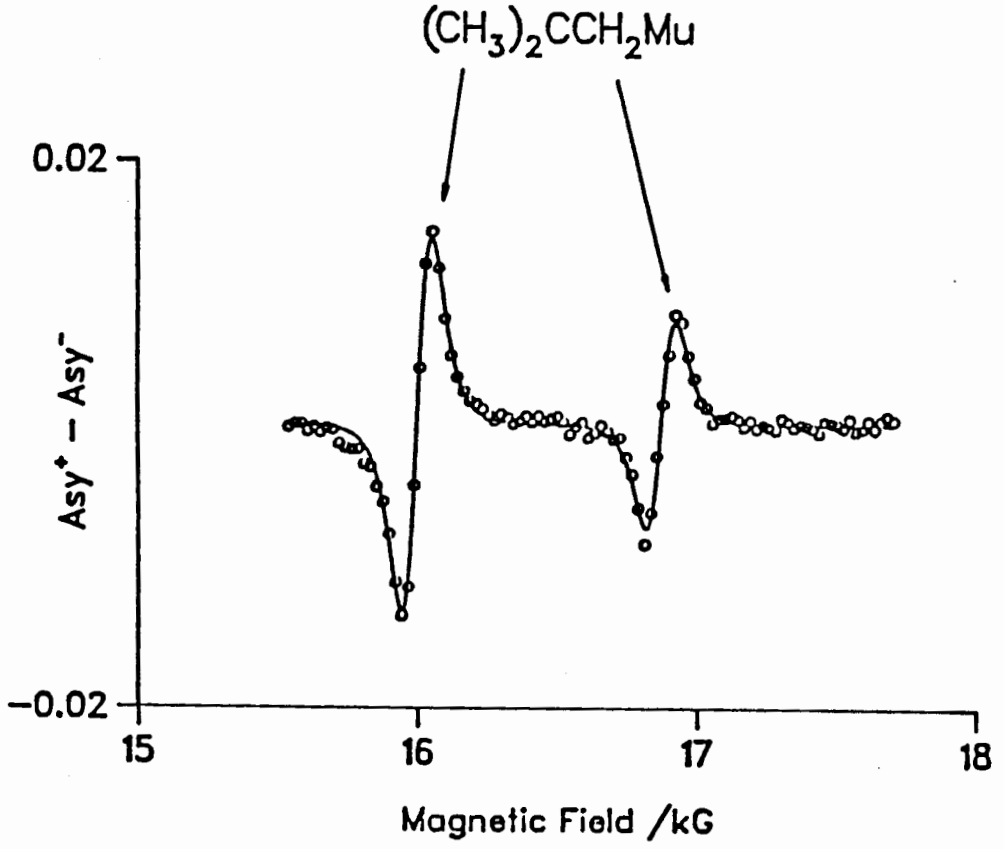

Figure VI.2. μLCR spectrum of $(CH_3)_2CCH_2Mu$ at 104.8 K, showing experimental data (o) and the best fit line.

VI.2. The experimental setup for longitudinal field μLCR experiments

μLCR experiments were done exclusively with longitudinally polarized surface muons and were carried out at the M15 and M20B beam lines. These experiments were performed to measure the hyperfine coupling constants of magnetic nuclei in muonium trihydroxy-substituted cyclohexadienyl radicals. The SLC (University of Tokyo's Superconducting Longitudinal Coil) apparatus was used initially but this was replaced with the arrival of the HELIOS superconducting solenoid. Magnetic fields up to 30 kG are available with the SLC magnet while up to 70 kG are available with HELIOS.

The fundamental difference between μLCR and μSR is that the former is a time-integral technique whereas the latter is time-differential. For μLCR there is no limit on the rate of incoming muons since it is not a single-particle-counting technique. The experimental setup requires only two sets of counters, arranged in forward and backward positions with respect to the sample, and a magnetic field applied along the muon polarization axis (longitudinal field). The forward and backward counters consist of 2 and 4 scintillators each for the SLC and HELIOS setups, respectively. A schematic setup for the SLC setup is given in figure VI.3.

The process of finding the position of the level-crossing resonance involves recording the time-integrated positron rates as a function of magnetic field. However, the raw spectrum is greatly affected by systematic deviations caused by rate-dependent effects. This is conveniently minimized by square-wave field modulation. In this mode, an extra field (usually in the neighbourhood of 50 G) was applied in addition to the main field. The signal is defined as $A^+ - A^-$, the difference in muon asymmetries measured under opposite modulation phases. The

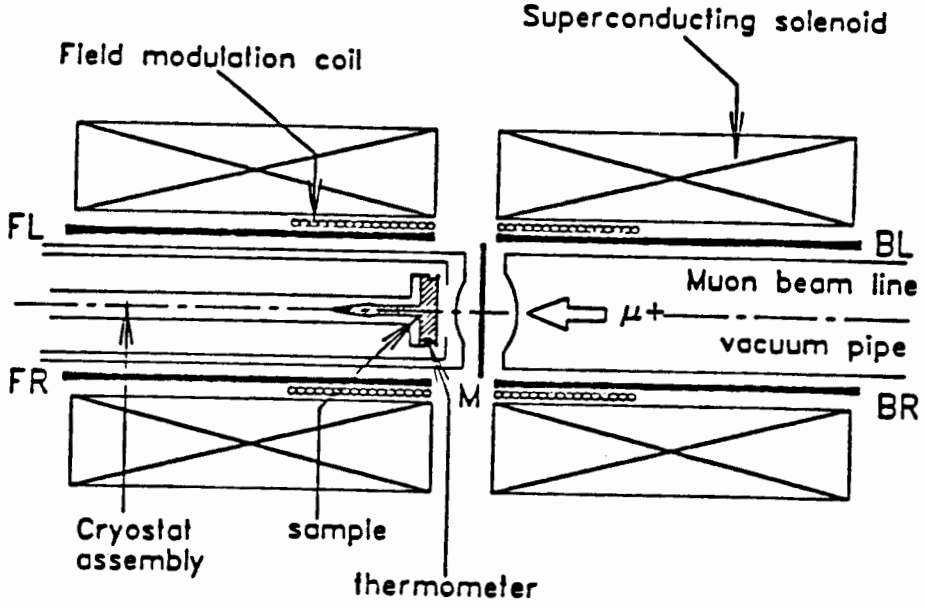

Figure VI.3. Schematic representation of the SLC setup.

asymmetry parameters A^+ and A^- are calculated from the forward and backward integrated asymmetries by the difference-sum method:

$$A^{\pm} = \frac{F^{\pm} - B^{\pm}}{F^{\pm} + B^{\pm}} \qquad \text{(VI.8).}$$

The $\pm$ refers to the phase of the modulation with respect to the main field while F and B refer to the e^+ counts in the forward and backward telescopes, respectively. For resonances wider than the field modulation width the lineshape is approximately field-differential.

The experimental procedure involves accumulating a preset count (typically on the order of 10^6) for each phase of the modulation field. The number of modulation coil flips is typically 20 at each field point. The size of the field increment is usually set at 50 G for rough scans and less for detailed scans.

A schematic diagram of the electronics setup used in a LCR experiment is given in figure VI.4. The signals from the detectors were converted to NIM standard by discriminators before being fed into the scalers. When the preset value is reached, data taking is stopped, scalers are read and the values stored in the computer. The preset scaler is then cleared and the phase of the modulation field is changed. When the desired count is reached, the main field is incremented. Data taking is inhibited if the beam current strays outside a preset tolerance.

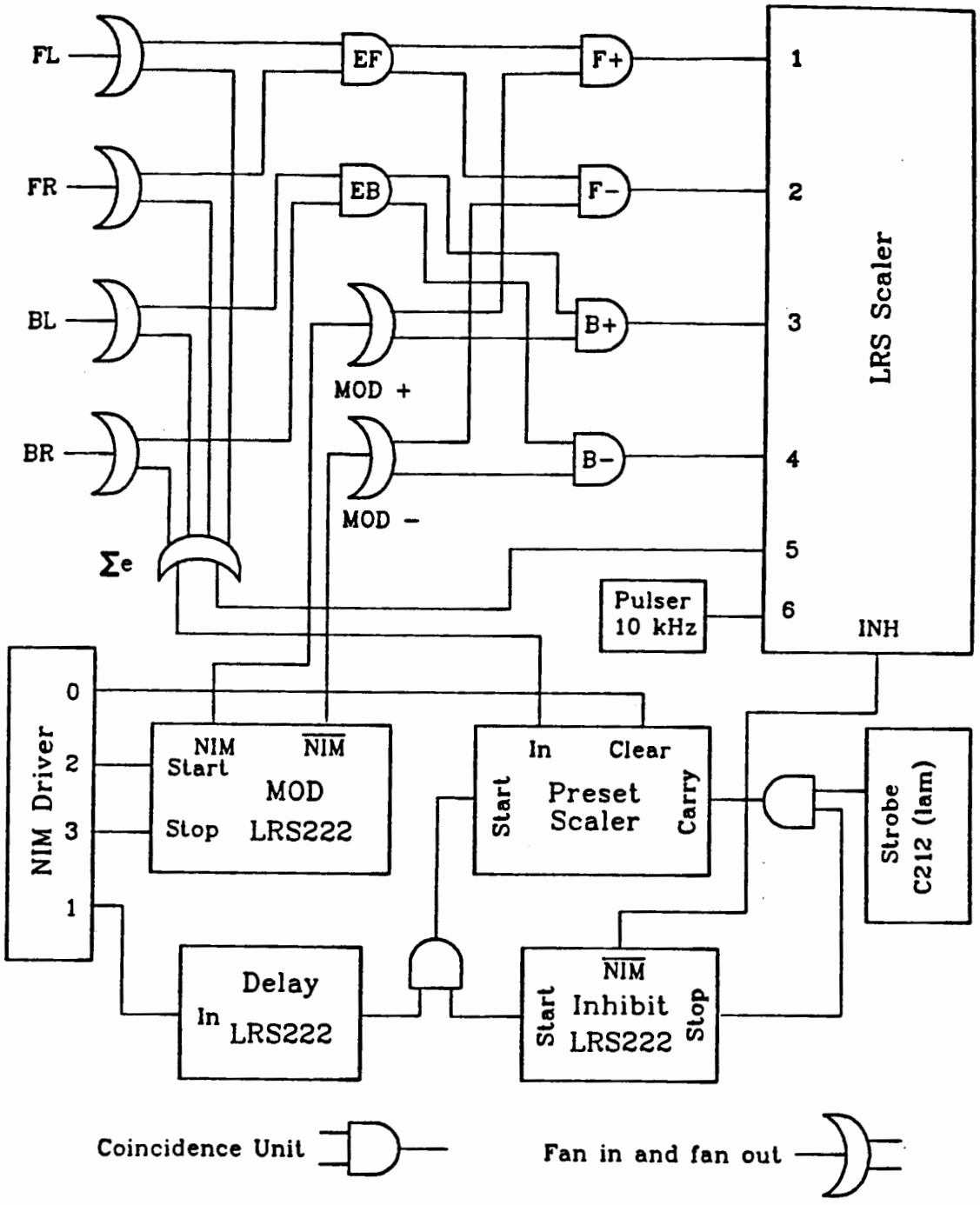

Figure VI.4. Block diagram of the electronics used for μLCR experiments.

CHAPTER VII. MU-SUBSTITUTED RADICALS IN AQUEOUS SOLUTIONS

VII.1. Introduction

One method to study the early chemistry of muonium is to study the kinetics of competing reactions. In fact, "competition kinetics" and "scavenger studies" (addition of reactants to selectively remove transient species) are well established tools of radiation chemistry [30]. Applications of such methods to muon radiolysis of water have mostly involved study of diamagnetic products [4,5,16,17,76]. Unfortunately, the short lifetime of the muon makes it impractical to resolve the precession frequencies of different diamagnetic compounds. Radicals, on the other hand, can be readily distinguished by μSR [77], and the recent advent of muon level-crossing resonance spectroscopy (μLCR) allows unique identification through determination of nuclear hyperfine parameters [13,14,70,71]. Since there is no requirement for phase coherence, as in μSR, radicals may be detected even if they are formed relatively slowly, up to the lifetime of the muon.

In order to test the potential of μLCR for studying radicals formed in dilute solutions, the reaction between muonium and pyrogallol (1,2,3-trihydroxybenzene) in aqueous solution was investigated in this study. The expected products are the two isomeric cyclohexadienyls formed by addition of muonium to one or the other of the unsubstituted positions of the benzene ring (see figure VII.1). Pyrogallol was chosen on account of its high solubility, since it was the goal of the present study to study the μLCR signal amplitudes over as wide a concentration range as possible. Furthermore, it was hoped to detect the radicals by their precession signals in highly concentrated aqueous solutions.

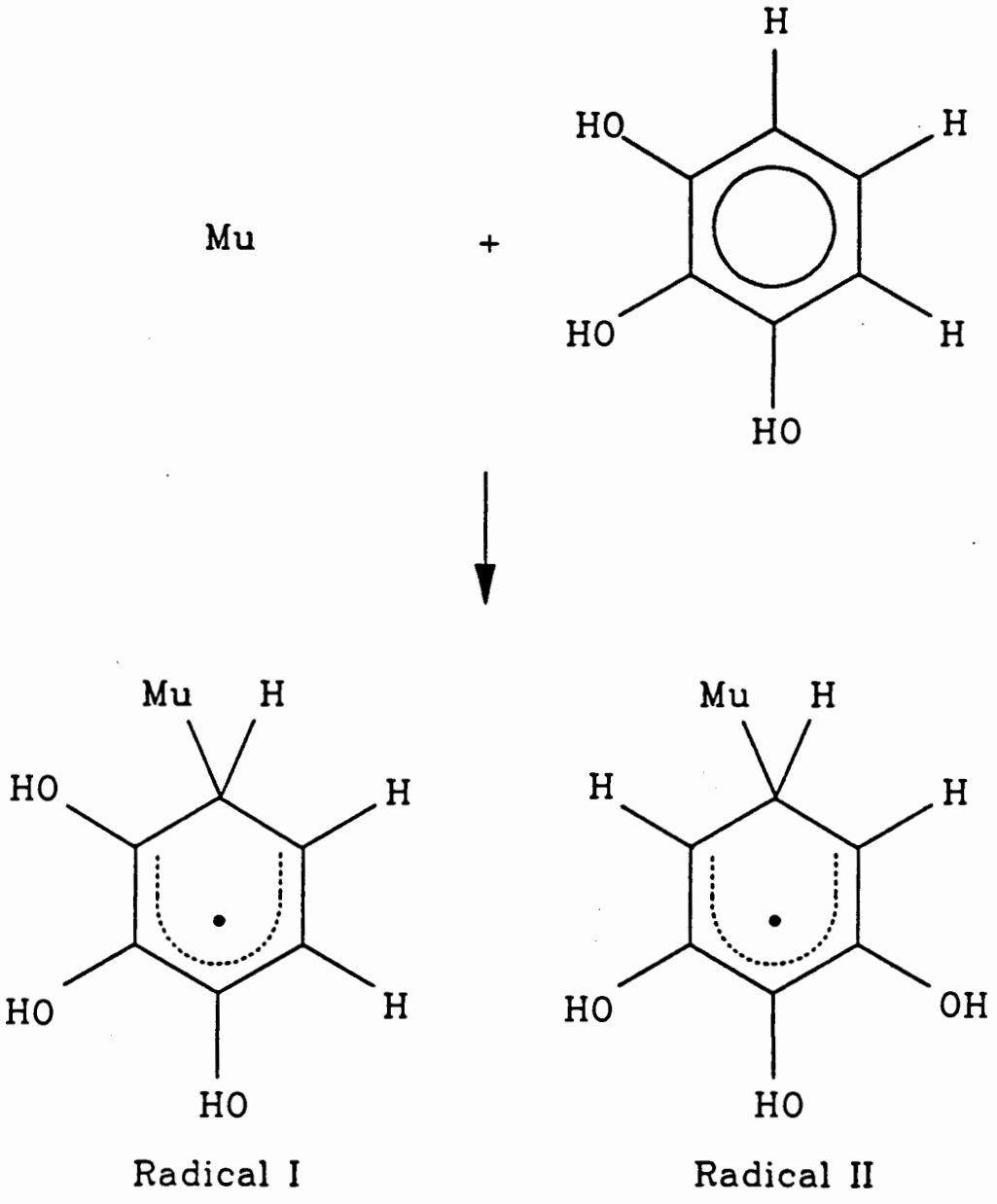

Figure VII.1. Radicals formed by addition of muonium to pyrogallol: 1,2,3-trihydroxycyclohexadienyl (I) and 2,3,4-trohydroxycyclohexadienyl (II).

VII.2. Experimental

Dilutions of pyrogallol were made from an acidified (pH 3 by perchloric acid) stock solution wrapped in aluminium foil to avoid decomposition (pyrogallol is sensitive to light), 15 minutes prior to the actual experiment. Only distilled and deionized water was used. During the experiments, the samples were thermostatted at 25 °C and bubbled with N_2 to ensure that they were in an inert atmosphere to avoid the presence of (paramagnetic) oxygen which can lead to rapid spin relaxation. Sample handling procedures were as described in section IV.6.

VII.2.1. Muonium kinetics

The OMNI apparatus was used for these low field experiments. An applied field of 10 G (where the muonium Zeeman splitting is small) was used. The statistics collected for these experiments were typically 10 million events per histogram.

The relaxation rates of muonium, λ_M, were determined for 4 concentrations (0.1, 0.2, 0.5, and 1 mM) of pyrogallol. Control samples of pure water were used to obtain the background relaxation rate which includes the field inhomogeneity of the electromagnet used. The decay rates are plotted as a function of pyrogallol concentration in figure VII.2. Since the muonium decay kinetics in such dilute solutions are homogeneous and pseudo-first order, λ_M is related to the radical formation rate constant, k_M, by the equation

$$\lambda_M = k_M \cdot [S] + \lambda_o \qquad \text{(VII.1)}$$

where λ_o is the background relaxation rate and [S] represents the concentration of

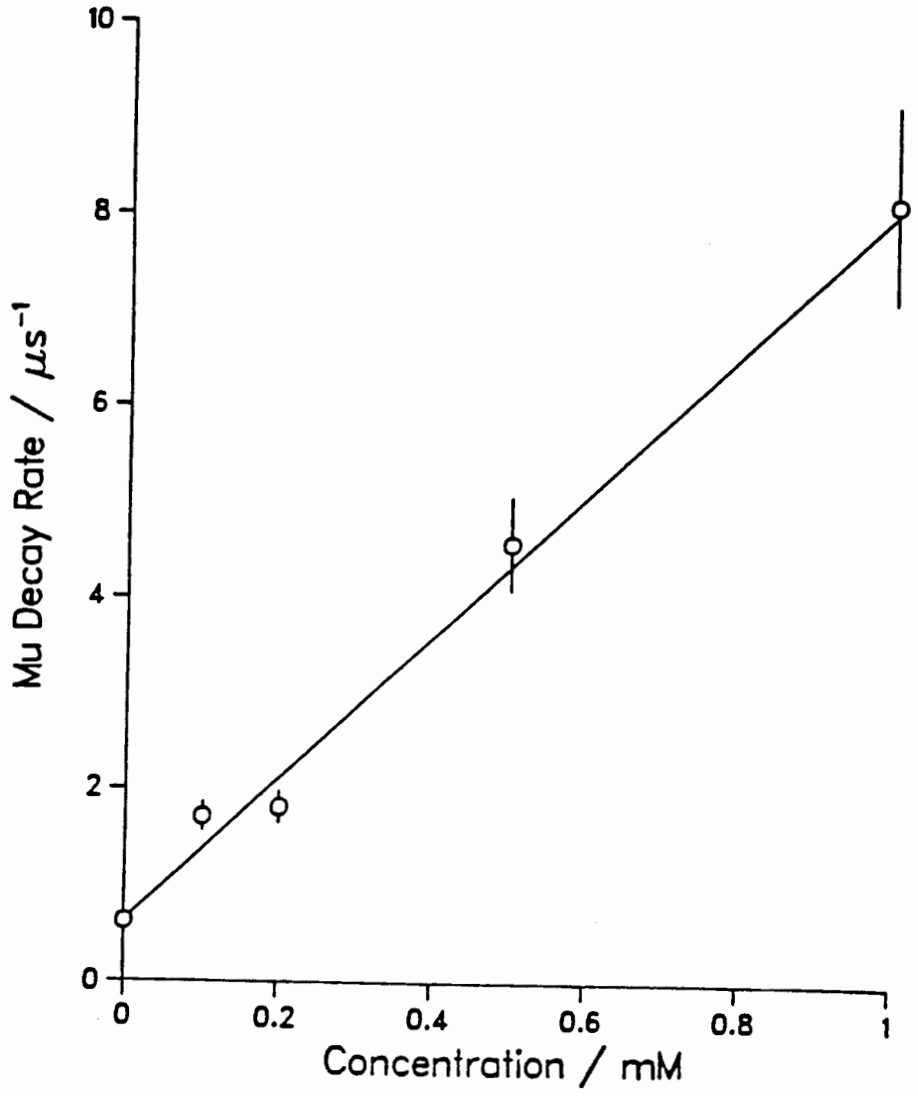

Figure VII.2. Muonium decay rates as a function of pyrogallol concentration.

the solute. Thus, the slope of the best fit line (shown by the straight line in figure VII.2) through the data represents the second order rate constant for the reaction between muonium and the solute (pyrogallol in this case). The value of k_M obtained is (7.4 ± 0.9) x 10^9 M^{-1} s^{-1}. This value is comparable to literature values of k_M = (1.9 ± 0.9) x 10^9 M^{-1} s^{-1} for muonium addition to benzene [78] and 7 x 10^9 M^{-1} s^{-1} for Mu addition to phenol [79]. Evidently, OH enhances the reactivity of the ring, but this is somewhat offset in the case of pyrogallol by the reduced number of unsubstituted sites open to attack (this point will be expanded in a later section).

VII.2.2. Radical products

μSR experiments were used to calibrate the applied magnetic field (using the diamagnetic signal from each sample) and to measure the muon hyperfine frequency of the radicals. The HELIOS and SLC apparatus were used for these experiments. The high transverse field experiments were done with the same experimental set-up as the μLCR experiments (but with spin-rotated muons). For transverse field (TF) μSR experiments, up to 10 million events were collected for each histogram. For longitudinal field μLCR experiments, only the field regions where methylene (CHMu) group resonances were expected were scanned.

Two radicals were detected by high-field μSR on the most concentrated pyrogallol sample (3.4 M). The diamagnetic and lower radical precession frequencies were extracted from the spectra. The muon hfccs were calculated using equations (II.14) and (II.15):

$$A_\mu = \frac{(\nu^e + \nu^\mu)^2 - \nu_o^2}{2\nu_o} \qquad \text{(VII.2)}$$

where $\nu_o = 2\nu^- + \nu^e - \nu^\mu$, and values of 470.7 MHz and 481.5 MHz were obtained. A Fourier transform spectrum is given in figure VII.3.

The field region where the methylene (CHMu group) protons are expected was scanned and two signals were found, at 18.9 kG and 19.4 kG, as shown in figure VII.4. They were assigned to two separate radicals, as the resonances from the other protons are found at quite different fields [80]. The resonance field, B_0, depends on both the muon and proton coupling constants as in equation (VI.1). The lower resonance was assigned to radical I and the upper to radical II (refer to figure VII.1 for structures), since the calculated proton couplings (A_p = 115.5 MHz and 119 MHz) then give similar isotope effects,

$$(A_\mu/A_p)/(\gamma_\mu/\gamma_p) \quad = \quad 1.28 \qquad \text{(VII.3)}$$

at a value typical for muonium-substituted cyclohexadienyls [81]. The assignment of the two radical structures (I and II) follows from known substituent effects [77]. In addition, on the basis of the ratio of addition sites, radical I is expected to form more readily than radical II by a factor of two.

VII.2.3. LCR signal amplitudes in pyrogallol

μLCR spectra were recorded for 10 concentrations of pyrogallol from 0.05 mM to 3 M at 25°C. Signal amplitudes were extracted from computer fits of the spectra. Since several uninteresting factors (such as apparatus geometry) affect signal amplitudes (A), only relative values (A/A_0) are reported in table VII.1.

A_0 is the signal amplitude which corresponds to 100% muon polarization. The standard used was 50% manganous nitrate, for which $A_0 = 0.209 \pm 0.002$, as determined from muon decay signals in longitudinal fields from 15 – 25 kG. The

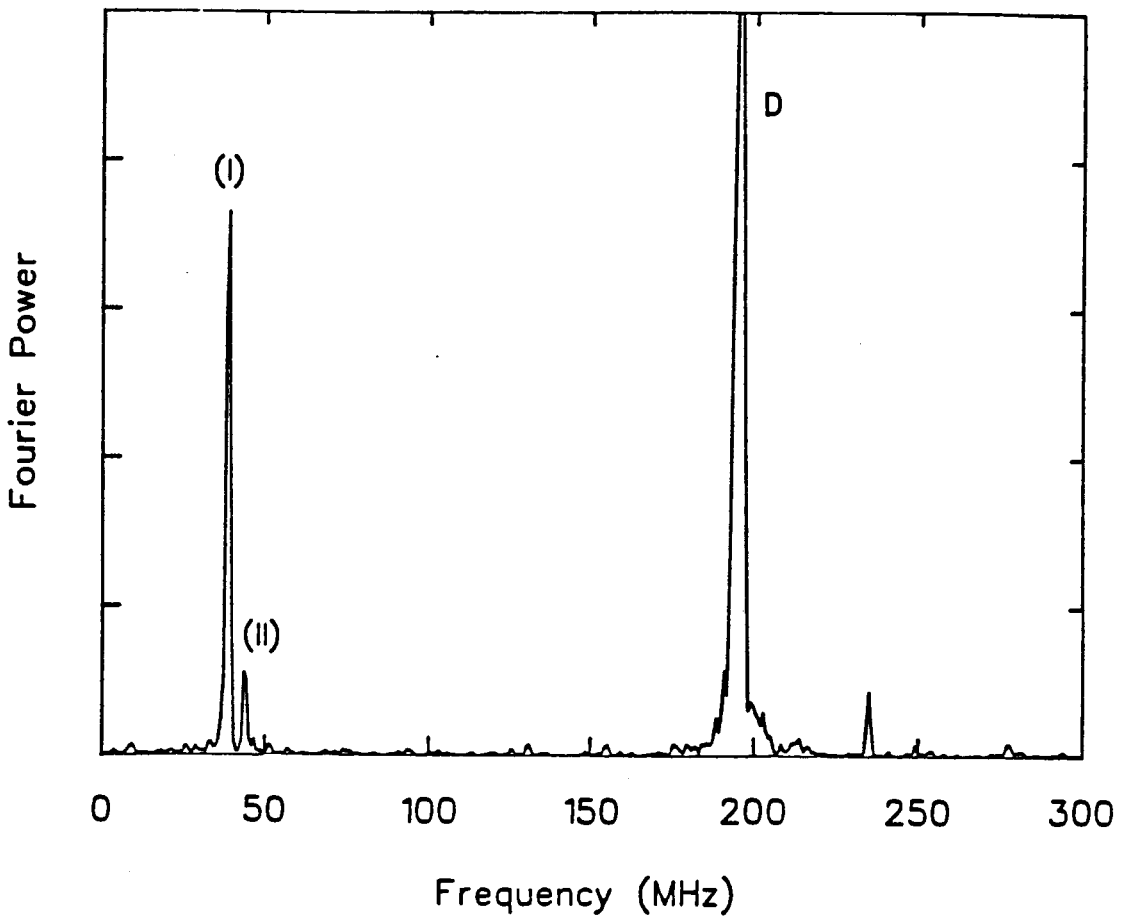

Figure VII.3. Fourier transform spectrum of pyrogallol in aqueous solution. The signals marked I and II arise from the cyclohexadienyl radicals whose structures are depicted in Figure VII.1. The diamagnetic signal D is truncated on the scale of this figure.

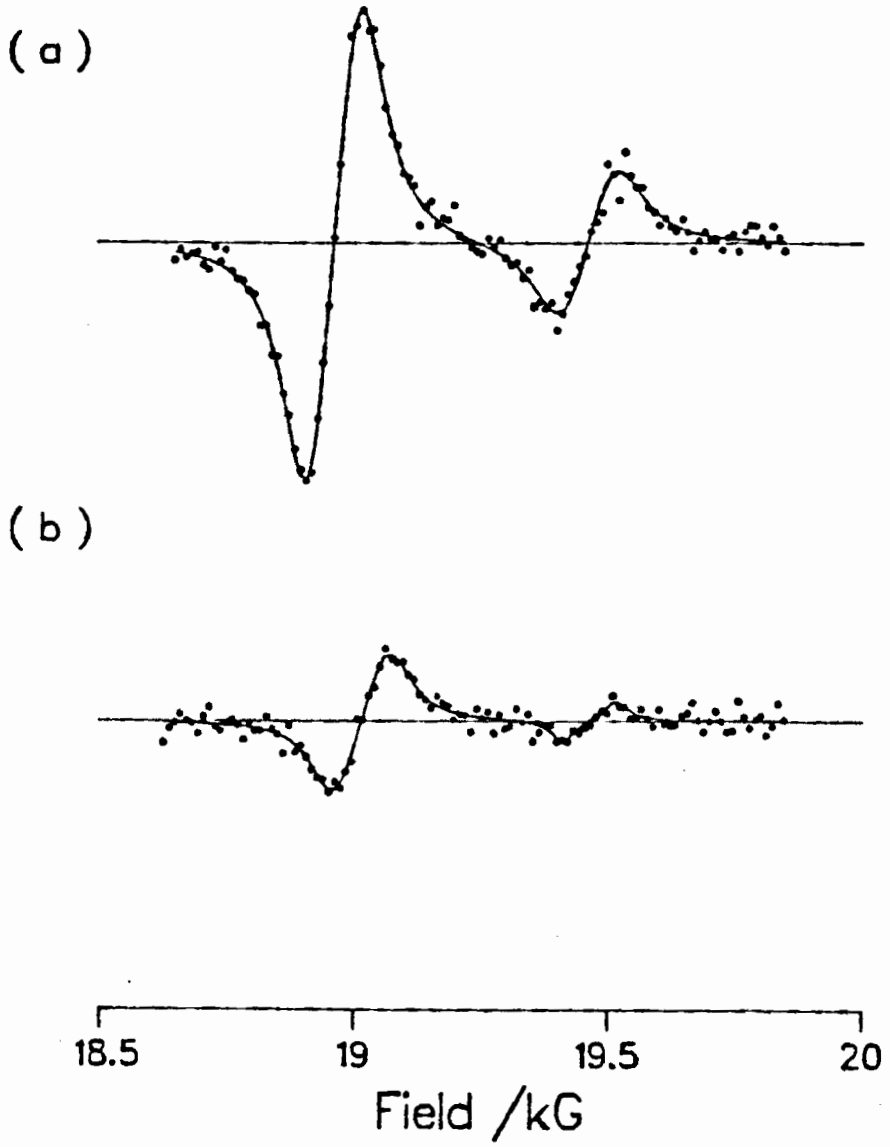

Figure VII.4. μLCR spectra recorded for aqueous solutions of pyrogallol at 298 K. (a) 3 M and (b) 1×10^{-4} M. The signals are due to methylene proton resonances in the two cyclohexadienyl isomers I and II (at $\approx$19.0 kG and 19.5 kG, respectively).

Table VII.1. μLCR signal amplitudes and polarization fractions

Pyrogallol Conc. (M)	Muonium lifetime (ns)	Radical I		Radical II		Total P_R
		A/A_0	P_R	A/A_0	P_R	
5×10^{-5}	2700	0.0084	0.117	-	0.029*	0.15
1×10^{-4}	1350	0.0123	0.112	0.0030	0.027	0.14
2×10^{-4}	680	0.0196	0.131	0.0048	0.032	0.16
3×10^{-4}	450	0.0221	0.130	0.0050	0.029	0.16
0.001	135	0.0254	0.121	0.0060	0.028	0.15
0.003	45	0.0333	0.147	0.0088	0.039	0.19
0.01	13.5	0.0409	0.176	0.0099	0.043	0.22
0.1	1.35	0.0454	0.194	0.0105	0.045	0.24
1	0.14	0.0494	0.211	0.0139	0.059	0.27
3	0.045	0.0451	0.192	0.0147	0.063	0.26

* Extracted from fit

calibration procedure may introduce a systematic error as high as 10% in the absolute values of the signal amplitudes, but this does not affect the trend with concentration, which is the main focus here. The results are plotted in figure VII.5.

The amplitudes of a μLCR signal can be predicted theoretically, as given in equation (VI.7) [71]:

$$A/A_0 = \frac{1}{4} \cdot \frac{\omega_0^2}{\lambda_0^2 + \omega_0^2} \cdot \frac{\lambda_M}{\lambda_M + \lambda_0} \cdot P_R \qquad \text{(VII.4).}$$

where λ_0 is the rate of any process which takes the muon out of resonance, including muon decay and reaction of the radical. ω_0 is 2π times the LCR transition frequency. The factor of ¼ and the following factor describe the change in muon polarization at resonance. The third term accounts for reduction of the signal when the muonium decay rate (λ_M) is comparable to λ_0. Finally, P_R represents the fraction of muon polarization available in muonium for transfer to the radical. Deviations from equation (VII.4) can occur in the event of spin exchange or other spin relaxation processes [82]. However, small contributions from these processes (of similar magnitude to the inverse muon lifetime) can be incorporated in the rate λ_0.

Since λ_M is simply given by the product of k_M and the pyrogallol concentration, equation (VII.4) can be tested against the data displayed in figure VII.5. A good fit was only possible for the low concentration data (< 3 mM). In that range, both sets of data for the two radicals I and II were fitted simultaneously, using only three variable parameters: λ_0 and the polarization fractions P_R(I) and P_R(II). k_M was fixed at the value found in the muonium kinetics study, while ω_0 was calculated from equation (VI.3):

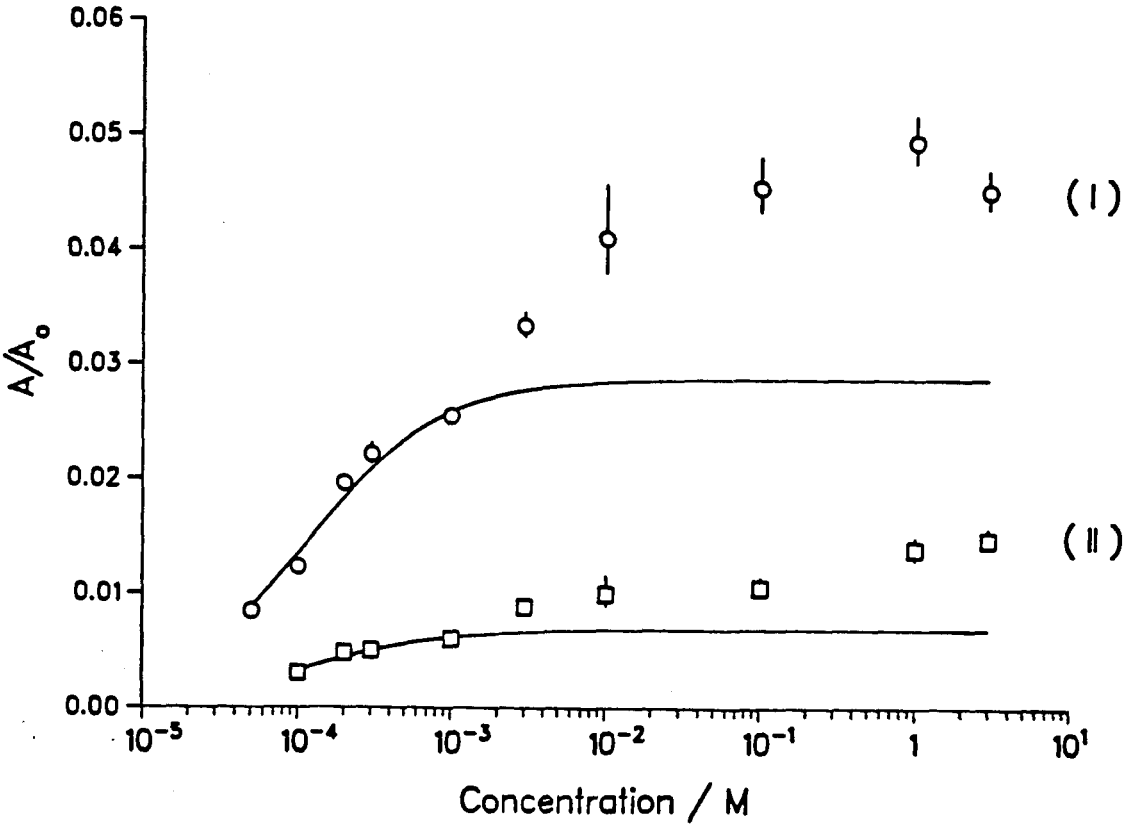

Figure VII.5. Relative signal amplitudes for radicals I (o) and II (□) as determined from μLCR experiments on aqueous solutions of pyrogallol. The curves through the points represent a simultaneous fit of eq. (VII.4) to the two sets of data below 3 mM. The fit parameters are given in table VII.2.

$$\omega_0(M,B_0) \approx \frac{\pi A_\mu A_k}{B_0 \gamma_e} \qquad \text{(VI.3).}$$

A common value of ω_0 was used for the two radicals since there is little difference. The parameters of the best fit are given in table VII.2. The value for λ_0 is about twice the rate due to the muon lifetime alone ($\tau_\mu^{-1} = 4.5 \times 10^5\ s^{-1}$), presumably due to radical decay or spin relaxation. This was confirmed by recording the time dependence of the muon signal at the resonance field: an additional decay rate of about $5 \times 10^5\ s^{-1}$ was found.

VII.3. Discussion

VII.3.1. Homogeneous Muonium kinetics

The quality of the fit in the low pyrogallol concentration range is good support for the validity of equation (VII.4) and the homogeneity of muonium kinetics at low concentrations of reactants. The ratio $P_R(I)/P_R(II)$ reflects the relative rates of radical formation. Radical (I) is favoured over II by a factor of 4.2, or in terms of site specificity, Mu attack at the 4 (or 6) position of the pyrogallol ring is preferred by a factor of 2.1 over position 5. This is not surprising since it is known that the regioselectivity of H atom addition to phenol follows the order: *ortho* > *para* >> *meta*, and the effect is expected to be the same for Mu. Radical I contains hydroxy groups in all three positions, while radical II has two hydroxy groups in *meta* positions.

Table VII.2. Parameters used to fit the low concentration data od muonium addition to pyrogallol

Parameter	Value[†]	Source
k_M (M^{-1} s^{-1})	7.4 x 10^9	Mu decay experiment
ω_0 (rad s^{-1})	3.26 x 10^6	calculated
λ_0 (s^{-1})	8.4(7) x 10^5	fit variable
P_R(I)	0.122(4)	fit variable
P_R(II)	0.029(2)	fit variable

[†] Number in brackets = uncertainty in final digit.

VII.3.2. Competition kinetics

The sum of $P_R(I)$ and $P_R(II)$ is 0.15, close to the magnitude of the muonium fraction detected by μSR in pure water, 0.19 (see Chapter V). It is not clear if the difference is significant, given the uncertainty in the asymmetry calibration and the sensitivity of the fit to points in the concentration range where the theoretical function reaches its upper limit. Nonetheless, the results show that most, if not all of the muonium polarization which survives to 100 ns is transferred to free radical products. At shorter times there is a competition between the development of the missing fraction and chemical reaction with pyrogallol to form the radical adducts. The deviation between the theoretical curves and the data in figure VII.5 is a measure of this competition. In terms of equation (VII.4) there is a concentration dependence to P_R at short times (< 100 ns, when direct observation of muonium or radical signals is not possible). Equation VII.4 was inverted to calculate values of P_R from the experimental data and the parameters of table VII.2. The results are also given in table VII.1, and the sum of the polarization for the two radicals is plotted as a function of muonium lifetime (λ_M^{-1}) in figure VII.6.

Although it is derived from radical polarization fractions, the P_R sum plotted in figure VII.6 actually represents the fraction of muon polarization present in muonium at the moment of reaction to form a radical. In this respect the radicals are acting as a "trap" to capture the magnitude of the muonium fraction at various times after a muon has stopped in the sample. At early times the muonium fraction is almost twice its value at later times, where homogeneous kinetics holds. This agrees with findings in the previous chapter concerning the initial size of the Mu fraction and the smaller fraction measurable at longer times in pure water [16,76].

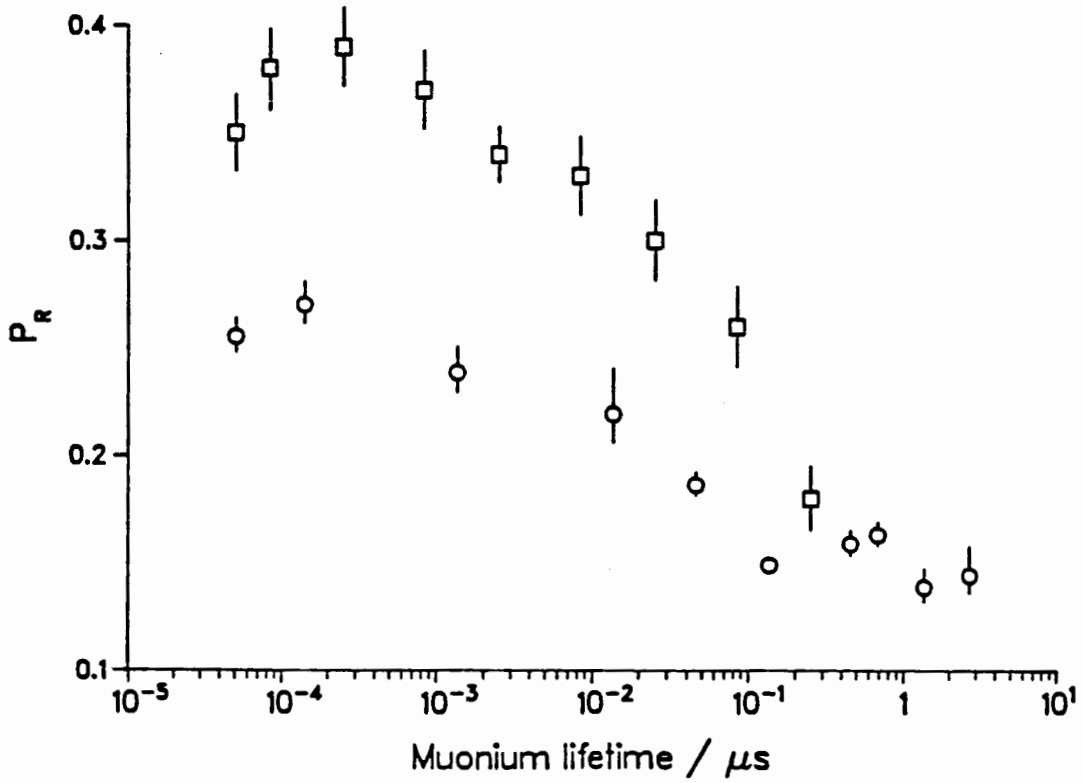

Figure VII.6. Polarized muonium fraction as a function of the chemical lifetime of muonium. (o) this work; (□) Venkateswaran *et al* [83].

Recently, Venkateswaran *et al* measured the yields of free radicals in another aqueous system [83]. They used acrylamide to trap muonium. In order to show the similarities between the results, their data are reproduced in figure VII.6. There is an obvious difference in scale between the two data sets, most likely due to a systematic error in the calibration of signal amplitude of the set of data from this work. Furthermore, direct comparison is inappropriate since Venkateswaran *et al* derived their values of P_R from a combination of signal amplitudes and resonance line widths, and the latter are not expected to be the same for the two different chemical systems. Apart from the scale difference, there are intriguing similarities in shape for the two sets of data, notably the drop in P_R at the shortest muonium lifetimes (times < 100 ns).

In accord with the results presented in Chapter V, the variation of P_R with time is ascribed to both reactions and non-reactive spin-exchange encounters of muonium with the paramagnetic transients produced in the radiolysis of water as the muon thermalizes. Venkateswaran *et al* interpreted their values of P_R directly as muonium yields (chemical fractions, as opposed to fractions of muon spin polarization). They discounted electron spin exchange as one of the explanations for the muon spin depolarization on the grounds that the nuclei are effectively decoupled from the unpaired electron for a radical in high magnetic fields. This argument is not accepted since it assumes the muon polarization in muonium is damped at a rate which depends on the electron spin relaxation rate reduced by a field-dependent factor [84]. For very high fields or rates of electron relaxation, the muon behaves as if it were "free", *i.e.* the muon spin is decoupled from the electron spin. The situation considered here is more complicated. As Mu and a

paramagnetic e^-_{aq} come together, their spin functions gradually evolve under the increasing influence of the electron exchange interaction. In principle, mixing can occur between the singlet electron pair combination and either the $M_s = 0$ or $M_s = -1$ triplet state, according to the relative magnitudes of the exchange interaction (a function of pair separation) and the electron Zeeman energy. The full theory has yet to be developed, but it is clear from magnetic resonance studies of reacting radicals (CIDNP and CIDEP effects [85]) that the evolution of radical pair spin functions is nuclear spin dependent, even in high magnetic fields.

Whatever the cause of muon depolarization, chemical reaction of muonium alone, or the combination of reaction and spin exchange effects, in either case it is true to state that the time dependence of P_R reflects the probability of encounter between muonium and transient products of the muon radiolysis of water. The characteristic time for this encounter is about 3 ns, as estimated from the half-way point for change in P_R, *i.e.* the point at which radical formation is equal to muon depolarization. This time is in good agreement with estimates from the residual polarization data.

VII.4. Conclusion

The concentration dependence of the radical amplitudes in pyrogallol in low concentration of solutes is explained by homogeneous kinetics of muonium addition to pyrogallol. At higher solute concentrations, formation of trihydroxycyclohexadienyl radicals is in competition with the development of the missing fraction (reaction and spin-exchange of muonium with e^-_{aq}).

CHAPTER VIII. SUMMARIES OF COLLABORATIVE PROJECTS

VIII.1. Introduction

The author of this thesis was a collaborator in various research projects with other μSR scientists. The topics of these collaborations are not directly related to radiolysis effects in muonium chemistry. Detailed accounts of these projects are beyond the scope of this thesis but summaries of them will be given in the following sections of this chapter.

VIII.2. Pressure-dependent muonium kinetics in aqueous solutions

In principle, valuable information on the transition state of a chemical reaction can be gained by the pressure dependence of the rate constant, k. The volume of activation is defined by

$$\Delta V^{\ddagger} = -RT \left(\frac{\partial \ln k}{\partial P} \right)_T \qquad \text{(VIII.1)},$$

and is interpreted as the difference in partial molar volume between the transition state and the separated reactants. In practice, interpretation is difficult, and $\Delta V^{\ddagger}$ has mostly been used in a semi-quantitative manner in the classification of reaction mechanisms [86]. Hentz *et al* [87-91] studied the effect of pressure on hydrogen atom reactions and classified these reactions in aqueous solutions into two categories: (1) activation-controlled reactions of H have $\Delta V^{\ddagger} = -5$ cm^3 mol^{-1}, and (2) diffusion-controlled reactions of H have $\Delta V^{\ddagger} = +2$ cm^3 mol^{-1}. They also proposed two models which describe the transition state of the activation-controlled reactions: (1) the small H atom is completely accomodated within the volume

occupied by the reactant molecule, *i.e.* the partial molar volumes of reactant and transition state are equal and the partial molar volume of H alone determines the activation volume

$$\Delta V^{\ddagger} = -\bar{V}(H) \qquad \text{(VIII.2)},$$

and (II) the volume of the transition state is the sum of the volumes of H and the reactants with the relevant H volume being the van der Waals volume, $V_w(H)$, so that

$$\Delta V^{\ddagger} = V_w(H) - \bar{V}(H) \qquad \text{(VIII.3)}.$$

Model I implies that $\bar{V}(H) = 5$ cm^3 mol^{-1}, and model II gives the upper limit of 9.4 cm^3 mol^{-1} (based on the van der Waals radius for H of 0.12 nm used by Hentz *et al*). Given that the molar volume of water is 18 cm^3 mol^{-1}, both the above interpretations predict that $\bar{V}(H) < \bar{V}(H_2O)$. On the other hand, Klein *et al* [92,93] suggested that the H_2O molecules form a clathrate cage around the H atom and concluded that the H atom is larger than a waer molecule. It does not necessarily follow, however, that $\bar{V}(H) > \bar{V}(H_2O)$, since the ordering of water molecules in the clathrate-structure would make a negative contribution to the partial volume of H.

Apparatus was developed to study the pressure dependence of Mu kinetics [51]. This was the first study of Mu kinetics at high pressures in condensed matter. Decay rates of Mu in aqueous solutions of NO_3^- and MnO_4^- were investigated as a function of pressure. The rate constant for the activation-controlled reaction of Mu with NO_3^-, k, was determined to be 1.5 x 10^9 M^{-1} s^{-1} while that for the diffusion-controlled reaction with permanganate was 2.5 x 10^{10} M^{-1} s^{-1}. The activation volumes obtained for the two reactions were $\Delta V^{\ddagger} = -7.1 \pm 1.5$ cm^3 mol^{-1} for Mu +

NO_3^- and $\Delta V^{\ddagger} = 3.1 \pm 1.6$ cm^3 mol^{-1} for Mu + MnO_4^-. For the activation-controlled reaction, the activation volume of Mu is larger than that of the H atom by 2 cm^3 mol^{-1}. A measure of the size of the atom could be [93]

$$R_{eff} = (R_w^2 + 3L_T^2)^{1/2} \quad \text{(VIII.4)}$$

where R_w is the van der Waals radius and L_T^2 is the thermal wavelength:

$$L_T^2 = \hbar/(mk_BT)^{1/2} \quad \text{(VIII.5)}$$

with k_B representing the Boltzmann constant, m the mass of the particle and $\hbar$ the Planck's constant. Using R_w = 0.21 nm [94], the calculated values of R_{eff} are 0.22 nm for H and 0.30 nm for Mu. These radii correspond to large free volumes, 27 and 64 cm^3 mol^{-1}, respectively which are much bigger than the corresponding partial molar volumes. Klein *et al* deduced from molecular dynamics simulations that the clathrate cage around Mu contains 23 water molecules instead of the 18 around H [92,93]. The larger volume occupied by Mu reflects the importance of quantum delocalization of the smaller particle. Although the free volume available to Mu is almost 50% greater than H, the ordering of the extra 5 water molecules almost compensates, with the result that the partial molar volumes are not very different. Futher considerations led to the suggestion that there is a complete loss of H solvation in the transition state, *i.e.* a modification of Hentz's second model. This would amount to replacing the van der Waals volume in equation VIII.3 (Hentz's model II) by V_{eff} as calculated by equation VIII.4, *i.e.* including the zero-point motional effects. Thus, the activation volume equals the difference between the effective volume of the atom and its partial molar volume, or simply the contribution to the partial molar volume caused by the ordering of the water molecules in the

clathrate cage. In this model, the partial molar volume of H was determined to be 32 cm^3 mol^{-1} and that of Mu 72 cm^3 mol^{-1}.

As for the diffusion-controlled reactions, given the notion of a clathrate cage around the solvated atom, it is reasonable to expect that diffusion of the solvated atom is limited by solvent properties and that the increased pressure would tend to suppress the formation of a new cavity adjacent to the occupied cage, so that diffusion is slowed. This is supported by the positive sign of the activation volumes for this type of reaction of Mu and H.

VIII.3. Intramolecular motion in the Mu-substituted tert-butyl radical

Although simple alkyl radicals are commonly held to have a planar configuration at the trigonal carbon [95], the most recent theoretical and experimental investigations conclude that only the methyl radical is planar, and that all other simple alkyls exhibit deviations from planarity in their lowest energy geometries [96,97]. For the tert-butyl radical, the ^{13}C hyperfine coupling constant (A_C) of the central carbon (C_α) falls with decreasing temperature [98], goes through a minimum, and rises at still lower temperatures [99]. This behaviour is consistent with pyramidal inversion in a shallow double-well potential. The barrier to inversion was estimated to be about 2kJ mol^{-1} above the potential minimum [99]. However, independent calculations found that the torsional modes of the methyl groups are strongly coupled to the low-frequency inversion mode, and the lowest energy path to inversion involves simultaneous rotation of the methyl groups to optimize the interaction between the β C–H bonds and the radical center [100,101]. Further theoretical calculations estimated the barrier to the concerted rotation-inversion to be 5-7 kJ mol^{-1}, depending on the basis set and type of motion [102,103].

The muon (A_μ) and proton (A_p) hyperfine coupling constants for the muon-substituted tert-butyl radical $(CH_3)_2CCH_2Mu$ were measured over a wide range of temperature in isobutene. The results are shown in figure VIII.1. The averaged hyperfine constant for the CH_2Mu group, $\bar{A}$, is defined as $\frac{1}{3}(A_\mu' + 2A_p)$, where A_μ' = 0.31413 A_μ. The temperature dependence of the hyperfine coupling constants was analyzed by Mr. D. Yu [74] in the manner of Ramos *et al* [104], assuming a sinusoidal V_2 potential with two-fold symmetry. The V_2 potential was determined to be 2.1 kJ mol^{-1} for the liquid phase (solid line in figure VIII.1) and 3.4 kJ mol^{-1} for the frozen liquid (broken line in figure VIII.1).

The most distinctive feature of the results is the discontinuity in A_μ at the melting point of isobutene. Since the variation of hfcc with temperature arises from the change in occupancy of the various torsional or vibrational states in the radical, the sudden change on freezing suggests that interaction with the lattice in the solid influences the distribution of motional states. The extrapolations of the liquid and solid data converge at 0 K, which implies that the minimum energy structure is identical for the two states, only the temperature dependence changes. This led to the suggestion that methyl rotation in the liquid phase is facilitated by simultaneous inversion of the carbon skeleton, but that the inversion mode is somewhat hindered in the solid.

$\bar{A}_\mu$, the average hyperfine coupling constant for the CH_2Mu group is larger than that of the unsubstituted tert-butyl radical (A_t = 63.7 MHz [105]). Furthermore, the high-temperature limiting values of A_μ' and $A_p(CH_2)$ are 71.0 and 64.5 MHz, respectively. This difference represents a "residual" iostope effect remaining after taking account of the preferred conformation. Its direction is consistent with the notion that the C–Mu is longer than a regular C–H bond

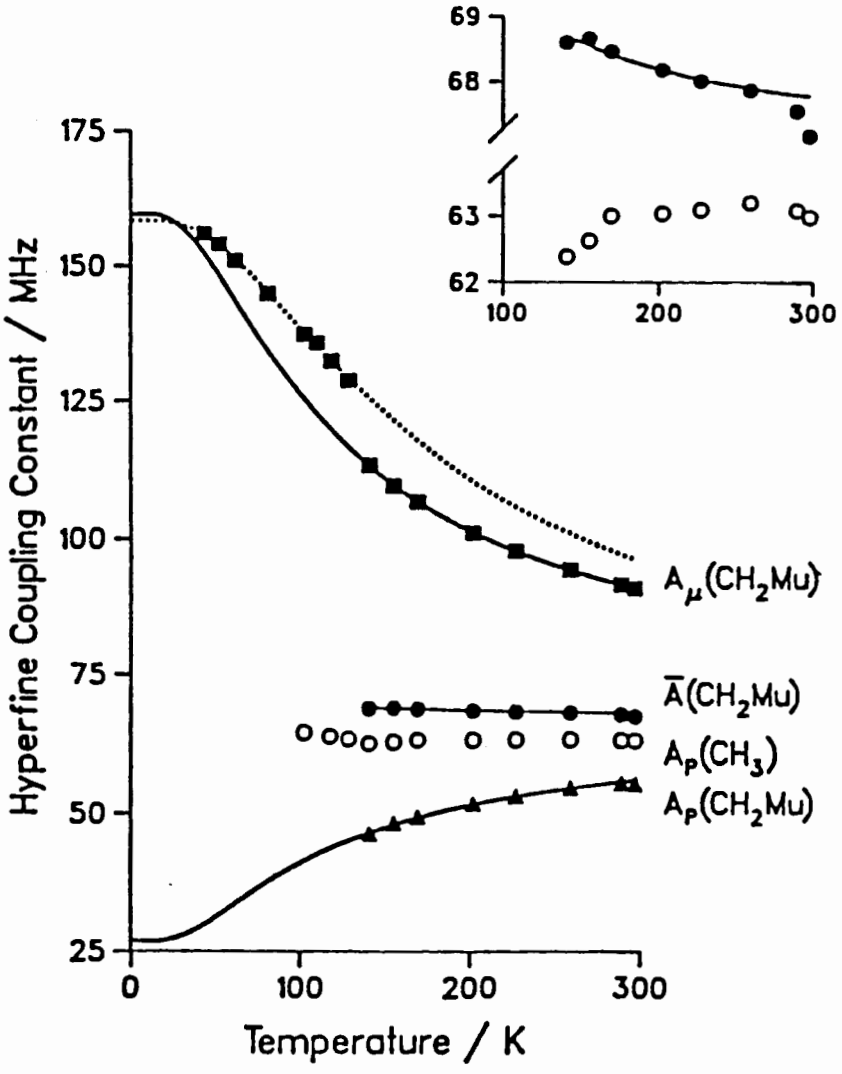

Figure VIII.1. Hyperfine coupling constants in $(CH_3)_2CCH_2Mu$. The solid lines correspond to fit for the liquid solution data, the dotted line to the frozen solution.

[75,77,106,107]. This increased C–Mu bond length should promote hyperconjugation. As a result the C–Mu bond is tilted towards the radical orbital. The C–H bond length is not much affected by the neighboring muonium (the values of A_p are close to those of A_t).

VIII.4. Structure and intramolecular motion of Mu-substituted cyclohexadienyl radicals

The electronic structure of the cyclohexadienyl radical has been the subject of considerable theoretical and experimental investigation over the past 25 years [108-117]. Early interest was centered on the anomalously high hyperfine coupling constant (hfcc) of the methylene protons and the possible deformation of the equilibrium structure by out-of-plane deviation of the C(6) methylene group (see figure VIII.2 for the definition of the ring positions). The high methylene proton hfcc has been explained by extension of the conjugated π system to the antisymmetric methylene group orbital [114]. However, uncertainties remain as to the nature of vibration of the methylene group. The equilibrium structure of C_6H_7 undoubtedly has a planar ring, but out-of-plane deformation of C(6) is relatively facile [116]. The H(6) coupling in C_6H_7 itself falls with temperature, but the opposite is true for some substituted cyclohexadienyls, consistent with a non-planar structure in which the single methylene H takes the equatorial position [114,117]. Early measurements of A_μ and A_C of ^{13}C enriched benzene and benzene with substituents (C_6X_6 where X = H, D, F) showed that Mu subsitution strongly perturbs the couplings of the methylene group substituents (Mu, X), but has little effect on the more distant nuclei [13,80,118]. In particular, A_μ in C_6H_6Mu is 20% higher, while A_p is 6% lower, than the methylene proton coupling in C_6H_7.

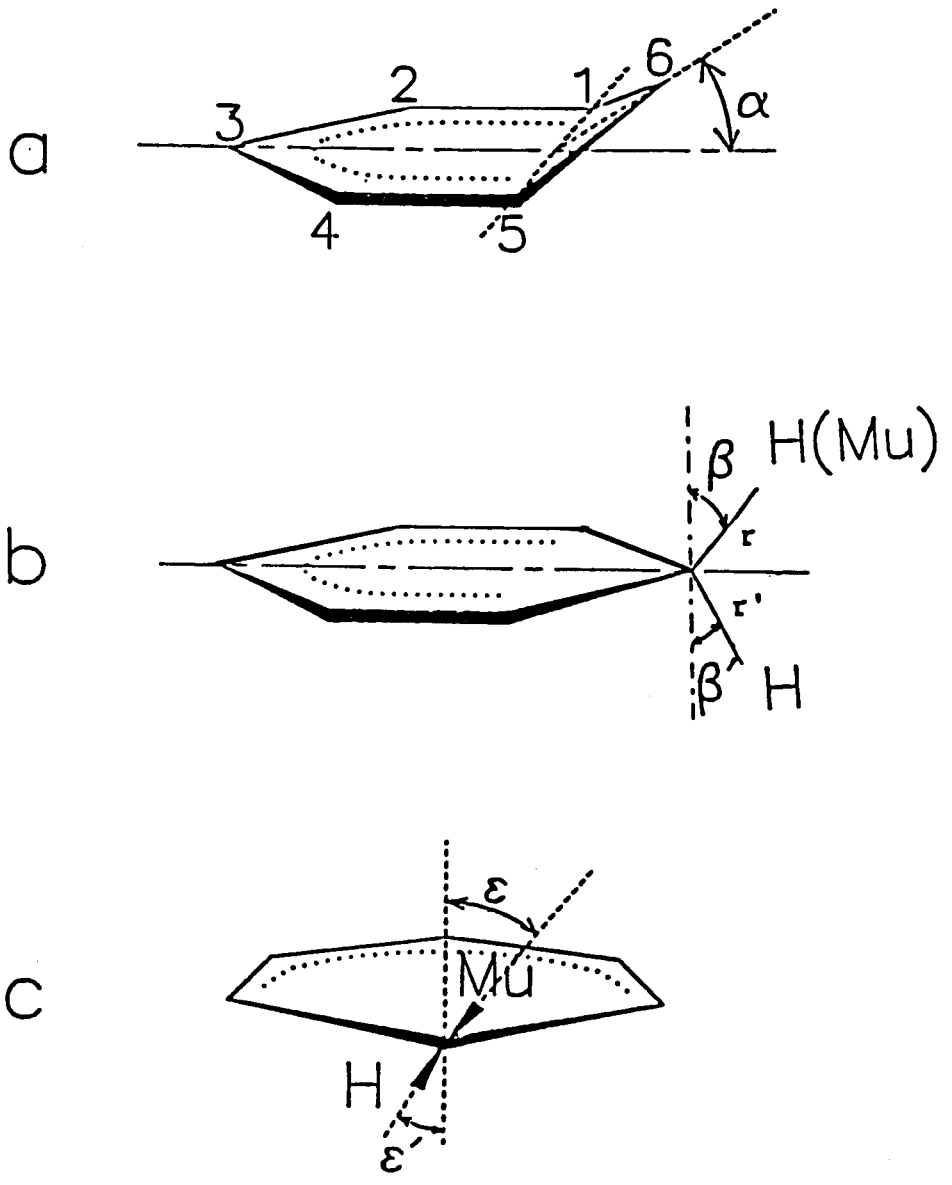

Figure VIII.2. Definition of the ring positions and notation for Mu-substituted cyclohexadienyl radicals.

The muon, methylene proton, methylene deuteron and ^{13}C hfcc of Mu-substituted cyclohexadienyl radicals (deuterated or enriched with ^{13}C where applicable) were measured as a function of temperature. The results are shown in figures VIII.3 and VIII.4. The muon and deuteron coupling constants in figure VIII.3 have been scaled by the appropriate ratio of magnetic moments to make them directly comparable to the proton couplings.

The negative temperature gradients of the hfccs of the muon and the methylene protons/deuterons are taken as evidence for a planar configuration for the C_6H_6Mu and C_6D_6Mu radicals. The spin distribution of unpaired spin density in the planar ring was estimated to be $\rho_1 = \rho_5 = 0.33$, $\rho_2 = \rho_4 = -0.10$, and $\rho_3 = 0.48$. The remaining spin density of 0.06 is located in the antisymmetric methylene group orbital. These results apply to C_6D_6Mu, C_6H_6Mu and C_6H_7. The lack of a significant isotope effect on the spin distribution suggests that the differences in magnitude and temperature gradient of the methylene hfccs are due to local effects only, such as isotope-dependent bond lengths. Semi-empirical calculations (MINDO/3 for geometries and INDO for hfcs) were carried out by Mr. D. Yu [74] to simulate muonium substitution in these radicals. The results indicated that the C−Mu bond is 4.3% larger than the C−H bond for C_6H_6Mu, and 4.9% for C_6D_6Mu. For C_6H_6Mu the optimum β (see figure VIII.2 for definition) was found to be 52.1° for Mu and 48.5° for H; for C_6D_6Mu the corresponding angles are 52.5° and 48.3°.

The same types of MINDO/3 and INDO calculations were carried out for the ^{13}C hfccs to investigate the various types of motions. Out-of-plane bending (increase in α) was found to have the greatest effect on C(1,5), in contradiction to experimental findings. Methylene wagging (increase in β) affects C(6) but not

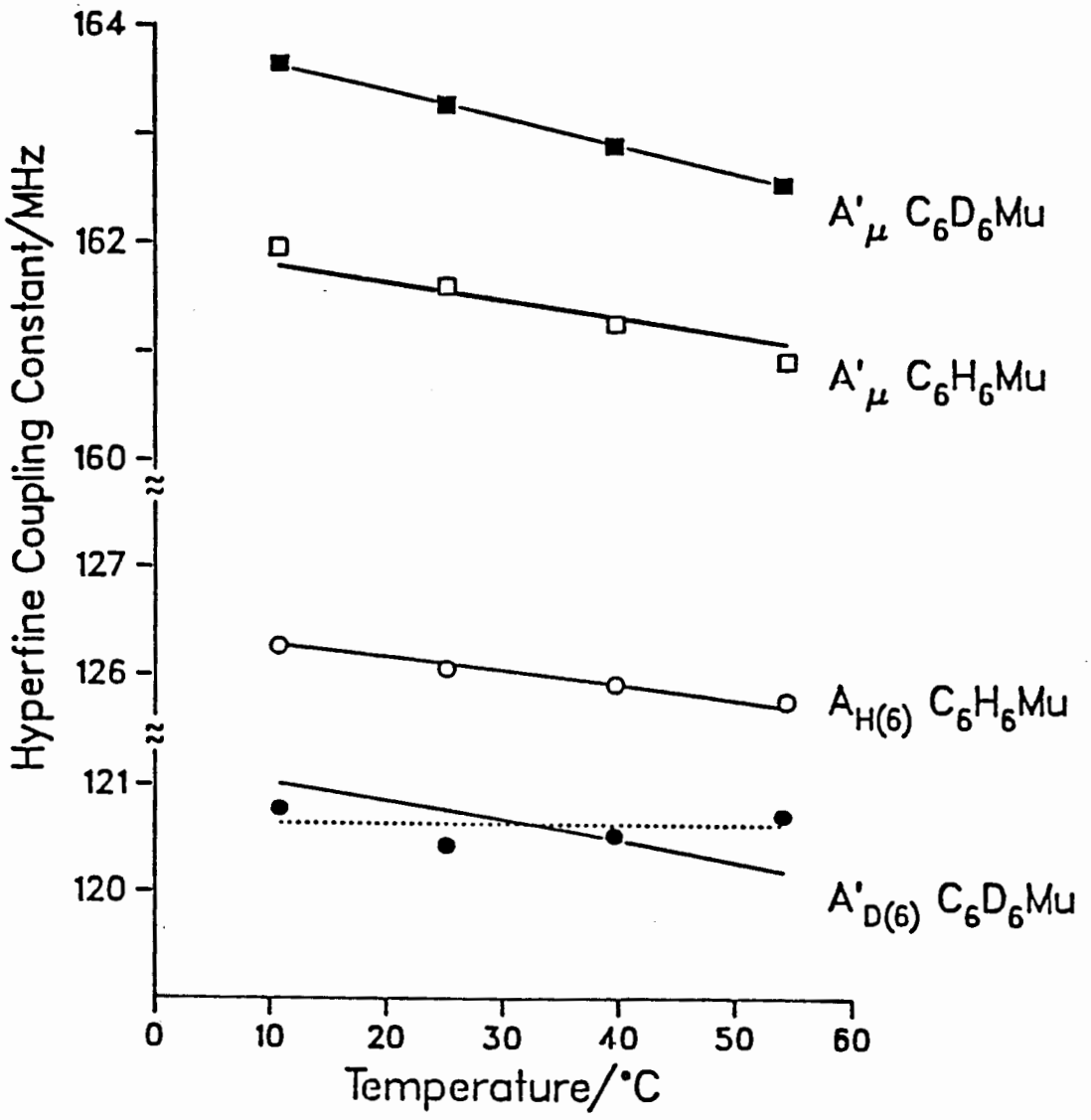

Fig. VIII.3. Temperature dependence of the hyperfine coupling constants for the methylene substituents of C_6H_6Mu and C_6D_6Mu. The muon and deuteron hfcc have been scaled by the appropriate ratio of magnetic moments to make them directly comparable to the proton couplings. Note the broken axis. The solid line through the points represents the best fit of the theoretical model. The dotted line represents the least-squares straight-line fit to the deuteron hfcc.

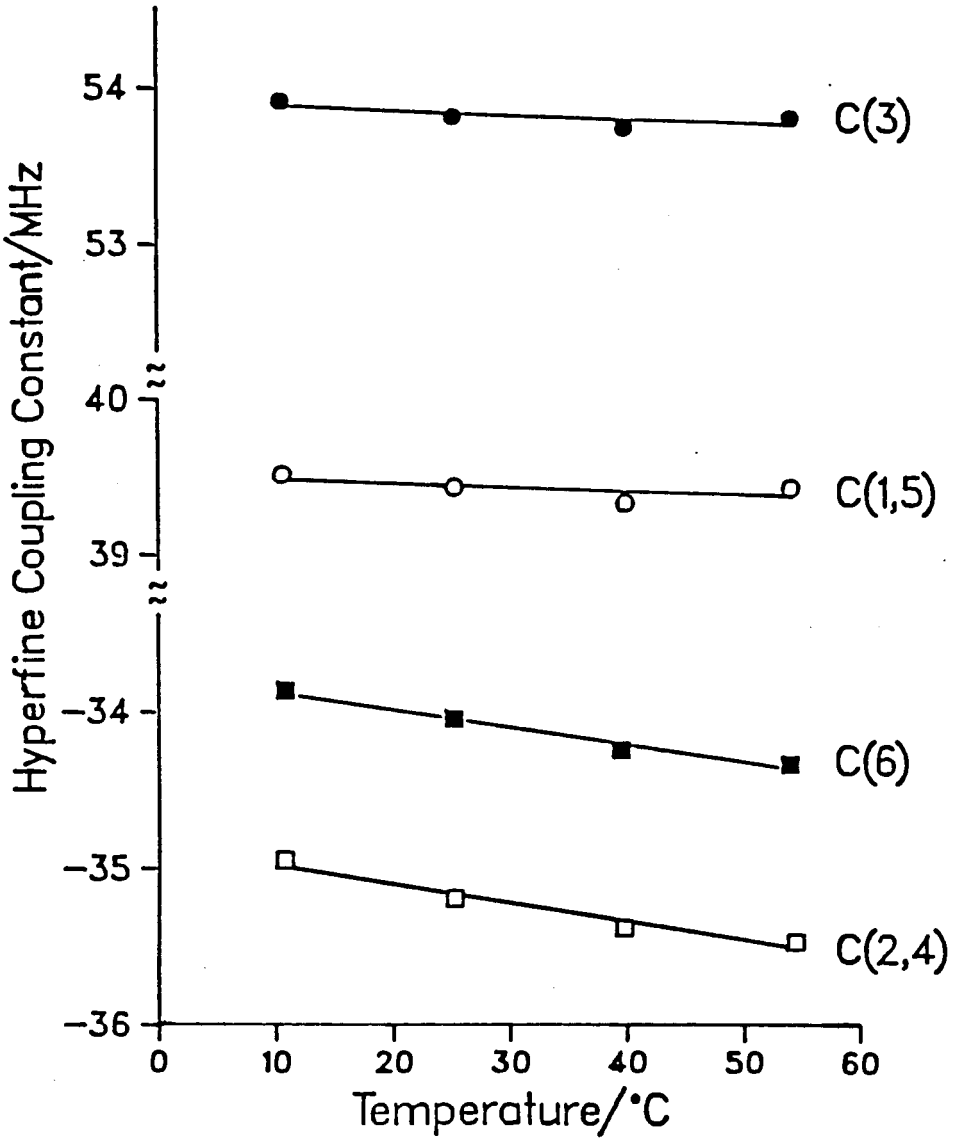

Figure VIII.4. Temperature dependence of ^{13}C hyperfine coupling constants for $^{13}C_6H_6Mu$. The points represent experimental results and the straight lines are the best fits to the experimental data.

C(2,4). Furthermore, the effect on C(6) is in the wrong direction. The motions which result in significant decrease in the C(6) hfc are the methylene C–Mu and C–H stretches and twisting of this group about the C(3)–C(6) axis. The conclusion was that a complete analysis should include all the atoms in the molecule (all 33 normal modes) and that there is no simple way to predict the temperature dependence of the ^{13}C hyperfine coupling constants.

VIII.5. Hyperfine constants for the ethyl radical in the gas phase

Measurements of hyperfine couplings of free radicals in the gas phase are of value in the study of molecular structure and vibrations since they are free of matrix and solvent effects. However, there has been only one previous report of direct μSR detection of a radical in the gas phase, that of the Mu-subsituted ethyl radical CH_2CH_2Mu, in 25–50 atm of ethene [119].

In a collaboration between the SFUMU group and the UBC gas muon chemistry group (Professor D.G. Fleming *et al*) experiments were carried out by conventional μSR and μLCR techniques, including detailed measurements of muon, proton, deuteron, and ^{13}C hyperfine coupling constants in CH_2CH_2Mu, CD_2CD_2Mu and $^{13}CH_2{}^{13}CH_2Mu$ in the gas phase. C_2H_4 was studied at pressures from 1 to 15 atm, C_2D_4 at 12 and 16 atm and $^{13}C_2H_4$ at 2.7 atm. No systematic variation of A_μ and A_p with pressure was found. However, A_μ was found to be temperature dependent. The temperature dependence of the positions of LCR resonances was attributed to the variation of A_μ with temperature. The hyperfine coupling constants for the methyl (β) and methylene (α) protons are tabulated in table VIII.1 along with the muon hyperfine coupling constants.

$\bar{A}$ is the average coupling for the methyl group as defined previously. A_μ' is

Table VIII.1. Muon (A_μ) and proton (A_p) hyperfine coupling constants for the $CH_2\dot{C}H_2Mu$ radical in the gas phase

Temp (°C)	A_μ (MHz)	A'_μ (MHz)	A_p (MHz)	$\bar{A}(CH_2Mu)$ (MHz)
Methyl (β) group				
10.7	333.5	104.8	66.8	79.4
25.3	329.8	103.6	66.8	79.1
37.2	327.2	102.8	67.2	79.0
Methylene (α) group				
10.8	333.4	104.7	−62.9	
24.4	330.0	103.7	−63.4	
37.5	327.2	102.8	−63.0	

considerably larger than A_p, in keeping with the general principle that in the minimum energy conformation the light isotope eclipses the orbital containing the unpaired electron. $\bar{A}(CH_2Mu)$ is significantly larger than the methyl proton hfcc in the unsubstituted radical, $A_p(CH_3)$ = 75.3 MHz [120], confirming the existence of a residual isotope effect (caused by the elongation of the C–Mu bond compared with C–H, a consequence of zero-point motion in an anharmonic potential) as mentioned in the previous two sections.

The deuterium– and ^{13}C–labelled radicals were studied at room temperature only. The results are summarized in table VIII.2. The proton equivalent coupling ($A'_D = 6.514\,A_D$) of the α deuterons is −63.2 MHz, in excellent agreement with the proton value. A'_D for the β deuterons is 63.8 MHz, which combined with A'_μ gives an average hfc for the CD_2Mu group of 78.2 MHz. This is not significantly different from the CH_2Mu value. Again, comparison with $A_p(CH_3)$ shows clear evidence of the residual isotope effect. The α ^{13}C hfc obtained in this experiment is close to that found for CH_2CH_3 in solution by ESR [121,122]. However, detailed comparison can not be made because of the difference in phases.

The μSR detection of the CH_2CH_2Mu radical down to a pressure of 1 atm suggests that a significant fraction of the radical must be formed by some other route than addition of (near) thermal muonium to ethene. This matter remains to be explored in future work.

VIII.6. Muonium formation in C_2H_6 and N_2

Of the collaborative projects mentioned in this chapter, the work described in this section is most pertinent to the main theme of the present thesis. In gases, muonium is formed at epithermal energies during the charge-exchange cycles of μ^+

Table VIII.2. Muon, deuteron, and ^{13}C hyperfine couplings for CD_2CD_2Mu and $^{13}CH_2{}^{13}CH_2Mu$ in the gas phase at room temperature

Radical	Temp. (°C)	A_μ (MHz)	A_D or A_C (MHz)
C_2D_4Mu	22±2	340.3±0.2	9.8±0.3 (β) -9.7±0.5 (α)
$^{13}CH_2CH_2Mu$	21±1	331.5±0.3	113.1±0.3 (β) −38.8±0.3 (α)

with the moderator [35,37,123]. For gases with ionization potentials (IP) greater than 13.6 eV (*e.g.*, for He, Ne, and N_2), the yield of Mu is less than 100% [123]. On the other hand, if the ionization potential for the gas is less than 13.6 eV, charge-exchange is exothermic even at thermal energies, and one would expect a 100% yield of thermalized muonium. This is in fact observed in the case of xenon at low to moderate pressures [124]. In all cases of molecular gases studied to date, an appreciable diamagnetic fraction is observed. In most molecular gases at pressures near 1 atm, values of P_M are typically $\approx$0.8 with $P_D \approx 0.2$ [38]. The situation is markedly different in solutions [3,17]. The mechanism of Mu formation in solutions is described by the spur model [16,76]. The existence of the missing fraction ruled out the simple view of condensed matter being a dense gas. The missing fraction is explained by encounters of Mu with paramagnetic species in the terminal muon spur [76].

The present study is a collaboration between the SFUMU group and the University of British Columbia gas chemistry group (Professor D.G. Fleming *et al*). Muon polarization as a function of pressure in nitrogen and ethane was measured. Ethane was studied at pressures from 1 atm to 250 atm, both above and below the critical temperature, T_c (305.3 K). Results were also obtained for N_2 in a similar pressure range, but only for $T > T_c$ (126 K). These studies are the first to provide systematic data on muon polarization over a wide range of pressure, spanning the regime from an ideal gas, where the hot atom model should be appropriate, to liquid densities, where the spur model has been widely applied.

P_M and P_D for ethane are plotted in figs. VIII.5 and VIII.6 as a function of density (ρ); the sum, P_{tot}, is also included in fig. VIII.6. Different symbols are used to indicate whether the data were obtained below (open points) or above (closed

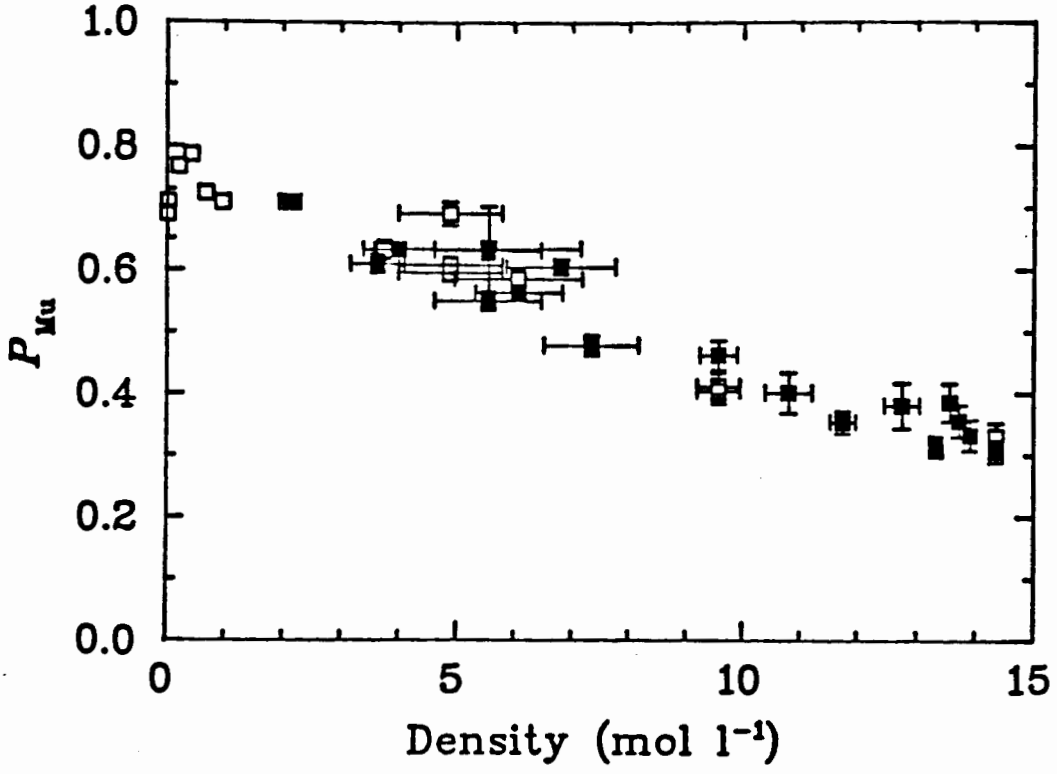

Figure VIII.5. Muonium polarization as a function of density in C_2H_6 above (filled symbols) and below (closed symbols) T_c (305.3 K).

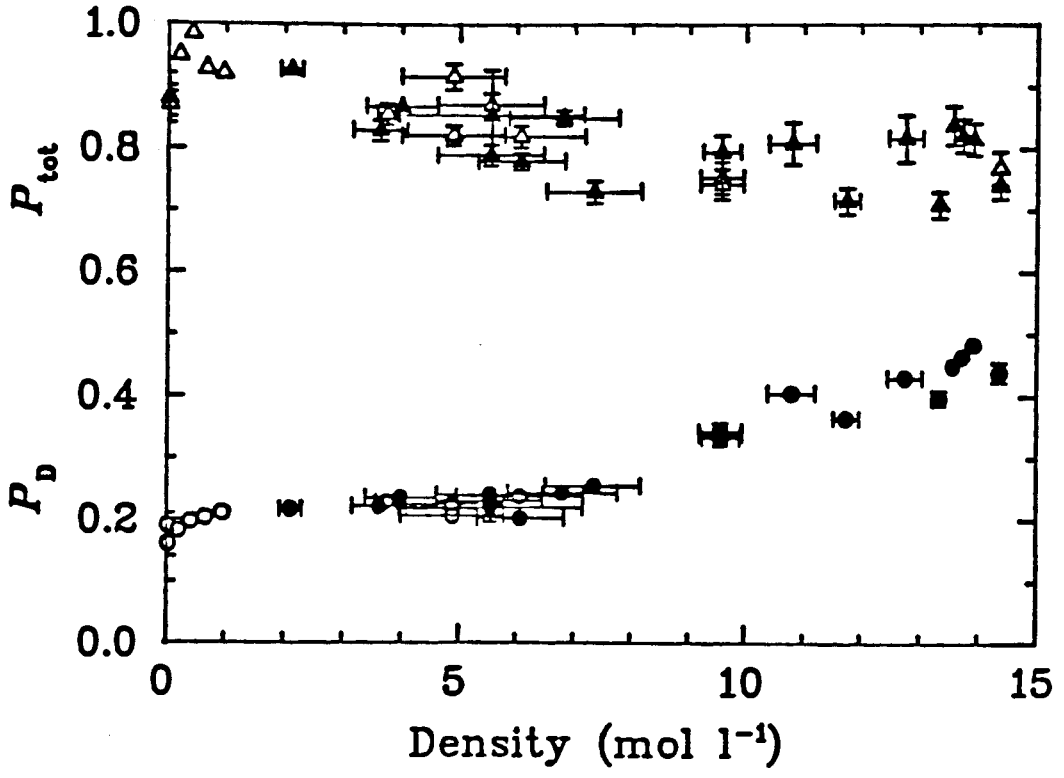

Figure VIII.6. Diamagnetic (circles) and total (triangles) muon polarizations as a function of density in C_2H_6 above (closed symbols) and below (open symbols) T_c.

points) T_c. The N_2 data were obtained at room temperature ($\approx$ 22 °C), where N_2 behaves as an ideal gas over the pressure range studied. The polarizations P_M and P_D are plotted vs. pressure in figs. VIII.7 and VIII.8, respectively. P_{tot} is also included in fig. VIII.8.

For N_2 in figure VIII.8, P_{tot} is unity (*i.e.* no missing fraction) at P $\approx$ 2 atm and p > 100 atm, while there is a considerable lost fraction at low and intermediate pressures (p < 1 atm and 3 < p < 100 atm). In contrast, the C_2H_6 data in figure VIII.6 show that even at high pressures there is is still an appreciable missing fraction ($P_L \approx 0.2$). Furthermore, P_D in N_2 steadily approaches zero at high pressure from its maximum of 0.18 at 1.5 atm; concomitantly, the muonium polarization approaches unity. This is to be compared with the increase in P_D with increasing density (pressure) with a corresponding decrease in P_M.

In the hot atom model, the two properties of the moderator that are expected to have the largest effect on the distribution of muon polarization are the ionization potential (IP) and the bond energy (BE), both of which are significantly higher in N_2 (IP = 15.6 eV, BE = 9.8 eV [125]) than in C_2H_6 (IP = 11.5 eV, BE = 4.2 eV [125]). Since the IP of N_2 is also considerably higher than that of Mu itself (13.5 eV), Mu can only form at epithermal energies down to 2.1 eV (the difference between the ionization potentials for N_2 and Mu). The muonium fraction is estimated to be 0.85, which agrees with the experimental values up to about 10 atm. The particularly strong bond in N_2 mitigates against hot atom reactivity as the Mu^* thermalizes below the cyclic charge exchange regime (on the order of 10 eV). In analogy with related studies in He and Ne [126], the diamagnetic signal in N_2 is attributed to N_2Mu^+ molecular ions. This is supported by the observation of rapid relaxation of the diamagnetic μSR signal in low pressure N_2 to which trace amounts

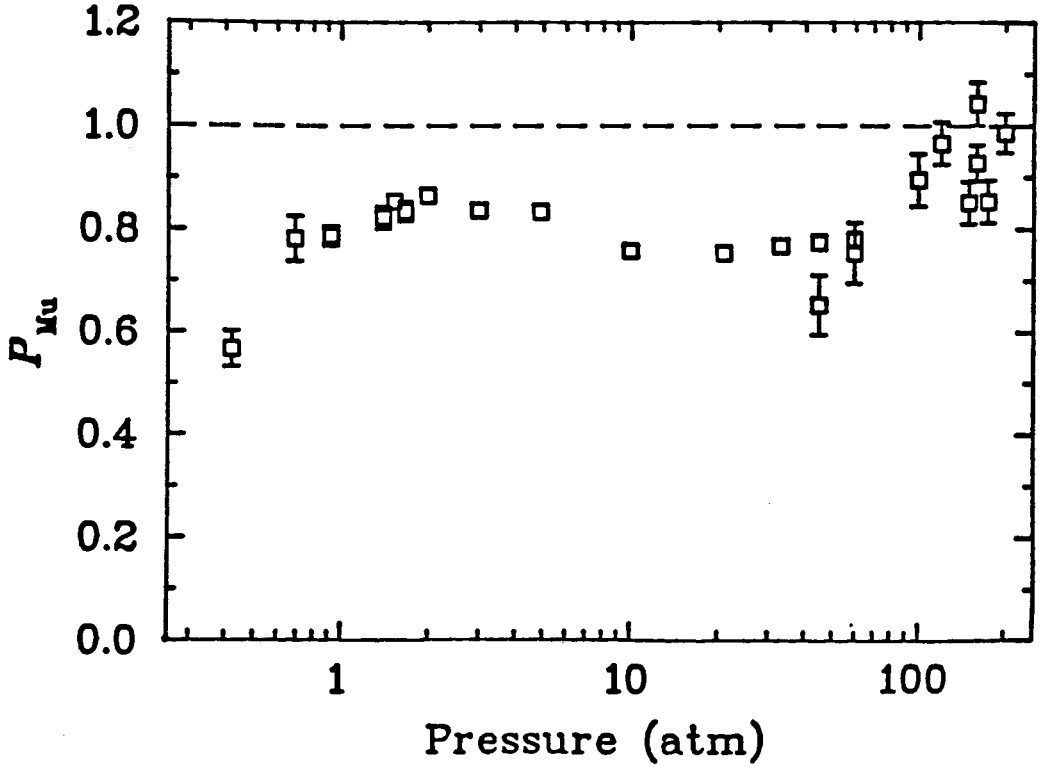

Figure VIII.7. Muonium polarization as a function of pressure in N_2.

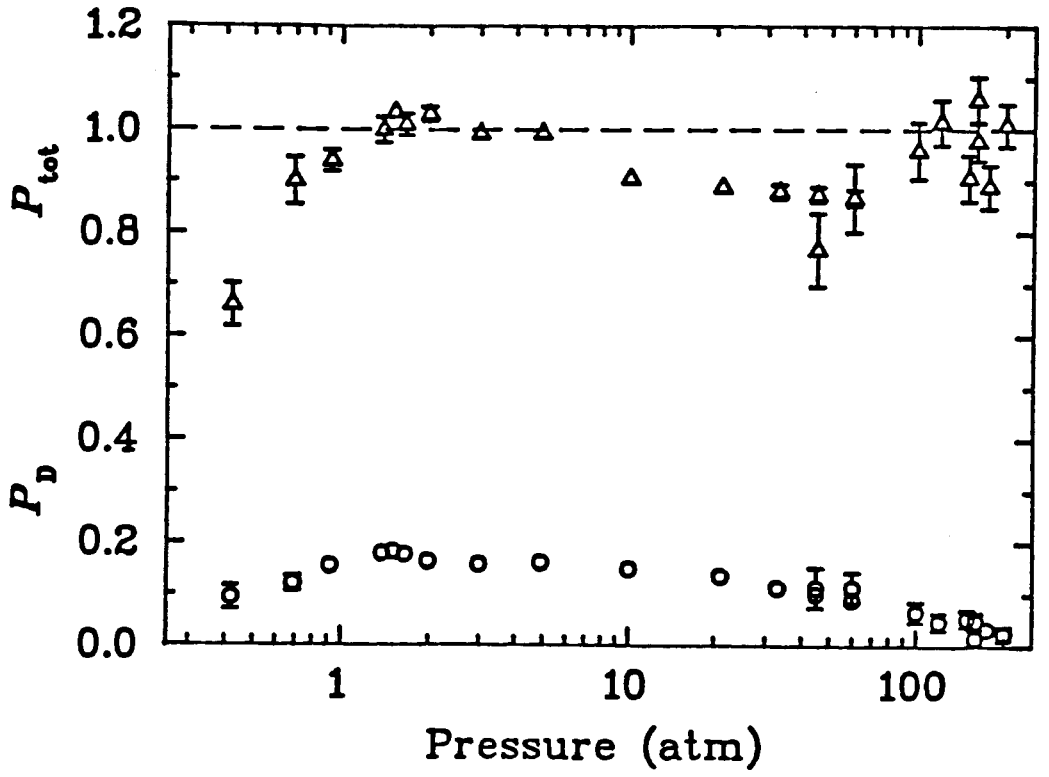

Figure VIII.8. Diamagnetic (circles) and total (triangles) muon polarizations as a function of pressure in N_2.

of dopants (*e.g.*, NO) have been added [126].

While epithermal charge exchange and μ^+ capture account for the data at low pressures, the spur model provides the most natural explanation for the distribution of muon polarization seen in N_2 at pressures above 10 atm. The decrease of the diamagnetic signal to zero at pressures above 150 atm is completely inconsistent with epithermal charge exchange from which the diamagnetic fraction would be expected to either increase (due to the stabilization of N_2Mu^+) or stay constant with increasing pressure. The increase in the missing fraction from its value of zero at 1.5 atm to its maximum of $\approx$ 0.13 near 50 atm is attributed to spin exchange with paramagnetic species in the spur, and is consistent with the spur model. The recovery of P_{tot} to unity at still higher pressures is possibly the result of combination of N_2^+ and e^- in the spur, facilitated by the decreased mobility of the e^- at the higher pressures. Indeed, both N_2^+ and e^- are paramagnetic species, both contributing to P_L in N_2 at lower pressures.

In contrast to N_2, the weaker C–H bond (4.2 eV [125]) in C_2H_6 facilitates hot atom reactions, reducing the muonium prompt fraction from one, and concomitantly increasing the diamagnetic fraction. The diamagnetic fraction at low pressures in C_2H_6 is thought to be predominantly due to MuH formed in abstraction reactions [38]. The increase in diamagnetic fraction below 40 atm (3 mol l^{-1} density) is explained within the hot atom model in terms of collisional stabilization of vibrationally excited substitution products, RMu^*. A contribution from hot abstraction reactions is also required to explain the nonzero diamagnetic fraction at zero density. The increase in the diamagnetic fraction with density above 3 mol l^{-1} is difficult to reconcile with the hot atom model. The spur model provides a more natural explanation in terms of competition between charge neutralization, forming

Mu, and proton transfer from $C_2H_6Mu^+$, forming a diamagnetic product. Significant factors in this competition include electron mobility and the distribution of radiolysis products in the neighborhood of the muon.

For both N_2 and C_2H_6, the missing fraction is most likely due to spin exchange of Mu with paramagnetic species in the terminal spur. The possibility that hot atom reactions could account for the results is remote, particularly in N_2. In this case, recovery of the polarization at high pressures is ascribed to the combination of N_2^+ ions with e^- in the spur. For C_2H_6, P_L is about twice as large as for N_2, and is essentially constant for densities beyond 5 M ($\approx$ 50 atm). Both the larger value for P_L and its persistence at higher densities in C_2H_6 can be understood in terms of interactions with alkyl radicals and H atoms in the spur, in addition to e^-. The former species persist chemically under conditions where the electrons are scavenged by positive ions.

VIII.7. Capto-dative effects in Mu-substituted cyclohexadienyl radicals

The hfcc for unsubstituted cyclohexadienyl is 514.5 MHz [127]. The hyperfine coupling constants of the methylene proton/muon for the two Mu-substituted trihydroxy-cyclohexadienyls were measured to be 470.7 MHz and 481.1 MHz (see Section VII.2). The shift in hfcc from the unsubstituted radical could be due to "capto-dative" stabilization in free radical chemistry [128,129]. This effect is described as the combined action of an electron-withdrawing (*captor*) and an electron-releasing (*donor*) substituent on a radical center leading to an additional stabilization in addition to the sum of their individual effects (*synergetic*). On the other hand, the combined effect of identical substituents (*i.e.* either both electron-withdrawing or donating) is less than the sum of their individual effects

(*antagonistic*).

This set of experiments was designed to test the antagonistic effect. High transverse-field μSR and LCR spectra were obtained for di–hydroxybenzenes (resorcinol, catechol, and hydroquinone) (the expected products are given in figure VIII.9). When both radical frequencies were observed in the μSR spectrum, the muon coupling constant was calculated simply by taking the difference between the two frequencies (see equation II.14). When ν^+ was too high to be observed, the muon hfcc was calculated using equation VII.3. The results are collected in table VIII.3. Three, two, and one pair of radical frequencies were detected for resorcinol, catechol, and hydroquinone, respectively. The calculated hfccs are also included in table VIII.3. LCR resonances for the methylene protons for all except the 2,4–dihydroxycyclohexadienyl were observed. The LCR resonance positions and amplitudes were extracted from the fits. The methylene proton hfcc (A_p) were calculated from eq. (VI.1). The results, along with the resonance fields, are given in table VIII.4.

The reasoning for the assignment of the radicals given in table VIII.3 is as follows. The values of A_μ of the radicals were compared to the muon hyperfine coupling constants for the 1–, 2–, and 3–hydroxycyclohexadienyls (formed when Mu adds to phenol) (467.4, 517.4, and 493.0 MHz, respectively [127]). The adduct with a substituent at the *meta* position is expected to have a muon hfcc close to that of unsubstituted cyclohexadienyl (radical IV).[1] Furthermore, A_μ of an adduct having an *ortho*-substituent is expected to be shifted to a lower frequency (compare 1–hydroxycyclohexadienyl to 3–hydroxycyclohexadienyl). By the same analogy, the

[1] *Meta* substituents in cyclohexadienyls have little effect on A_μ since the molecular orbital containing the unpaired electron has a node in that position.

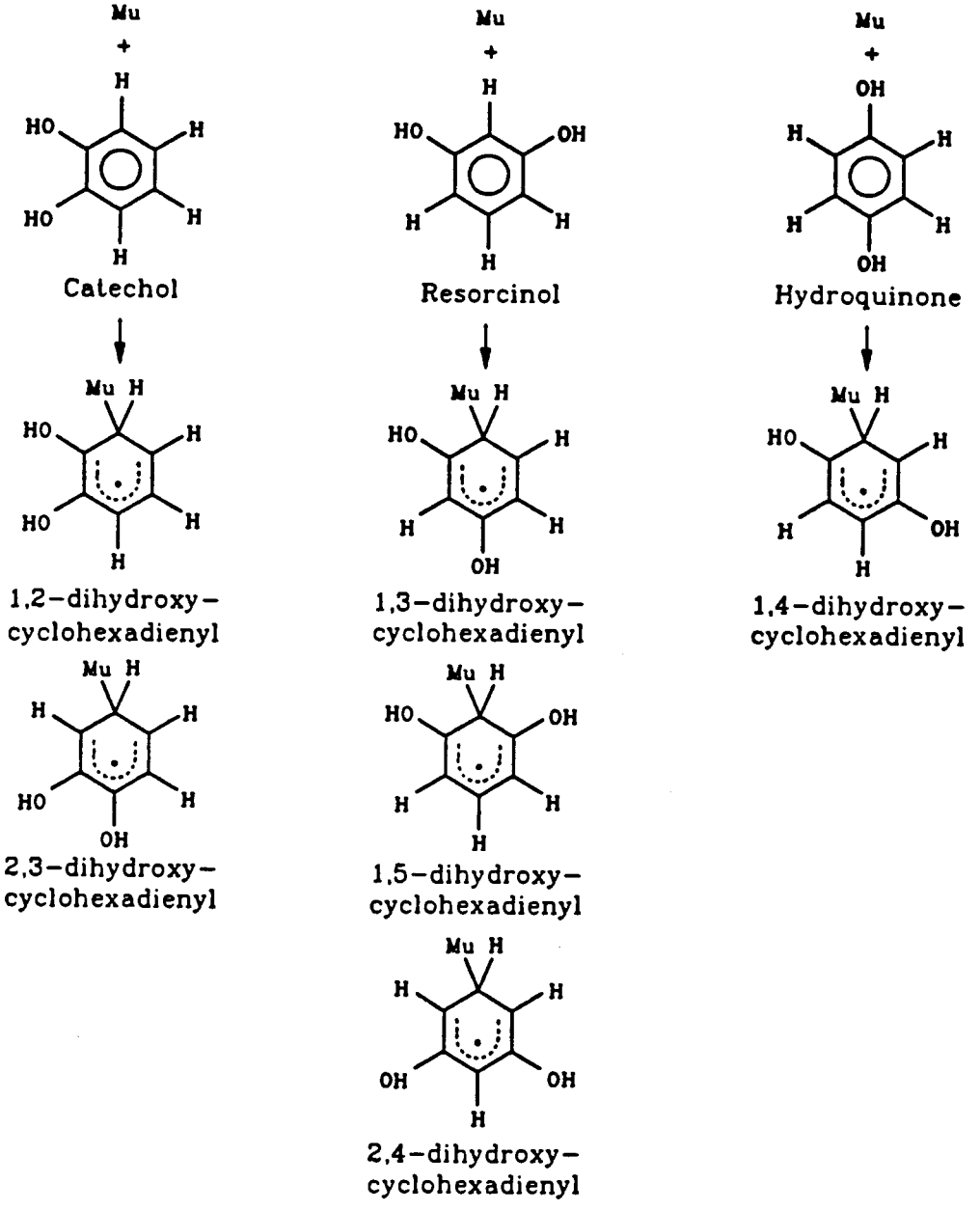

Figure VIII.9. Radicals formed by addition of Mu to catechol, resorcinol, and hydroquinone.

Table VIII.3. Experimental values of ν^+, ν^- and ν^μ for some hydroxy-substituted cyclohexadienyl radicals. The calculated values of A_μ are also included.

Sample	ν^+ (MHz)	ν^- (MHz)	ν^μ (MHz)	A_μ (MHz)	Assign-ment
Di-hydroxycyclohexadienyls					
Catechol	339.1(8)	143.4 (3)	94.94(2)	482.6(1)	1,2
Resorcinol	316.5(1)	121.79(5)	94.94(2)	438.3(4)	1,5
Hydroquinone		155.58(2)	64.87(2)	448.3(1)	1,4
Resorcinol	328.1(1)	132.92(4)	94.94(2)	461.0(1)	1,3
Catechol		144.9 (3)	94.94(2)	485.7(1)	2,3
Resorcinol		165.56(7)	94.94(2)	528.1(3)	2,4
Tri-hydroxycyclohexadienyls					
Pyrogallol		165.94(4)	65.34(1)	470.7(1)	1,2,3
Pyrogallol		44.03(8)	195.27(1)	481.5(6)	2,3,4

Number in brackets = uncertainty in final digit.

Table VIII.4. A_μ, A_p, and B_0 for some hydroxy-substituted cyclohexadienyls

Positions of substituents	A_μ [a] (MHz)	B_0 [a] (G)	A_p [a] (MHz)	$(A_\mu/A_p)/(\gamma_\mu/\gamma_p)$
	Di-hydroxycyclohexadienyls			
1,2	482.5 (1)	19343(1)	120.9 (3)	1.26
1,3	461.02(3)	18664(2)	112.11(1)	1.29
1,4	448.3 (1)	18019(1)	112.19(3)	1.26
1,5	438.3 (4)	17481(2)	111.47(1)	1.241
2,3	485.7 (1)	19708(2)	117.3 (3)	1.30
2,4	528.1 (3)	[b]		
	Tri-hydroxycyclohexadienyls			
1,2,3	470.7 (1)		115.5 (1)	1.28
2,3,4	481.1 (1)		119.6 (1)	

[a] Number in brackets = uncertainty in final digit.
[b] Radical not resolved in μLCR spectrum.

lowest A_p were assigned to radicals containing the most number of *ortho* hydroxy groups while the highest were those with the most number of *meta* substituents.

ESR studies of substituted benzyl radicals indicated that the "capto-dative" effect exists [129,130]. The following equation defines a fractional shift in hfcc of a mono-substituted radical from the unsubstituted radical:

$$\Delta_x = 1 - A_x/A_0 \qquad \text{(VIII.6)}$$

where A_x is the hfcc of the substituted radical and A_0 is for the unsubstituted radical. If the substituent effects are purely cumulative, then the following equation should predict the muon hyperfine coupling constants of di-substituted cyclohexadienyl radicals:

$$A_\mu = A_\mu^0 (1 - \Delta_{x1}) (1 - \Delta_{x2}) \qquad \text{(VIII.7)}$$

where A_μ^0 is the coupling for the unsubstituted cyclohexadienyl. However, a recent μSR study by Rhodes and Roduner on di-substituted cyclohexadienyl radicals showed that with the addition of a substituent interaction parameter to equation (VIII.7), *i.e.*

$$A_\mu = A_\mu^0 (1 - \Delta_x) \cdot (1 - \Delta_y) \cdot (1 - \Delta_{xy}) \qquad \text{(VIII.8),}$$

or more generally,

$$A_\mu = A_\mu^0 \Pi(1 - \Delta_x) \Pi(1 - \Delta_{xy}) \qquad \text{(VIII.9),}$$

they found better agreement with their experimental data [131]. If Δ_{xy} is positive, the combined effect of the substituents are more than cumulative (synergetic). If Δ_{xy} is negative, then the interaction is antagonistic.

The values of Δ_x (from Mu addition to phenol) were calculated and the results were used to estimate A_μ for the di-hydroxycyclohexadienyls using equation (VIII.7) (A_μ^0 from neat benzene). The results are given in table VIII.5. It is evident that the calculated A_μ do not agree well with experimental results. Therefore, the values of Δ_{xy} in equation (VII.8) were calculated and were used to calculate A_μ for the trihydroxycyclohexadienyls. The results can also be found in table VIII.5. The calculated values of A_μ for the trihydroxycyclohexadienyl radicals agree reasonably well with experiment (the discrepancies are less than 1%).

For comparison purposes, the values of Δ_{xy} from previous works [131,132] are given in table VIII.6 along with those obtained in this work. Our result roughly follow the trend of their data. The scattering of the signs of Δ_{xy}, especially when one or both of the substituents occupies a *meta* position, indicate that other substituent effects may also operate. These include polar effects and inductive destabilization (with electron withdrawing substituents) [133-135]. It seems that this procedure can only give rough predictions, at best, for combined effects of substituents on the stablization of radicals. Further discussion of this topic will have to wait until more data is available.

Table VIII.5. Calculated values of A_μ, Δ_x, and Δ_{xy} for some hydroxy-substituted cyclohexadienyl radicals

Substituent position	Experimental A_μ (MHz)	Δ_x	Calculated A_μ from eq. (VIII.7) (MHz)[a]	Δ_{xy}	Calculated A_μ from eq. (VIII.8) (MHz)[a]
1	467.4[b]	0.0915			
2	517.4[b]	-0.0057			
3	493.0[b]	0.0418			
1,2	482.6		470.1	-0.0267	
1,3	461.1		447.9	-0.0296	
1,4	448.4		470.1	0.0461	
1,5	438.3		424.6	-0.0322	
2,3	485.7		495.8	0.0203	
2,4	528.1		520.4	-0.0149	
1,2,3	470.7		450.4		466.47
2,3,4	481.5		498.6		485.70

[a] A_μ^0 used is 514.48 MHz.
[b] Data are from reference [127].

Table VIII.6. Values of Δ_{xy} for the interaction of two substituents in the cyclohexadienyl radical (in units of 100 Δ_{xy})

Substituent positions	Substituents			
	Me[a]	F[a]	OMe[a]	OH[b]
1,2	-1.81	-1.62	-7.07	-2.65
1,3	-0.45	-0.71	-3.37	-2.93
1,4	+0.36	+1.12	+4.44	+4.62
1,5	-0.13	-1.93	-2.62	-3.23
2,3	-0.99	+1.53	-2.53	+2.03
2,4	+0.01	-0.90	-1.45	-1.48

[a] Data from reference [132,133].
[b] This work.

CHAPTER IX. SUMMARY

The aim of this thesis was to characterize the time-scale of the spur process which leads to the missing fraction of the initial muon polarization in aqueous solutions. This has been done in two different ways using both the conventional μSR and the μLCR techniques. Firstly, the diamagnetic muon polarization in pure water was measured as a function of applied field using conventional μSR. A small field dependence of P_D was found. This dependence arises from MuH formed in the spin-selective reaction of Mu with e^-_{aq}. In competition with chemical reaction is spin exchange, which leads to the muon spin depolarization manifest as the missing fraction. From results of scavenger experiments, the interaction between Mu and e^-_{aq} was determined to occur on a nanaosecond time-scale. This interaction is quite distinct from the competition between muon hydration and muonium formation which occurs at much shorter times.

Secondly, the addition of muonium to pyrogallol in aqueous solution was studied by means of the μLCR technique. The concentration dependence of the radical amplitudes in low concentration of solutes is explained by homogeneous kinetics of muonium addition to pyrogallol. The radical formation rate constant was found to be 7.4×10^9 M^{-1} s^{-1}, in agreement with results obtained by conventional μSR. At higher solute concentrations, formation of trihydroxycyclohexadienyl radicals is in competition with the development of the missing fraction. The characteristic time for the encounter between Mu and hydrated electrons was estimated to be about 3 nanosecond. This time is in good agreement with estimates from the pure water study using the μSR technique.

Thus, in conclusion, the missing fraction of the muon polarization in aqueous solutions is a result of interactions between Mu and e^-_{aq} on a nanosecond time-scale. Contrary to previous belief, muonium also undergoes chemical reaction with hydrated electrons to form MuH.

REFERENCES

1. S.H. Neddermeyer and C.D. Anderson, Phys. Rev. 54 (1938) 88.

2. E. Gardner and C.M.G. Lattes, Science 107 (1948) 270.

3. A. Schenck, "Muon Spin Rotation Spectroscopy" (Adam Hilger, Bristol, 1985).

4. D.C. Walker, "Muon and Muonium Chemistry" (Cambridge University Press, Cambridge, 1983).

5. J. Chappert and R.I. Grynszpan, eds., "Muons and Pions in Materials Research" (North-Holland, Amsterdam, 1984).

6. B. Webster, Ann. Rept. Progr. Chem. C 81 (1984) 3.

7. P.W. Percival, .B. Brodovitch and K.E. Newman, Faraday Discussions Chem. Soc. 78 (1984) 315.

8. S.F.J. Cox, J. Phys. C 20 (1987) 3187.

9. J.I. Friedman and V.L. Telegdi, Phys. Rev. 105 (1957) 1681.

10. V.W. Hughes, D.W. McColm, K. Ziock and R. Prepost, Phys. Rev. Lett. 5 (1960) 63.

11. D.G. Fleming, D.M. Garner, L.C. Vaz, D.C. Walker, J.H. Brewer and K.M. Crowe, Adv. in Chemistry Series 175 (1979) 279.

12. A. Abragam, *C.R. Acad. Sc. Paris, Serie II* 299 (1984) 95.

13. R.F. Kiefl, S. Kreitzman, M. Cello, R. Kietel, G.M. Luke, J.H. Brewer, D.R. Noakes, P.W. Percival, T. Matsuzaki and K. Nishiyama, Phys. Rev. A 34 (1986) 681.

14. M. Heming, E. Roduner, B.D. Patterson, W. Odermatt, J. Schneider, H. Baumeler, H. Keller and I.M. Savic, Chem. Phys. Letters 128 (1986) 100.

15. P.W. Percival, H. Fischer, M. Camani, F.N. Gygax, W. Rüegg, A. Schenck, H. Schilling and H. Graaf, Chem. Phys. Lett. 39 (1976) 333.

16. P.W. Percival, E. Roduner and H. Fischer, Chem. Phys. 32 (1978) 353.

17. P.W. Percival, *Radiochimica Acta* 26 (1979) 1.

18. P.W. Percival, K.M. Adamson-Sharpe, J.C. Brodovitch, S.K. Leung and K.E. Newman, Chem. Phys. 95 (1985) 321.

19. R.F. Kiefl, J.B. Warren, G.M. Marshall, C.J. Oram and C.W. Clawson, J. Chem. Phys. 74 (1981) 308.

20. Y. Ito, Y, Miyake, Y. Tabata, K. Nishiyama and K. Nagamine, Chem. Phys. Lett. 93 (1982) 361.

21. Y. Miyake, Y. Tabata, Y. Ito, K. Nishiyama and K. Nagamine, Rad. Phys. Chem. 28 (1986) 99.

22. Y. Morozumi, K. Nishiyama and K. Nagamine, Phy. Lett. A 118 (1986) 93.

23. P.W. Percival, J.C. Brodovitch and K.E. Newman, NBS Special Publication 716 (NBS, Washington, 1986), p.547.

24. B.W. Ng, M.Sc. Thesis, University of British Columbia (1980).

25. V.W. Hughes, Bull. Am. Phys. Soc. II 2 (1957) 205.

26. R.L. Garwin, L.M. Lederman and M. Weinrich, Phys. Rev. 105 (1957) 1415.

27. J.H. Brewer, K.M Crowe, F.N. Gygax and A.Schenck, in "Muon Physics" vol. 3, ed. V.W. Hughes and C.S. Wu, (Academic Press, 1975).

28. E. Roduner and H. Fischer, Chem. Phys. 54 (1981) 261.

29. J.H. Brewer, D.G. Fleming and P.W. Percival, in "Fourier, Hadamard, and Hilbert Transforms in Chemistry", ed. A.G. Marshall, (Plenum Publishing Corp. 1982).

30. I.G. Draganic and Z.D. Draganic, "The Radiation Chemistry of water" (Academic Press, New York, 1971).

31. H.A. Bethe and J. Ashkin, in "Experimental Nuclear Physics" vol. 1, ed. E. Segré, (Wiley, New York, 1953), p. 166.

32. "Radiation Chemistry. Principles and Applications", ed. Farhataziz and M.A.J. Rodgers (VCH Publishers, New York, 1987).

33. A.H. Samuel and J.L. Magee, J. Chem. Phys. 21 (1953) 1080.

34. J.W.T. Spinks and R.J. Woods, "An Introduction to Radiation Chemistry" (Wiley and Sons, New York, 1964).

35. D.G. Fleming, R.J. Mikula and D.M. Garner, Phys. Rev. 26A (1982) 2527.

36. D.G. Fleming, D.J. Arseneau, D.M. Garner, M. Senba and R. Mikula, Hyperfine Interactions 17-19 (1984) 655.

37. D.G. Fleming, Rad. Phys. and Chem. 28 (1986) 115.

38. D.G. Fleming, M. Senba, D.J. Arseneau, I.D. Reid and D.M. Garner, Can. J. Chem. 64 (1986) 57.

39. D.G. Fleming, L.Y. Lee, M. Senba, D.J. Arseneau, I.D. Reid and D.M. Garner, *Radiochimica Acta* 43 (1988) 98.

40. O.E. Mögensen, J. Chem. Phys. 60 (1974) 988.

41. O.E. Mögensen and P.W. Percival, Radiat. Phys. Chem. 28 (1986) 85.

42. F.M. Jacobsen, Hyperfine Interactions 31-32 (1986) 501.

43. P.W. Percival, Hyperfine Interactions 8 (1981) 325.

44. P.W. Percival, J.C. Brodovitch and K.E. Newman, Chem. Phys. Letters 91 (1982) 1.

45. J.L Beveridge, J. Doornbos and D.M. Garner, Hyperfine Interactions 32 (1986) 907.

46. F. James and M. Roos, MINUIT, CERN computer, 7600 Interim Program Library (1971).

47. P.W. Percival and H. Fischer, Chem. Phys. 16 (1976) 89.

48. K.E. Newman, J.C. Brodovitch and P.W. Percival, Chem. Phys. Lett. 113 (1985) 347.

49. Y. Miyake, Y. Ito, Y. Tabata and D.C. Walker, Hyperfine Interactions 32 (1986) 825.

50. S.K. Leung, M.Sc. Thesis, Simon Fraser University (1985).

51. J.C. Brodovitch, S.K. Leung, P.W. Percival, D. Yu and K.E. Newman, Rad. Phys. Chem 32 (1988) 105.

52. M. Anbar, Farhataziz and A.B. Ross, "Selected Specific Rates of Reactions of Transients from Water in Aqueous Solutions. Vol. 2 Hydrogen Atom" NSRDS-NBS 51 (US Government Printing Office, Washington, 1975).

53. Y. Miyake, Y. Tabata, Y. Ito, K. Ishida, T. Matsuzaki, K. Nishiyama, K. Nagamine, K.M. Crowe and J.H. Brewer, Hyperfine Interactions 17-19 (1984) 807.

54. K. Ishida, T. Matsuzaki, K. Nishiyama, K. Nagamine, Y. Miyake, Y. Tabata and Y. Ito, Hyperfine Interactions 17-19 (1984) 933.

55. K.E. Newman, K.M. Adamson-Sharpe, J.C. Brodovitch and P.W. Percival, Hyperfine Interactions 17-19 (1984) 709.

56. K.E. Newman, J.C. Brodovitch and P.W. Percival, Chem. Phys. Letters 124 (1986) 279.

57. E. Klempt, R. Schulze, H. Wolf, M. Camani, F.N. Gygax, W. Rüegg, A. Schenck and H. Schilling, Phys. Rev. D25 (1982) 652.

58. K. Nishiyama, T. Azuma, K. Ishida, T. Matsuzake, J. Imazato, T. Yamazaki and K. Nagamine, Hyperfine Interactions 32 (1986) 887.

59. A.D. Trifunac, T.M. Chiu and R.G. Lawler, J. Phys. Chem. 90 (1986) 1871.

60. P.W. Percival, Hyperfine Interactions 8 (1981) 315.

61. G.G. Myasishcheva, Yu.V. Obukhov, V.S. Roganov and V.G. Firsov, *Khim. Vys. Energ.* 1 (1967) 387 (English translation: High Energy Chem. 1 (1967) 337).

62. B. Brocklehurst, Faraday Discussions Chem. Soc. 78 (1984) 303.

63. B. Brocklehurst, Chem. Phys. Letters 143 (1988) 59.

64. D. Eisenberg and W. Kauzmann, "The Structure and Properties of Water" (Oxford University Press, Oxford, 1969).

65. B. Brocklehurst and D.B. Cook, Chem. Phys. Letters 143 (1987) 329.

66. P.W. Percival, Hyperfine Interactions 6 (1979) 373.

67. Farhataziz and A.B. Ross, "Selected Specific Rates of Reactions of Transients From Water in Aqueous Solutions. III. Hydroxyl Radical and Perhydroxyl Radical and Their Radical Ions" NSRDS-NBS 59, (US Government Printing Office, Washington, 1977).

68. T.G. Eck, L.L. Foldy amd H. Wielder, Phys. Rev. Letters 10 (1963) 239.

69. D.T. Edmonds, Phys. Report 29C (1977) 233.

70. S.R. Kreitzman, J.H. Brewer, D.R. Harshman, R. Keitel, D.L. Williams, K.M. Crowe and E.J. Ansaldo, Phys. Rev. Letters 56 (1986) 181.

71. M. Heming, E. Roduner and B.D. Patterson, Hyperfine Interactions 32 (1986) 727.

72. R.F. Kiefl, Hyperfine Interactions 32 (1986) 707.

73. P.W. Percival, J.C. Brodovitch, S.K. Leung, D. Yu, R.F. Kiefl, G.M. Luke, K. Venkateswaran and S.F.J. Cox, Chem. Phys. 127 (1988) 137.

74. D. Yu, Ph.D. Thesis, Simon Fraser University (1990).

75. D. Yu, P.W. Percival, J.C. Brodovitch, S.K. Leung, R. Kiefl, K. Venkateswaran and S.F.J. Cox, Chem. Phys. 142 (1990) 229.

76. S.K. Leung, J.C. Brodovitch, P.W. Percival, D. Yu and K.E. Newman, Chem. Phys. 121 (1988) 393.

77. E. Roduner, "The Positive Muon as a Probe of Free Radical Chemistry" (Springer-Verlag, Berlin, 1988).

78. P.W.F. Louwrier, G.A. Brinkman and E. Roduner, Hyperfine Interactions 32 (1986) 831.

79. Y.C. Jean, J.H. Brewer, D.G. Fleming, D.M. Garner, R.J. Mikula, L.C. Vaz and D.C. Walker, Chem. Phys. Letters 57 (1978) 293.

80. P.W. Percival, R.F. Kiefl, S.R. Kreitzman, D.M. Garner, S.F.J. Cox, G.M. Luke, J.H. Brewer, K. Nishiyama and K. Venkateswaran, Chem. Phys. Letters 133 (1987) 465.

81. C.J. Rhodes and M.C.R. Symons, J. Chem. Soc., Faraday Trans. 1. 84 (1988) 1187.

82. M. Heming, E. Roduner, I. Reid, P.W.F. Louwrier, J.W. Schneider, H. Keller, W. Odermatt, B.D. Patterson, H. Simmler, B. Pümpin, and I.M. Savic, Chem. Phys. 129 (1989) 335.

83. K. Venkateswaran, M.V. Barnabas, R.F. Kiefl, J.M. Stadlbauer and D.C. Walker, J. Phys. Chem. 93 (1989) 388.

84. V.G. Nosov and I.V. Yakovleva, *Zh. Eksp. Teor. Fiz.* 43 (1962) 1750 (English translation in Sov. Phys. - JETP 16 (1963) 1236).

85. L.T. Muus, P.W. Atkins, K.A. McLauchlan and J.B. Peterson, editors, "Chemically Induced Magnetic Polarization" (Reidel, Dordrecht, 1977).

86. T. Asano and W.J. Le Noble, Chem. Rev. 78 (1978) 407.

87. R.R. Hentz, Farhataziz, D.J. Milner and M. Burton, J. Chem. Phys. 46 (1967) 2995.

88. R.R. Hentz, Farhataziz and D.J. Milner, J. Chem. Phys. 49 (1968) 2153.

89. R.R. Hentz and C.G. Johnson Jr., J. Chem. Phys. 51 (1969) 1236.

90. R.R. Hentz and D.W. Brazier, J. Chem. Phys. 54 (1971) 2777.

91. Farhataziz, I. Mihalcea, L.J. Sharp and R.R. Hentz, J. Chem. Phys. 59 (1973) 2309.

92. J.S. Tse and M.L. Klein, J. Phys. Chem. 87 (1983) 5055.

93. B. De Raedt, M. Sprik and M.L. Klein, J. Chem. Phys. 80 (1984) 5719.

94. W. Kolos and L. Wolniewicz, Chem. Phys. Letters 24 (1973) 457.

95. J.K. Kochi, in "Advances in Free Radical Chemistry" Vol. 5, ed. G.H. Williams (Academic Press, New York, 1975) chapter 4, page 189.

96. M.R. Imam and N.L. Allinger, J. Mol. Structure 126 (1985) 345.

97. M.N. Paddon-Row and K.N. Houk, J. Phys. Chem. 89 (1985) 3771.

98. D.E. Wood and R.F. Sprecher, Mol. Phys. 26 (1973) 1311.

99. D. Griller, K.N. Ingold, P.J. Krusic and H. Fischer, J. Am. Chem. Soc. 100 (1978) 6750.

100. M. Yoshimine and J. Pacansky, J. Chem. Phys. 74 (1981) 5168.

101. M.N. Paddon-Row and K.N. Houk, J. Am. Chem. Soc. 103 (1981) 5046.

102. I. Carmichael, J. Phys. Chem. 89 (1985) 4727.

103. I. Pacansky and M. Yoshimine, J. Phys. Chem. 90 (1986) 1980.

104. M.J. Ramos, D. McKenna, B.C. Webster and E. Roduner, J. Chem. Soc. Faraday Trans. I 80 (1984) 255.

105. H. Paul and H. Fischer, Helv. Chim. Acta 56 (1973) 1575.

106. S.F.J. Cox, T.A. Claxton and M.C.R. Symons, Radiat. Phys. Chem. 28 (1986) 107.

107. C.J. Rhodes and M.C.R. Symons, J. Chem. Soc. Faraday Trans. I 84 (1988) 1187.

108. R.W. Fessenden and R.H. Schuler, J. Chem. Phys. 38 (1963) 773.

109. W.G. Filby and K. Günther, J. Chem. Phys. 60 (1974) 3355.

110. M. Lefcourt, K.P. Madden and R.H. Schuler, J. Phys. Chem. 89 (1985) 3101.

111. J.P. Colpa and E. de Boer, Mol. Phys. 7 (1964) 333.

112. K. Eiben and R.H. Schuler, J. Chem. Phys. (1975) 3093.

113. M. Karplus and G.K. Fraenkel, J. Chem. Phys. 35 (1961) 1312.

114. M. Kira, H. Sugiyama and H. Sakurai, J. Am. Chem. Soc. 105 (1983) 6436.

115. H.M. McConnell, J. Chem Phys. 24 (1956) 764.

116. M.B. Yim and D.E. Wood, J. Am. Chem. Soc. 97 (1975) 1004.

117. M. Kira and H. Sakurai, J. Am. Chem. Soc. 99 (1977) 3892.

118. R.F. Kiefl, P.W. Percival, J.C. Brodovitch, S.K. Leung, D. Yu, K. Venkateswaran and S.F.J. Cox, Chem. Phys. Letters 143 (1988) 613.

119. E. Roduner and D.M. Garner, Hyperfine Interactions 32 (1986) 733.

120. R.W. Fessenden and R.H. Schuler, J. Chem. Phys. 39 (1963) 2147.

121. R.W. Fessenden, J. Phys. Chem. 71 (1967) 74.

122. D. Griller, P.R. Marriott and K.F. Preston, J. Chem. Phys. 7 (1979) 3703.

123. D.G. Fleming and M. Senba, in "Atomic Physics with Positrons", J.W. Humberston and E.A.G. Armour, ed., (Plenum, New York, 1987), page 343.

124. M. Senba, R.E. Turner, D.J. Arseneau, D.M. Garner, L.Y. Lee, I.D. Reid and D.G. Fleming, Hyperfine Interactions 31-32 (1986) 795.

125. R.C. Weast, ed., "CRC Handbook of Chemistry and Physics" 59th edition, (CRC Press, West Palm Beach, 1988).

126. D.J. Arseneau, D.G. Fleming, M. Senba, I.D. Reid and D.M. Garner, Can. J. Chem. 66 (1988) 2018.

127. E. Roduner, G.A. Brinkman and P.W.F. Louwrier, Chem. Phys. 88 (1984) 143.

128. H.G. Viehe, Z. Janousek, R. Merenyi and L. Stella, Acc. Chem. Res. 18 (1985) 148.

129. L. Sylvander, L. Stella, H.G. Korth and R. Sustmann, Tetrahedron Letters 26 (1985) 749.

130. H.G. Korth, P. Lommes, R. Sustmann, L. Sylvander and L. Stella, in "Substituent Effects in Radical Chemistry", H.G. Viehe, Z. Janousek and R. Merenyi, eds., (Reidel, Dordrecht, 1986).

131. C.J. Rhodes and E. Roduner, Tetrahedron Letters 29 (1988) 1437.

132. E. Roduner, G.A. Brinkman and P.W.F. Louwrier, Chem. Phys. 73 (1982) 117.

133. D.D.M. Wayner and D.R. Arnold, Can. J. Chem. 63 (1985) 2378.

134. C.J. Rhodes, PhD. Thesis, University of Sussex (1985).

135. D.J. Pasto, R. Krasnansky and C. Zercher, J. Organic Chem. 52 (1987) 3062.